Improvement of the SPH method for multiphase flows application to the emergency water landing of aircrafts : application to the emergency water landing of aircrafts

Imadeddine Hammani

CENTRALE NANTES

THESE DE DOCTORAT DE

L'ÉCOLE CENTRALE DE NANTES

ECOLE DOCTORALE N° 602
Sciences pour l'Ingénieur
Spécialité : Mécanique des Milieux Fluides

Par

Imadeddine Hammani

Amélioration de la méthode SPH pour écoulements multiphasiques

Application à l'amerrissage d'urgence d'avions

Thèse présentée et soutenue à Nantes, le 31 janvier 2020
Unité de recherche : Laboratoire de recherche en Hydrodynamique, Energétique et Environnement Atmosphérique UMR CNRS 6598

Rapporteurs avant soutenance :

Damien Violeau	Chercheur Sénior, EDF R&D
Jacek Pozorski	Professeur des Universités, Institute of Fluid-Flow Machinery, Polish Academy of Sciences

Composition du Jury:

Président:	Jacek Pozorski	Professeur des Universités, Institute of Fluid-Flow Machinery, Polish Academy of Sciences
Examinateurs:	Damien Violeau	Chercheur Sénior, EDF R&D
	Nicolas Grenier	Maître de Conférences, LIMSI, Université Paris Sud
	Lisl Weynans	Maître de Conférences, IMB, INRIA Bordeaux Sud-Ouest, Université de Bordeaux
	Florian de Vuyst	Professeur des Universités, LMAC, Université de Technologie de Compiègne
Dir. de thèse:	David Le Touzé	Professeur des Universités, LHEEA, Centrale Nantes
Co-dir.de thèse:	Guillaume Oger	Maître de Conférences, LHEEA, Centrale Nantes
Co-dir.de thèse:	Zhe Li	Maître de Conférences, LHEEA, Centrale Nantes

ÉCOLE CENTRALE DE NANTES

DOCTORAL THESIS

Improvement of the SPH method for multiphase flows - Application to the emergency water landing of aircrafts

---

Author:
Imadeddine HAMMANI

Supervisor:
Prof. David LE TOUZÉ

A thesis submitted in fulfillment of the requirements for the degree of Doctor of Philosophy

May 14, 2020

Contents

List of Figures

List of Tables

Introduction

One of the specific challenges for the design of aircrafts is to minimize the risk of injury to the persons on board throughout the duration of a potential water landing. To this effect, the motion of the aircraft along with the loadings acting on it are growingly studied during the design phase. However, the ditching process is extremely violent and challenging to solve numerically as it encapsulates multiphase physics, fragmentation and complex dynamics of the air-water interface.

Classical mesh-based Lagrangian methods have been used for the simulation of airborne vehicle impact on water. Examples include the Finite Element Method (FEM) used in the works of Vignjevic et al. [99], Pentecôte et al. [89] and Ortiz et al. [85]. Yet, these mesh-based methods had a hard time reliably solving this kind of violent impact problems, mainly due to the prohibitively large distortion incurred by the meshes. The mesh-based Finite Volume Method (FVM) was also used for the simulation of aircraft ditching, for instance in the works of Wick [106], Guo et al. [39] and Qu et al. [90]. Still, this approach is usually dependent on an interface tracking method (*e.g.* Level-Set, Volume Of Fluids), and its accuracy is highly linked to the accuracy of the interface tracking.

The SPH method has recently been identified as a good candidate for simulating violent multiphase impact problems thanks to its mesh-less and Lagrangian properties. Indeed, the absence of a mesh within the SPH method is a huge advantage for solving flows with violent deformations, since it avoids altogether the problem of mesh distortion that plagues the other aforementioned numerical methods. Moreover, the Lagrangian formalism of the SPH method omits the discretization of any convection term within the governing equations. This aspect is particularly advantageous in the context of multiphase flows, since it prevents any diffusion of the interface between the fluids, effectively suppressing the need of any interface tracking technique.

The SPH method was first introduced by Gingold and Monaghan [32] and Lucy [59] to solve astrophysical problems, after which it was used for flow simulations due to its relatively simple handling of complex interfaces, especially when considered as free surfaces. The SPH method was extended to model incompressible fluids through two approaches. The first approach consists in treating them as "weakly-compressible" [71, 97] where the fluid real sound speeds are replaced by appropriate numerical values that maintain low density variations, while a stiff equation of state is used to explicitly link the pressure to the density. However, this approach classically suffers from high-frequency oscillations that are detrimental to the resulting pressure field. The second approach, called "incompressible SPH" (ISPH) and introduced by Cummins and Rudman [22], enforces incompressibility through

a divergence free velocity field via a pressure Poisson equation [14]. This approach helps eliminating the spurious oscillations of the pressure, but it is computationally expensive since the Poisson equation needs to be solved for each particle at each iteration.

The ISPH method has been extended to multiphase flows [43, 41]. Combinations of incompressible-compressible SPH methods also exist for simulating water-air flows [57]. However, the weakly-compressible SPH formulation is predominantly used within the SPH community in the multiphase framework. Historically, Colagrossi and Landrini [18] presented in 2003 one of the first multiphase SPH models, still used to this day, which was able to handle air-water simulations at realistic density ratios of 1000. Bearing similarities with [18], Grenier et al. [34, 35] derived a multiphase model based on Lagrangian variational principles. Monaghan and Rafiee [75] presented another SPH method for simulating multiphase flows with high-density ratios. All of these models were validated on test cases involving a light and a heavy phase, showing good results that agreed with the experiments or with other numerical methods. However, they all use sound speeds in the light phase that are larger compared to the heavy phase, which can be subject to criticism as in reality the opposite is true, and also yielded to the presence of high-frequency oscillations in the fluid domain.

Therefore, in view of these challenges, one of the aims of the present thesis is the development of a weakly-compressible multiphase SPH model, that is able to handle interfacial flows with high density ratios. This model should also be capable of handling the presence of a free-surface, which for instance in the context of air-water flows, means that only the water phase is modeled instead of both air and water, a potentially relevant choice whenever the air is not expected to influence the solution. Moreover, the proposed model should yield quality pressure fields, *i.e.* without the spurious oscillations which are inherent to the weakly-compressible approach. Practically speaking, the proposed model was implemented and validated on the SPH-Flow software, which is a property of NextFlow Software and Ecole Centrale de Nantes, co-developed with the support of CNR-INM.

The first chapter of this work is a bibliographical study which presents the fundamentals of the SPH method and its application to the Euler equations. Indeed, here the viscosity terms of the Navier-Stokes equations can be neglected since, throughout this thesis, we will be dealing with high Reynolds number problems, such as high speed water impacts. Then the classical stabilization techniques used in SPH are highlighted, and special care is taken to detail the boundary conditions in the multiphase SPH context. Also, all the numerical tools (particle disordering, particle refinement) used throughout this work are exhibited in the last section of this bibliographical study.

The second chapter starts with a survey of the main multiphase weakly compressible SPH models present in the literature. Special care was taken in highlighting the pros and cons of each model. Then, the proposed model, called the Multiphase δ-SPH scheme, is fleshed out in detail in terms of its governing equations and its stabilizing terms. An alternative derivation of the proposed model will be provided, and its set of governing equations is

compared to the first derivation. Later, the numerical stability of the Multiphase δ-SPH scheme is investigated, regarding the maximal stable time steps depending on the sound speed ratio of the simulated phases.

Based on this knowledge, the validation of the proposed Multiphase δ-SPH scheme is carried out in Chapter 3. A series of validation tests are performed over three different benchmarks widely used in the SPH literature. A fourth test case is introduced, featuring the water entry of a corrugated panel involving the entrapment of an air cavity, showing how the proposed SPH method is able to treat complex water impact events.

Later, a comparison between the proposed Multiphase δ-SPH scheme and another Riemann-based SPH model is performed. First, the stability curve of the Riemann-SPH model will be investigated and compared to the one of our proposed model. Conclusions regarding the efficiency of each model will be drawn out, including their respective computational costs. Then, the test cases used to validate the Multiphase δ-SPH scheme in Chapter 3 are rerun using the Riemann-SPH model, and a comparison is made regarding the quality of the pressure field and numerical diffusion yielded by each model.

The fifth and final chapter is in direct link with the industrial context of this work. Indeed, the present thesis is partly funded by the European Commission under the Horizon 2020 research programme. It is part of the SARAH (increased Safety And Robust certification for ditching of Aircrafts and Helicopters) project, a collaborative endeavor aiming at establishing novel simulation-based approaches to the analysis of aircraft and helicopter ditching. Results of the SARAH project are expected to support the certification of future aircrafts and helicopters while enhancing the safety of air transport in general.

Therefore, in Chapter 5 a numerical investigation of a ditching problem using the SPH method is carried out. It is based on the experimental campaign of Iafrati et al. [44], which highlighted the occurrence of cavitation in the water depending on impact velocity. In this chapter, a simple yet effective technique of cavitation capturing is proposed and validated through a series of 2D and 3D fuselage ditching simulations.

Chapter 1

SPH fundamentals

1.1 The governing equations

1.1.1 The Euler equations

The Euler equations are a simplified form of the Navier-Stokes equations in the case of inviscid flows. They express the conservation of mass, momentum and energy of a fluid medium. The mass conservation is described in a Lagrangian form by the following equation:

$$\frac{d\rho}{dt} = -\rho \nabla \cdot \mathbf{u} \tag{1.1}$$

where $\frac{d}{dt}$ is the material derivative, ρ and $\mathbf{u}$ are the fluid's density and velocity respectively, and $\nabla\cdot$ denotes the divergence operator. The momentum conservation equation reads:

$$\frac{d\mathbf{u}}{dt} = -\frac{\nabla P}{\rho} + \mathbf{g} \tag{1.2}$$

where P and $\mathbf{g}$ are respectively the pressure and the gravity, and ∇ is the gradient operator. In a Lagrangian formalism, the trajectory of a material particle is described by:

$$\frac{d\mathbf{x}}{dt} = \mathbf{u} \tag{1.3}$$

In order to close the system of equations (1.1) and (1.2), an equation of state is introduced to link the pressure to the density. In the present thesis, the Cole equation of state [21] is used to this effect:

$$P = \frac{\rho_0 c_0^2}{\gamma}\left[\left(\frac{\rho}{\rho_0}\right)^{\gamma} - 1\right] \tag{1.4}$$

where c_0, ρ_0 and γ are the fluid reference sound speed, nominal density and polytropic coefficient respectively. By using this particular barotropic equation of state there is no need to solve an energy equation since the pressure and the energy are assumed independent.

Therefore, throughout this study we use the following system of governing equations:

$$\begin{cases} \dfrac{d\mathbf{x}}{dt} = \mathbf{u} \\ \dfrac{d\rho}{dt} = -\rho \nabla \cdot \mathbf{u} \\ \dfrac{d\mathbf{u}}{dt} = -\dfrac{\nabla P}{\rho} + \mathbf{g} \\ P = \dfrac{\rho_0 c_0^2}{\gamma}\left[\left(\dfrac{\rho}{\rho_0}\right)^{\gamma} - 1\right] \end{cases} \tag{1.5}$$

1.2 The SPH method

1.2.1 The SPH interpolation

The SPH (Smoothed Particle Hydrodynamics) is a meshless method. It is based on the discretization of the domain into scattered points which are not linked together by connectivities, conversely to other classic numerical methods (*e.g.* Finite Elements/Volumes). Thus, it is essential within the SPH method to derive operators that can estimate the fields and their gradients while being free from the constraints of a mesh.

The fundamental idea of the SPH interpolation is the approximation of a field quantity $f(\mathbf{x})$ at a certain point $\mathbf{x}$ of the fluid domain D using the known field quantity $f(\mathbf{y})$ in its vicinity through the use of a convolution product.

As a first step we can write the following convolution:

$$\langle f \rangle(\mathbf{x}) = f * \delta(\mathbf{x}) = f(\mathbf{x}) = \int_D f(\mathbf{y})\delta(\mathbf{x}-\mathbf{y})dV \tag{1.6}$$

where $\delta(.)$ is the Dirac distribution verifying:

$$\int_D \delta(\mathbf{x})dV = 1 \tag{1.7}$$

At the continuum level, the use of the Dirac distribution allows for the exact evaluation of a function value at a considered point of space. The Dirac distribution is then approximated by a regular function W. This function has a compact support Ω and is called the interpolation kernel. This leads finally to the following approximation [32]:

$$\langle f \rangle(\mathbf{x}) \simeq f * W = \int_\Omega f(\mathbf{y})W(\mathbf{x}-\mathbf{y}, R_k)dV \tag{1.8}$$

where the spatial parameter R_k is the kernel support radius. When R_k approaches 0, the kernel function must tend towards the Dirac distribution:

$$\lim_{R_k \to 0} W(\mathbf{x}, R_k) = \delta(\mathbf{x}) \tag{1.9}$$

Furthermore, if the kernel is positive, symmetric, monotonically decreasing and verifies:

$$\int_\Omega W(\mathbf{x}, R_k)dV = 1 \tag{1.10}$$

then the approximation (1.8) is second-order accurate [67] :

$$\langle f \rangle = f + O(R_k^2) \tag{1.11}$$

1.2.2 The SPH differential operators

Based on (1.8), the gradient of a function f can be evaluated as:

$$\langle \nabla f \rangle(\mathbf{x}) = \int_\Omega \nabla_\mathbf{y} f(\mathbf{y}) W(\mathbf{x} - \mathbf{y}, R_k)dV \tag{1.12}$$

This expression holds only if the kernel support radius R_k is constant, which is the case throughout the present work unless specified otherwise. Using integration by parts, we have:

$$\langle \nabla f \rangle(\mathbf{x}) \simeq \int_{\partial\Omega} f(\mathbf{y}) W(\mathbf{x} - \mathbf{y}, R_k)\mathbf{n}dS - \int_\Omega f(\mathbf{y}) \nabla_\mathbf{y} W(\mathbf{x} - \mathbf{y}, R_k)dV \tag{1.13}$$

where $\partial\Omega$ denotes the boundary of the kernel support and $\mathbf{n}$ denotes the normal to $\partial\Omega$ pointing outwards. When the kernel support does not intersect the domain boundary, the first integral is null due the compactness property of the kernel. The kernel gradient being antisymmetric:

$$\nabla_\mathbf{x} W(\mathbf{x} - \mathbf{y}, R_k) = -\nabla_\mathbf{y} W(\mathbf{x} - \mathbf{y}, R_k) \tag{1.14}$$

then :

$$\langle \nabla f \rangle(\mathbf{x}) \simeq \int_\Omega f(\mathbf{y}) \nabla_\mathbf{x} W(\mathbf{x} - \mathbf{y}, R_k)dV \tag{1.15}$$

Note that (1.15) allows to determine the gradient of f simply through the knowledge of f itself and the simple analytical computation of the kernel gradient, which is an important feature of the SPH method. Furthermore, the kernel gradient verifies:

$$\int_\Omega \nabla W(\mathbf{x} - \mathbf{y}, R_k)dV = 0 \tag{1.16}$$

and the approximation (1.15) is second-order accurate [67]:

$$\langle \nabla f \rangle = \nabla f + O(R_k^2) \tag{1.17}$$

1.2.3 The discretized SPH approximation

The SPH approximation is based on the discretization of a continuum into N fluid elements called particles, which serve as interpolation points. To each particle i are associated discrete values of the physical fields: position $\mathbf{x}_i$, velocity $\mathbf{u}_i$, volume V_i, density ρ_i, etc.

Using the midpoint quadrature rule for approximating integrals, the interpolations (1.8) and (1.15) are discretized as follows:

$$\langle f \rangle_i = \sum_{j=1}^{N} f_j W_{ij} V_j \tag{1.18}$$

$$\langle \nabla f \rangle_i = \sum_{j=1}^{N} f_j \nabla_i W_{ij} V_j \tag{1.19}$$

where $f_j = f(\mathbf{x}_j)$, $W_{ij} = W(\mathbf{x}_i - \mathbf{x}_j, R_k)$ and $\nabla_i W_{ij} = \nabla_{\mathbf{x}} W(\mathbf{x}_i - \mathbf{x}_j, R_k)$.

However, once discretized the SPH operators lose their second-order accuracy as:

$$\sum_{j=1}^{N} W_{ij} V_j \neq 1 \quad \text{and} \quad \sum_{j=1}^{N} \nabla_i W_{ij} V_j \neq 0 \tag{1.20}$$

in a general case [91]. The convergence is achieved theoretically if the number of particles N is infinite and if the kernel tends towards the Dirac function. Noting Δx as a reference distance between two particles, these conditions are equivalent to:

$$\frac{R_k}{\Delta x} \to \infty \quad \text{and} \quad R_k \to 0 \tag{1.21}$$

Numerically the first condition is impossible to achieve as in practice the number of neighboring particles is fixed to keep non prohibitive CPU costs. The effect of the ratio $R_k/\Delta x$ on the convergence of the interpolations (1.18) and (1.19) was investigated in [91, 82]. It was found that in practice, a good compromise between precision and CPU time can be achieved with some ratios, the convergence being limited to an acceptable error due to not respecting the $\Delta x/R_k \to 0$ condition. Throughout this work, the ratio $R_k/\Delta x$ is taken equal to 4 in 2D and 2.4 in 3D in order to limit the CPU time as the number of neighboring particles drastically increases in 3D.

Nevertheless, some correction techniques were developed by the SPH community in order to improve the precision of the interpolation. These will be discussed in Section 1.3.3.

1.2.4 Adopted kernel function

The kernel W is a regular function with compact support, usually circular in 2D and spherical in 3D. The interpolation kernels remain one of the subjects of research in SPH as different kernels could sometimes yield better or worse results for the same considered test case, especially in terms of stability.

One of the most used kernels is the C^2 Wendland kernel [105], for which improved stability properties exist [24]. Noting $q = \|\mathbf{x}\|/R_k$, the C^2 Wendland kernel is defined as follows:

$$W(\mathbf{x}, R_k) = \frac{1}{V_k}\theta(q) \tag{1.22}$$

where

$$\theta(q) = C \times \begin{cases} (1-q)^4(1+4q) & \text{if } 0 \leq q \leq 1, \\ 0 & \text{otherwise.} \end{cases} \tag{1.23}$$

and the kernel radius is $R_k = 2h$, where h is a spatial parameter called the smoothing length of the kernel.

The constant C normalizes the kernel so that Eq. (1.10) is verified. It is equal to 7 in 2D and 14 in 3D. The term V_k corresponds to the kernel support volume (πR_k^2 in 2D and $\frac{4\pi R_k^3}{3}$ in 3D). Unless specified otherwise, this is the kernel used throughout the present work.

1.3 Application to the Euler Equations

1.3.1 The weakly-compressible approach

It is possible to model flows considered incompressible using compressible governing equations. Indeed, it was shown, see *e.g.* [10], that when the Mach number is low, the full compressible solution is equal to the sum of the incompressible solution, of an acoustic contribution in $\mathcal{O}(Ma)$ and of additional terms in $\mathcal{O}(Ma^2)$, where the Mach number is $Ma = u_{max}/c_0$ and u_{max} is the maximal flow speed. Therefore, the Mach number is the criterion that characterizes the incompressibility of the flow.

A limit on the Mach number Ma is usually taken as a threshold below which the compressible numerical solutions are considered close to the incompressible solution. The value of $Ma \leq 0.1$ is commonly adopted within this "weakly-compressible" approach, whereby the weakly-compressible fluid dynamics closely follows its incompressible counterpart.

The weakly-compressible SPH (WCSPH) approach consists in choosing the numerical sound speed c_0 in Eq. (1.4) so as to respect the condition $Ma \leq 0.1$. This choice is legitimate since the acoustic contributions to the solutions have a very small energy and will not impact the incompressible part of the flow. Indeed, the density/pressure fluctuations are proportional to the Mach number squared [10].

Note that this approach necessitates a priori the estimation of the maximal speed u_{max} reached during the flow evolution so that the condition on the Mach number stays verified during the whole simulation. Moreover, this condition on the Mach number infers that the numerical density variations should be less than 1% within the weakly-compressible approach, which is always checked post-computations.

1.3.2 The SPH discretized governing equations

The governing equations are approximated here through the SPH interpolation presented in the previous section. The regularized Euler equations read:

$$\begin{cases} \dfrac{d\mathbf{x}}{dt} = \mathbf{u} \\ \dfrac{d\rho}{dt} = -\rho\langle\nabla\cdot\mathbf{u}\rangle \\ \dfrac{d\mathbf{u}}{dt} = -\dfrac{\langle\nabla P\rangle}{\rho} + \mathbf{g} \\ P = \dfrac{\rho_0 c_0^2}{\gamma}\left[\left(\dfrac{\rho}{\rho_0}\right)^{\gamma} - 1\right] \end{cases} \tag{1.24}$$

Based on Eq. (1.15), the pressure gradient can be approximated as:

$$\langle\nabla P\rangle(\mathbf{x}) = \int_\Omega P(\mathbf{y})\nabla_{\mathbf{x}} W dV \tag{1.25}$$

which is discretized as follows:

$$\langle\nabla P\rangle_i = \sum_j P_j \nabla_i W_{ij} V_j \tag{1.26}$$

However, in practice this form of the pressure gradient induces numerical instabilities since it violates the action-reaction principle, *i.e.* the discrete momentum conservation. Indeed, taking into account two interacting particles i and j, $\mathbf{F}_{i\to j} = -\mathbf{F}_{j\to i}$ is supposed to be verified, which is not true when using Eq. (1.26):

$$-\frac{m_i}{\rho_i} P_j \nabla_i W_{ij} V_j \neq \frac{m_j}{\rho_j} P_i \nabla_j W_{ij} V_i \tag{1.27}$$

In order to restore the reciprocity of interactions, the pressure gradient can be made anti-symmetrical using:

$$\nabla P = \nabla P + P\nabla 1 \tag{1.28}$$

which yields:

$$\langle\nabla P\rangle(\mathbf{x}) = \int_\Omega (P(\mathbf{y}) + P(\mathbf{x}))\nabla_{\mathbf{x}} W dV \tag{1.29}$$

and its discretized form:

$$\langle\nabla P\rangle_i = \sum_j (P_j + P_i)\nabla_i W_{ij} V_j \tag{1.30}$$

Similarly, the velocity divergence operator is written so as to evaluate exactly the divergence of constant fields:

$$\nabla\cdot\mathbf{u} = \nabla\cdot\mathbf{u} - \nabla 1\cdot\mathbf{u} \tag{1.31}$$

meaning:

$$\langle \nabla \cdot \mathbf{u} \rangle(\mathbf{x}) = \int_{\Omega} (\mathbf{u}(\mathbf{y}) - \mathbf{u}(\mathbf{x})) \cdot \nabla_{\mathbf{x}} W dV \tag{1.32}$$

which is finally discretized as:

$$\langle \nabla \cdot \mathbf{u} \rangle_i = \sum_j (\mathbf{u}_j - \mathbf{u}_i) \cdot \nabla_i W_{ij} V_j \tag{1.33}$$

Beyond this symmetrization process lies the concept of compatibility between the divergence and gradient operators. Indeed, the choice of the divergence operator (1.32) for the continuity equation formally leads to the compatible form of the pressure gradient (1.29) in the momentum equation so as to guarantee energy conservation of the system. This concept of compatibility was demonstrated by Bonet and Lok [7] using a variational approach, and Monaghan [73] through a derivation based on a Lagrangian. It was further extended for free-surface flows by Colagrossi et al. [16] using the Principle of Virtual Works.

All in all, using Eqs. (1.29) and (1.32), the standard, weakly-compressible discretized system of Euler equations reads:

$$\begin{cases} \dfrac{d\mathbf{x}_i}{dt} = \mathbf{u}_i & (1.34) \\ \dfrac{d\rho_i}{dt} = -\rho_i \displaystyle\sum_j (\mathbf{u}_j - \mathbf{u}_i) \nabla_i W_{ij} V_j & (1.35) \\ \dfrac{d\mathbf{u}_i}{dt} = \mathbf{g} - \dfrac{1}{\rho_i} \displaystyle\sum_j (P_i + P_j) \nabla_i W_{ij} V_j & (1.36) \\ P_i = \dfrac{\rho_{0i} c_{0i}^2}{\gamma_i} \left[\left(\dfrac{\rho_i}{\rho_{0i}} \right)^{\gamma_i} - 1 \right] & (1.37) \end{cases}$$

This scheme will be hereinafter referred to as “Standard Scheme”.

1.3.3 Improvement of the accuracy of the SPH operators

1.3.3.1 The Shepard correction

Several methods are available in the literature to enhance the order of accuracy of the SPH operators. One of them is the Shepard correction, which is used to ensure the equality:

$$\sum_j W_{ij} V_j = 1 \tag{1.38}$$

regardless of the particles distribution in space. This is achieved by modifying the kernel function as follows:

$$W^S = \frac{W_{ij}}{\sum_j W_{ij} V_j} \tag{1.39}$$

1.3.3.2 The renormalization matrix

Another correction was proposed by Randles and Libersky [92] who introduced a renormalization matrix that increases the order of the interpolation (1.19):

$$\langle \nabla \cdot \mathbf{f} \rangle_i^{\mathcal{L}} = \sum_j (\mathbf{f}_j - \mathbf{f}_i) \cdot \mathcal{L}_i \cdot \nabla_i W_{ij} V_j \tag{1.40}$$

$$\langle \nabla f \rangle_i^{\mathcal{L}} = \sum_j (f_j - f_i) \mathcal{L}_i \nabla_i W_{ij} V_j \tag{1.41}$$

where $\mathcal{L}_i$ is the renormalization matrix given by :

$$\mathcal{L}_i = [\sum_j (\mathbf{x}_j - \mathbf{x}_i) \otimes \nabla_i W_{ij} V_j]^{-1} \tag{1.42}$$

This operator allows for the exact evaluation of linear field gradients.

A third correction was introduced by Dilts *et al.* [25] which allows to exactly evaluate constant functions, linear functions and gradients of linear functions, through the use of Moving Least Squares.

1.4 Stabilization techniques in SPH

The Lax equivalence theorem states that a numerical scheme converges towards the solution of a system of differential equations if and only if the scheme is consistent and stable [53].

The first condition of convergence is guaranteed since the Euler equations were discretized in a consistent manner in Section 1.3.2 [7, 16, 100] provided that conditions (1.21) are verified.

Stability means that the total variation of the numerical solution is bounded at any fixed time t when the time step Δt goes to 0 [53]. The standard SPH scheme (1.34-1.37), which is based on a space centered-like interpolation [100] and is generally solved via explicit time integration within the WCSPH context, is known to be unconditionally unstable.

In order to ensure the stability of this Standard Scheme, numerical diffusive terms are introduced within the equations. Many forms of stabilization terms are available in the literature. The following sections will present the main ones used within the SPH community. A detailed study of convergence can be found in Vila [100].

1.4.1 Artificial viscosity

Monaghan [72] adapted the concept of artificial viscosity of Von Neumann and Richtmyer [79] to the SPH method by introducing a pseudo-pressure term:

$$\Pi_{ij} = -\frac{1}{8} R_k \alpha (\rho_i + \rho_j)(c_i + c_j) \mu_{ij} \tag{1.43}$$

where

$$\mu_{ij} = \begin{cases} \dfrac{\mathbf{u}_{ij} \cdot \mathbf{x}_{ij}}{||\mathbf{x}_{ij}||^2 + \epsilon R_k^2} & \text{if } \mathbf{u}_{ij} \cdot \mathbf{x}_{ij} < 0 \\ 0 & \text{otherwise} \end{cases} \tag{1.44}$$

and where $\mathbf{u}_{ij} = \mathbf{u}_i - \mathbf{u}_j$, $\mathbf{x}_{ij} = \mathbf{x}_i - \mathbf{x}_j$, α is a coefficient chosen between 0.01 and 1 depending on the simulation, and ϵ is a parameter usually equal to 0.01, that avoids a singularity when $\mathbf{x}_{ij} = 0$.

Once added in the momentum equation (1.36) it writes:

$$\frac{d\mathbf{u}_i}{dt} = \mathbf{g} - \frac{1}{\rho_i} \sum_j (P_i + P_j + \Pi_{ij}) \nabla_i W_{ij} V_j \tag{1.45}$$

The term (1.44) acts as a diffusive term, improving the stability of the scheme.

1.4.2 δ-SPH

In addition to adding a numerical viscous term to the momentum equation, some authors studied the possibility of adding numerical diffusive terms also in the continuity equations in order to filter out some of the spurious oscillations in the pressure, which are a drawback of weakly-compressible SPH. Indeed, since the pressure is computed via a state equation, a smooth density field would automatically lead to a smooth pressure field.

Ferrari et al. [30] proposed to add a numerical diffusive term to the continuity equation in order to reduce the numerical noise inside the density field, but it was inconsistent at the free-surface. Molteni and Colagrossi [69] also studied the possibility of adding a numerical diffusive term inside the continuity equation. Their formulation yielded good results but did not compute correctly the hydrostatic problem. To circumvent this issue, Antuono et al. [3] corrected the diffusive term of Molteni and Colagrossi [69] making it compatible with the hydrostatic solution and yielding pressure fields without spurious oscillations, even in the presence of a free-surface.

The governing equations of the δ-SPH model of Antuono et al. [3] read:

$$\begin{cases} \dfrac{d\rho_i}{dt} = -\rho_i \sum_j (\mathbf{u}_j - \mathbf{u}_i) \cdot \nabla_i W_{ij} V_j + \delta h c_0 \mathcal{D}_i \\ \rho_i \dfrac{d\mathbf{u}_i}{dt} = -\sum_j (P_i + P_j) \nabla_i W_{ij} V_j + \rho_i \mathbf{g} + \alpha h c_0 \rho_0 \sum_j \pi_{ij} \nabla_i W_{ij} V_j \\ \dfrac{d\mathbf{x}_i}{dt} = \mathbf{u}_i \end{cases} \tag{1.46}$$

where π_{ij} is a viscosity term defined as:

$$\pi_{ij} = \frac{\mathbf{u}_{ij} \cdot \mathbf{x}_{ij}}{||\mathbf{x}_{ij}^2||} \tag{1.47}$$

with the parameter α ranging between 0.01 and 0.1 depending on the problem at hand. For example for violent impact problems $\alpha = \mathcal{O}(0.1)$ is generally adopted in order to stabilize the scheme.

The diffusive term denoted by $\mathcal{D}_i$ is controlled by a dimensionless parameter δ, hence the denomination "δ-SPH". In order to properly tune the coefficient δ, Antuono et al. [3] presented a linear stability analysis which yielded a variability range of δ in $0 < \delta < 0.2$.

Note that both numerical terms in the continuity and momentum equations are proportional to the smoothing length h in order to guarantee the consistency with the Euler equations when $h \to 0$.

In the δ-SPH scheme the density diffusive term has the form of a density Laplacian. In SPH the Laplacian is generally approximated through the Morris formula [76]:

$$\langle \nabla^2 f \rangle_i = 2 \sum_j (f_j - f_i) \frac{\mathbf{x}_{ji} \cdot \nabla_i W_{ij}}{\mathbf{x}_{ji}^2} V_j \tag{1.48}$$

where f is a generic scalar function. However, Antuono et al. [3] proved that this formula diverges along the free-surface, and proposed a formulation which recovers the convergence of the diffusive term over the entire fluid domain.

Considering a generic kernel with the following structure:

$$W = W\left(- \frac{||\mathbf{x}_{ij}||^2}{h^2} \right) \Rightarrow \nabla_i W\left(- \frac{||\mathbf{x}_{ij}||^2}{h^2} \right) = \frac{2}{h^2} \mathbf{x}_{ji} W\left(- \frac{||\mathbf{x}_{ij}||^2}{h^2} \right) \tag{1.49}$$

the expression (1.48) becomes:

$$\langle \nabla^2 f \rangle_i = \frac{4}{h^2} \sum_j (f_j - f_i) W_{ij} V_j \tag{1.50}$$

Using a Taylor expansion Antuono et al. proved that Eq. (1.50) comes from:

$$\langle \nabla^2 f \rangle_i = \frac{4}{h^2} \sum_j (f_j - f_i) W_{ij} V_j - 2 \nabla f_i \cdot \nabla S_i + \mathcal{O}((1 - S_i)) + \mathcal{O}(h^2) \tag{1.51}$$

where $S_i = \sum_j W_{ij} V_j$ and $\nabla S_i = \sum_j \nabla_i W_{ij} V_j$. This means that the Morris formula converges to the Laplacian of f if $\nabla S = 0$ and $S = 1$. Colagrossi et al. [16] proved that these conditions hold inside the fluid but not near the free-surface where ∇S diverges like $\frac{1}{h}$. Consequently, the Morris formula also diverges near the free-surface.

Thus, Antuono et al. [3] proposed the following conservative expression of the diffusive term:

$$\langle \mathcal{D}(f)_i \rangle = \frac{4}{h^2} \sum_j \left[(f_j - f_i) - \frac{1}{2} (\nabla f_j + \nabla f_i) \cdot \mathbf{x}_{ji} \right] W_{ij} V_j + \mathcal{O}(h) \tag{1.52}$$

where the contribution of ∇S is eliminated. The convergence of $\langle \nabla f \rangle$ to ∇f is ensured by using the renormalized gradient presented in Section 1.3.3.2 to evaluate the gradients in Eq. (1.52). Finally, the definitive δ-SPH diffusive term of Antuono et al. [3] reads:

$$\mathcal{D}_i = \sum_j \psi_{ij} \cdot \nabla_i W_{ij} V_j \tag{1.53}$$

where

$$\psi_{ij} = 2(\rho_j - \rho_i) \frac{\mathbf{x}_{ji}}{||\mathbf{x}_{ij}||^2} - [\langle \nabla \rho \rangle_i^{\mathcal{L}} + \langle \nabla \rho \rangle_j^{\mathcal{L}}] \tag{1.54}$$

It is important to note that the δ-SPH model is still used even with kernels that do not verify the structure of Eq. (1.49), such as the C^2 Wendland kernel (Section 1.2.4) used in this study (and in, e.g., [96]).

1.4.3 Riemann-SPH

Inspired from the Finite Volume Method, Vila [100] and Parshikov et al. [87] proposed to stabilize the Standard Scheme by solving Riemann problems at each pair interaction.

The Riemann problem is solved at the interface between particles i and j located at $\bar{\mathbf{x}}_{ij} = \dfrac{\mathbf{x}_i + \mathbf{x}_j}{2}$, with an interface velocity $\bar{\mathbf{u}}_{ij} = \dfrac{\mathbf{u}_i + \mathbf{u}_j}{2}$ and a normal direction $\mathbf{n}_{ij} = \dfrac{\nabla_i W_{ij}}{||\nabla_i W_{ij}||}$. The Riemann-SPH scheme proposed by Vila reads:

$$\begin{cases} \dfrac{d\mathbf{x}_i}{dt} = \mathbf{u}_i & (1.55) \\ \dfrac{dV_i}{dt} = V_i \displaystyle\sum_j (\mathbf{u}_j - \mathbf{u}_i) \cdot \nabla W_{ij} V_j & (1.56) \\ \dfrac{d(\rho_i V_i)}{dt} = -V_i \displaystyle\sum_j 2\rho_E (\mathbf{u}_E - \mathbf{u}(\bar{\mathbf{x}}_{ij})) \nabla_i W_{ij} V_j & (1.57) \\ \dfrac{d(\rho_i V_i \mathbf{u}_i)}{dt} = \rho_i V_i \mathbf{g} - V_i \displaystyle\sum_j 2(\rho_E \mathbf{u}_E \otimes (\mathbf{u}_E - \mathbf{u}(\bar{\mathbf{x}}_{ij})) + P_E \mathbb{I}) \nabla_i W_{ij} V_j & (1.58) \end{cases}$$

where ρ_E, $\mathbf{u}_E$ and p_E are solutions of the Riemann problem formulated at the interface between i and j. This solution can be computed via exact [46] or linearized [77, 86] solvers. Throughout this work, the acoustic Riemann solver of Murrone and Guillard [77] is used, which computes $\mathbf{u}_E$ and p_E as:

$$\begin{cases} u_E = \dfrac{\rho_i c_i u_i + \rho_j c_j u_j}{\rho_i c_i + \rho_j c_j} + \dfrac{P_i - P_j}{\rho_i c_i + \rho_j c_j} & (1.59) \\ P_E = \dfrac{\rho_j c_j P_i - \rho_i c_i P_j}{\rho_i c_i + \rho_j c_j} + \dfrac{\rho_i c_i \rho_j c_j (u_i - u_j)}{\rho_i c_i + \rho_j c_j} & (1.60) \end{cases}$$

Although Eq. (1.57) does not keep particle masses constant anymore (since a mass flux exists), the mass exchange is symmetrical between i and j, ensuring the mass conservation of the system.

Taking for left and right states values of the Riemann problem the values at the particles i and j leads to a very dissipative (and low order) scheme. To decrease the numerical dissipation while increasing the order of the scheme, Van Leer [55] proposed the MUSCL (Monotonic Upstream Scheme for Conservation Laws) method, which consists in replacing the left and right states by piecewise linear reconstructions from the particles to the interface between i and j, as illustrated in Fig. 1.1.

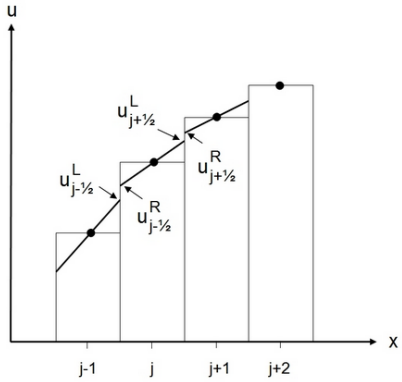

FIGURE 1.1: An example of MUSCL type left and right state piecewise linear reconstructions.

We will see later that the Riemann-SPH scheme can be adapted quite straightforwardly to take into account multiphase flows.

1.5 Boundary conditions in SPH

We consider a fluid domain Ω where different fluids are present. The fluid domain is limited by a solid boundary $\partial\Omega_B$ and also by a free-surface $\partial\Omega_F$ (when the pressure of the lighter phase, usually a gas, does not affect the dynamics of the heavy phase). The solid boundary consists of an external frontier which contains Ω, and of solid bodies with can be inside the fluid domain and can move across $\partial\Omega_F$. Inside the fluid domain, interfaces between different fluids can also be present. Fig. 1.2 shows a sketch of the problem, which can be solved by the multiphase SPH model proposed in this thesis.

Therefore, in order to define well the tackled problems and solve the Euler governing equations, we need to impose conditions on the domain boundaries and interfaces. These consist of kinematic and dynamic boundary conditions.

The kinematic boundary conditions are enforced on the velocity of the considered fluids. In the case of the Navier-Stokes equations, the kinematic condition expresses the continuity of the tangential (no-slip) and normal velocities at the interface $\partial\Omega_I$ between two mediums $\mathcal{X}$ and $\mathcal{Y}$:

$$\mathbf{u}_{\mathcal{X}}(\mathbf{x}) = \mathbf{u}_{\mathcal{Y}}(\mathbf{x}), \quad \forall \mathbf{x} \in \partial\Omega_I \tag{1.61}$$

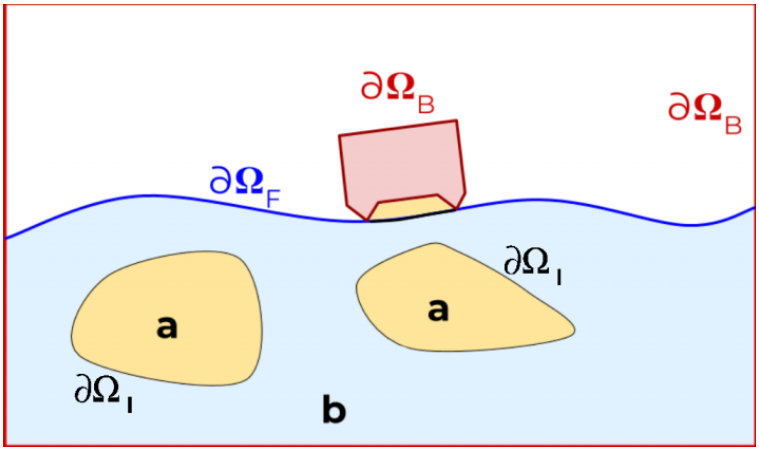

FIGURE 1.2: Sketch of the domain. The domain Ω is confined by a solid boundary $\partial\Omega_B$, which comprises walls and solid bodies. Different fluids a and b are present. They are delimited by an interface $\partial\Omega_I$, while a free-surface $\partial\Omega_F$ is also present.

For the Euler equations, a non-penetration condition is enforced, and expresses the continuity of the normal velocity at the interface:

$$\mathbf{u}_{\mathcal{X}}(\mathbf{x}) \cdot \mathbf{n} = \mathbf{u}_{\mathcal{Y}}(\mathbf{x}) \cdot \mathbf{n}, \quad \forall \mathbf{x} \in \partial\Omega_I \tag{1.62}$$

where $\mathbf{n}$ is the normal to the interface. The same condition is applied if $\mathcal{Y}$ is a rigid solid or the moving free-surface.

The dynamic boundary condition at the interface $\partial\Omega_I$ between two mediums $\mathcal{X}$ and $\mathcal{Y}$ expresses the continuity of the normal stresses across the interface:

$$\mathcal{T}^{\mathcal{X}}(\mathbf{x}).\mathbf{n} = \mathcal{T}^{\mathcal{Y}}(\mathbf{x}).\mathbf{n}, \qquad \forall \mathbf{x} \in \partial\Omega_I \tag{1.63}$$

where $\mathcal{T}$ is the stress tensor. For the Euler equations and in the absence of surface tension effects, this condition reduces to the continuity of pressure across the interface.

The enforcement of these boundary conditions is a challenge for the SPH method. The reasons for this are twofold. First, unlike other mesh-based methods, it is difficult to impose boundary conditions on the mobile SPH particles. Secondly, the kernel support is truncated near the limits of the domain. Consequently, the surface term in the SPH gradient operator (1.13) cannot be neglected anymore and needs to be soundly taken into account, and the approximation of the volumic term becomes very poor due to lack of particles in the support.

In this section, the general SPH kinematic and dynamic conditions at the interface between two mediums $\mathcal{X}$ and $\mathcal{Y}$ are explained. These mediums can represent:

- a fluid/solid interface, where in the present work the solid is always taken as a non-deformable wall, or
- a fluid/fluid interface, as in a air/water configuration for instance, or

- a fluid/void interface, *i.e.* a free-surface.

1.5.1 Solid boundary conditions in SPH

There are several techniques in the literature which make it possible to impose kinematic and dynamic wall boundary conditions. These are split in two frameworks.

The first consists of volumetric methods that extend the fluid domain by considering a fictitious domain in which moving, see *e.g.* [18], or fixed [62] ghosts particles are created in order to complete the kernel support for near-wall particles. In this case, the kernel support is filled even close to the boundary and no surface term need to be accounted for. The difficulty lies in creating and imposing conditions to the ghost particles.

The second framework consists of surface term methods that aim to introduce wall integrals in the differential operators of Section 1.3.2 [52, 29, 56, 102]. These methods are known as Boundary Integral Methods (BIM). Chiron [11] extensively covered the state-of-the-art of these methods. Authors like De Leffe [23], Feldman [28] and Leroy et al. [56] developed such Boundary Integral Methods in SPH formalism, which has the advantage of better handling complex wall geometries compared to the ghost particles method.

In the following sections, the moving ghosts particles and the BIM used in this work are presented.

1.5.1.1 The moving ghost particles

The idea of this method is to complete the fluid particles kernel support by adding a fictive domain Ω_G of ghost particles. The position of these ghost particles is computed by mirroring the fluid particles with respect to the walls. The symmetrization include the fluid particles whose support intersects the solid wall, see *e.g.* [18, 84].

For a plane wall, the position of the ghost particle $g(i)$ mirrored from a particle i is :

$$\mathbf{x}_{g(i)} = \mathbf{x}_i + 2(\mathbf{x}_w \cdot \mathbf{n} - \mathbf{x}_i \cdot \mathbf{n})\mathbf{n} \tag{1.64}$$

where $\mathbf{x}_w$ refers to the wall position and $\mathbf{n}$ to the wall normal. The no-penetration condition (1.62) is enforced through :

$$\mathbf{u}_{g(i)} = \mathbf{u}_i + 2(\mathbf{u}_w \cdot \mathbf{n} - \mathbf{u}_i \cdot \mathbf{n})\mathbf{n} \tag{1.65}$$

with $\mathbf{u}_w$ the local velocity of the wall.

The ghost pressure must take into account the wall kinematics and the presence of volumetric forces such as gravity, otherwise non-physical fluxes appear through the solid boundaries. Differentiating the no-penetration condition yields [81]:

$$\frac{d\mathbf{u}}{dt} \cdot \mathbf{n} = (\mathbf{u}_w - \mathbf{u}) \cdot \frac{d\mathbf{n}}{dt} + \frac{d\mathbf{u}_w}{dt} \cdot \mathbf{n} \tag{1.66}$$

then :

$$-\frac{1}{\rho}\frac{\partial P}{\partial n}+\mathbf{g}\cdot\mathbf{n}=(\mathbf{u}_w-\mathbf{u})\cdot\frac{d\mathbf{n}}{dt}+\frac{d\mathbf{u}_w}{dt}\cdot\mathbf{n} \tag{1.67}$$

And since by differentiating the Cole equation of state (1.4) we have:

$$\frac{\partial P}{\partial n}=\frac{\partial P}{\partial \rho}\frac{\partial \rho}{\partial n}=c_0^2\left(\frac{\rho}{\rho_0}\right)^{\gamma-1}\frac{\partial \rho}{\partial n} \tag{1.68}$$

we get by integration [81]:

$$\rho_g(i)=\left[\rho_i^{\gamma-1}+\frac{\rho_0^{\gamma-1}(\gamma-1)}{c_0^2}\left((\mathbf{u}-\mathbf{u}_w)\cdot\frac{d\mathbf{n}}{dt}-\frac{d\mathbf{u}_w}{dt}\cdot\mathbf{n}+\mathbf{g}\cdot\mathbf{n}\right)(\mathbf{x}_{g(i)}-\mathbf{x}_i)\cdot\mathbf{n}\right]^{\frac{1}{\gamma-1}} \tag{1.69}$$

Then the ghost pressure is determined by the equation of state (1.4) using the ghost density $\rho_g(i)$.

The volume of the ghost particle also needs to be determined. In the case of a plane wall, the volume of the ghost particle is taken equal to the corresponding fluid counterpart :

$$V_{g(i)}=V_i \tag{1.70}$$

In this work, apart from the ditching simulations, we will be dealing systematically with plane, non-moving walls for the 2D academic test case validations. The position, velocity, density and volumes of the ghost particles are sufficient to treat such cases. Nevertheless, the moving ghosts method has also been extended to complex geometries in 3D [81, 100]. However, this method is not ideal for the treatment of these industrial complex geometries, in particular in presence of singularities. Boundary Integral Methods are preferred for such applications.

1.5.1.2 The Boundary Integral Method (BIM) with Cut-Face Approach (CFA)

This method was developed by different authors, *e.g.* [28, 23, 56]. In our laboratory it was developed within the Riemann-SPH scheme context, and its adaptation to the δ-SPH scheme is in progress. This development of the BIM method is reported here.

Near the domain boundaries, the property (1.10) is not verified since the kernel support is truncated. In order to solve this problem, the interpolation (1.8) can be rewritten as follows [23]:

$$\langle f\rangle(\mathbf{x})=\frac{1}{\gamma(\mathbf{x})}\int_\Omega f(\mathbf{y})W(\mathbf{x}-\mathbf{y},R_k)dV \tag{1.71}$$

where $\gamma(\mathbf{x})$ is the Shepard correction:

$$\gamma(\mathbf{x})=\int_\Omega W(\mathbf{x}-\mathbf{y},R_k)dV \tag{1.72}$$

The gradient and divergence operators (1.29) and (1.32) are then modified respectively as follows:

$$\begin{aligned}\langle \nabla P \rangle(\mathbf{x}) =& \frac{1}{\gamma(\mathbf{x})} \int_\Omega (P(\mathbf{y}) + P(\mathbf{x})) \nabla_\mathbf{x} W dV + \\ & \frac{1}{\gamma(\mathbf{x})} \int_{\partial\Omega} (P(\mathbf{y}) + P(\mathbf{x})) W(\mathbf{x}-\mathbf{y}, R_k) \mathbf{n} dS\end{aligned} \tag{1.73}$$

$$\begin{aligned}\langle \nabla \cdot \mathbf{u} \rangle(\mathbf{x}) =& \frac{1}{\gamma(\mathbf{x})} \int_\Omega (\mathbf{u}(\mathbf{y}) - \mathbf{u}(\mathbf{x})) \cdot \nabla_\mathbf{x} W dV + \\ & \frac{1}{\gamma(\mathbf{x})} \int_{\partial\Omega} (\mathbf{u}(\mathbf{y}) - \mathbf{u}(\mathbf{x})) \cdot \mathbf{n} W(\mathbf{x}-\mathbf{y}, R_k) dS\end{aligned} \tag{1.74}$$

Note that the second integral of each operator is no longer null as the kernel support intersects a wall. The domain frontier $\partial\Omega$ is then discretized into s control surfaces and the velocity divergence and pressure gradient operators are discretized as follows:

$$\langle \nabla P \rangle_i = \frac{1}{\gamma_i} \sum_{j \in \mathcal{F}} (P_i + P_j) \nabla_i W_{ij} V_j + \frac{1}{\gamma_i} \sum_{j \in \mathcal{W}} (P_i + P_j) W_{ij} \mathbf{n}_j s_j \tag{1.75}$$

$$\langle \nabla \cdot \mathbf{u} \rangle_i = \frac{1}{\gamma_i} \sum_{j \in \mathcal{F}} (\mathbf{u}_j - \mathbf{u}_i) \cdot \nabla_i W_{ij} V_j + \frac{1}{\gamma_i} \sum_{j \in \mathcal{W}} (\mathbf{u}_j - \mathbf{u}_i) \cdot \mathbf{n}_j W_{ij} s_j \tag{1.76}$$

where $\mathcal{F}$ and $\mathcal{W}$ denote respectively the set of neighboring particles belonging to the fluid and the set of faces discretizing the wall. In practice, $\mathbf{u}_j$ is replaced by the boundary condition velocity $\mathbf{u}_w$ in the surface integrals. Moreover, in our method p_j is replaced by a wall pressure p_w, which is computed as follows [31]:

$$P_w = P_i + \rho_j c_j \mathbf{u}_i \cdot \mathbf{n} \tag{1.77}$$

The improvement of the BIM method precision is the subject of many papers, notably concerning how to accurately compute the Shepard correction [28, 56] and the extension of the method to 3D configurations [102, 13].

The version used in the present PhD thesis is the Cut-Face Approach (CFA) presented in detail in [13].

1.5.2 Free-surface conditions in SPH

The interface between a light and a heavy phase can be considered as a free-surface if the evolution of the heavy phase is not affected by the light phase. This allows for simulations involving only the heavy phase, which are called "free-surface flows" throughout this work, *i.e.* the light phase is supposed to be void.

If no surface tension is taken into account, the dynamic condition along the free-surface states that the pressure is continuous across $\partial\Omega_F$, and equal to the external pressure p_e:

$$P = P_e, \quad \forall \mathbf{x} \in \partial\Omega_F \tag{1.78}$$

Since the light phase is not modeled, the kernel support near the free-surface is truncated, which means that the kernel interpolation naturally enforces the ambient pressure $P = P_e$ on the free-surface particles. Usually, a change of pressure origin leads SPH practitioners to consider $P = 0$ on the free-surface, which automatically means that the stress is null on this boundary. Indeed, Colagrossi et al. [16] proved, via the Principle of Virtual Works, that this dynamic free-surface boundary condition is intrinsically satisfied in a weak sense (using an integral formulation) within the SPH scheme, provided compatible operators are used in the continuity and momentum equations. This is a very important result which means that no additional treatment is needed in order to satisfy the free-surface boundary condition. For more details on the subject, the reader is referred to the original paper [16].

On the other hand, the kinematic free-surface condition states that a microscopic fluid particle initially on $\partial\Omega_F$ will remain on it, *i.e.*:

$$\mathbf{u} \cdot \mathbf{n}_F = \mathbf{u}_F \cdot \mathbf{n}_F, \quad \forall \mathbf{x} \in \partial\Omega_F \tag{1.79}$$

where $\mathbf{n}_F$ and $\mathbf{u}_F$ are respectively the normal to the free-surface and the free-surface velocity. Due to the Lagrangian nature of the SPH method, the fluid particles located at the free-surface move at a velocity equal to the free-surface velocity in the normal direction when $R_k \to 0$, which means that the free-surface kinematic condition is automatically satisfied [16].

1.5.3 Fluid/fluid interface conditions in SPH

At the interface between two fluids, the SPH differential operators take into account the particles belonging to both fluids, which results in smoothing out the physical quantities in the interface zone. This property is commonly assumed within the SPH community to ensure the continuity of the pressure and of the normal velocity across the interface, and consequently the kinematic and dynamic boundary conditions in the absence of surface tension effects [18, 42, 34].

However, this same property has the nonphysical effect of smoothing out other quantities of interest, mainly the density and the velocity divergence. This is undesirable since physically speaking, the tangential velocity (in the case of inviscid flows) and more importantly the density are not continuous across the interface. More light will be shed of this problem and how to solve it in Section 2.1.6.

1.6 Numerical tools in SPH

1.6.1 Particle disordering

The Lagrangian nature of SPH means that the particles naturally follow the Lagrangian trajectories. Therefore, flows involving strong stretching lead to an anisotropic evolution of the particle volumes, which in turn leads to linear particle structures. An illustration of such particle structures is presented in

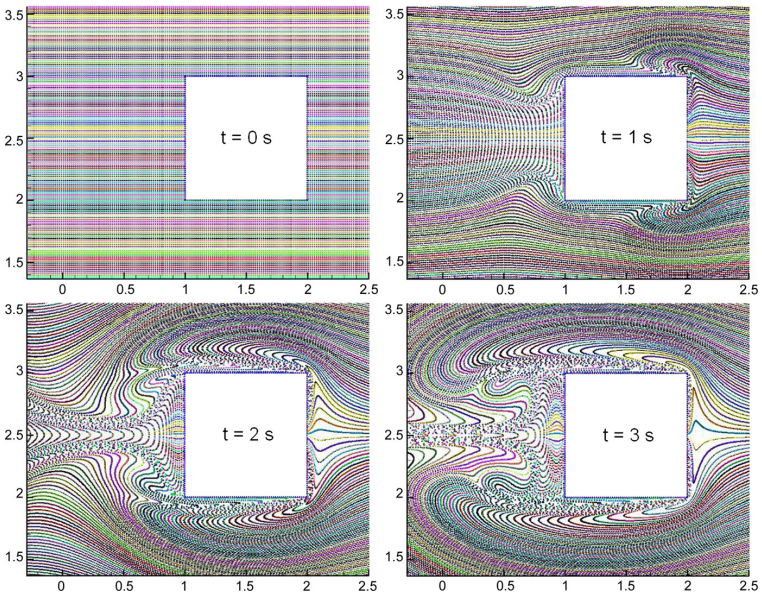

FIGURE 1.3: Evolution of the purely Lagrangian evolution of the flow past a square obstacle, taken from Colagrossi et al. [17], also cited in Oger et al. [83].

Fig. 1.3, which shows the purely Lagrangian evolution of the flow around a square-shaped obstacle [83].

For example at $t = 3s$, in the zone right to the square obstacle the particles distribution is highly anisotropic which leads to a creation of voids between the Lagrangian structures. These coherent structures affect the particles distribution inside the kernel support, which heavily decreases the accuracy of the SPH operators.

To circumvent this issue, some techniques were developed with the aim of introducing disorder within the particles distribution, in order to break the anisotropic alignment of particles. The following paragraphs sum up the main methods for disordering particles within the SPH community.

Monaghan [70] introduced a correction on the particles trajectory called XSPH, which rewrites the first equation of the system (1.34)-(1.37) as:

$$\frac{d\mathbf{x}_i}{dt} = \mathbf{u}_i + 2\epsilon \sum_j \left(\frac{\mathbf{u}_j - \mathbf{u}_i}{\rho_i + \rho_j} \right) W_{ij} \rho_j V_j \tag{1.80}$$

where the parameter ϵ is typically taken as 0.5. Although this method takes into account the free-surface, it does not necessarily converge towards the Euler equations, as the ϵ term is not guaranteed to tend towards 0 when $R_k \to 0$.

Oger et al. [83] introduced a transport velocity $\mathbf{u}_{oi}$ within an Arbitrary Lagrangian Eulerian (ALE) SPH formalism. In comparison with XSPH, this method is consistent with the Euler equations and reads, in the Riemann-SPH

context:

$$\begin{cases} \dfrac{d\mathbf{x}_i}{dt} = \mathbf{u}_{0i} \\ \dfrac{dV_i}{dt} = V_i \sum\limits_j (\mathbf{u}_{0j} - \mathbf{u}_{0i}) \cdot \nabla_i W_{ij} V_j \\ \dfrac{d(\rho_i V_i)}{dt} = -V_i \sum\limits_j 2\rho_E (\mathbf{u}_E - \mathbf{u}_0(\mathbf{x}_{ij})) \nabla_i W_{ij} V_j \\ \dfrac{d(\rho_i V_i \mathbf{u}_i)}{dt} = \rho_i V_i \mathbf{g} - V_i \sum\limits_j 2(\rho_E \mathbf{u}_E \otimes (\mathbf{u}_E - \mathbf{u}_0(\mathbf{x}_{ij})) + P_E \mathbb{I}) \nabla_i W_{ij} V_j \end{cases} \tag{1.81}$$

with $\mathbf{u}_{0i} = \mathbf{u}_i + \delta_{\mathbf{u}i}$ and $||\delta_{\mathbf{u}i}|| << ||\mathbf{u}_i||$. The idea is to slightly modify the Lagrangian velocity by adding a small velocity perturbation $\delta_{\mathbf{u}i}$ in order to break the anisotropic particle structures inherent to the SPH method, and to insert it consistently in the conservation laws through an ALE formalism. Oger et al. [83] proposed the following form of the velocity perturbation:

$$\delta_{\mathbf{u}i} = \begin{cases} -U^{char} R_{k,i} \tilde{\mathbf{n}} & \text{if } U^{char} R_{k,i} ||\tilde{\mathbf{n}}|| < 0.25 ||\mathbf{u}_i|| \\ -0.25 ||\mathbf{u}_i|| \dfrac{\tilde{\mathbf{n}}}{||\tilde{\mathbf{n}}||} \end{cases} \tag{1.82}$$

where the characteristic flow velocity $U^{char} = c_0 Ma$ controls the perturbation amplitude, and $\tilde{\mathbf{n}}$ is a vector pointing towards the voids:

$$\tilde{\mathbf{n}} = \sum_j \nabla W(\mathbf{x}_i - \mathbf{x}_j, R_\delta) V_j \tag{1.83}$$

Note that the radius R_δ is not necessarily equal to the kernel's support radius R_k. $R_\delta = 2\Delta x$ is prescribed in order to impose the anisotropy correction locally around the particle i.

Other methods have been developed for particle disordering, notably the Particle Shifting method by Lind et al. [45] and Xu et al. [108] which are based on Fick's law of diffusion. However, these are mainly used within the incompressible SPH (ISPH) framework, and are not detailed here. Later in this work, a particular case of the Oger et al. [83] law will be used, where the velocity is modified only in the trajectory equation.

1.6.2 Varying spatial resolution

1.6.2.1 Variable-h

In SPH the computations are usually performed using a uniform particle distribution, meaning that the inter-particle distance is the same everywhere in the domain. However, this is not ideal for example if the domain is very large in comparison to the characteristic size of the physics of interest.

To this aim, one idea is to refine the resolution in the zones of interest while coarsening it in the rest of the domain, in order to minimize the number

of particles involved, and consequently the computational cost and memory requirements.

In this context, varying spatial resolution techniques were introduced [40, 9, 78, 84, 37] which consist in slowly varying the kernel radius in time and space. From a theoretical point of view, these methods should account for the time and space derivatives of R_k in order to satisfy conservation requirements.

Oger et al. [84] considered a technique in which the kernel support of each particle stays constant in time so that $dR_k/dt = 0$. In the same time, the kernel radius must vary in space slowly enough so as to make it possible to neglect the ∇R_k terms in the equations, while avoiding reflection of acoustic waves between the coarse and fine zones. Typically, this is achieved through limiting the spatial evolution of R_k between adjacent particles to a maximum value of 3%.

There are many variable-h formulations in the literature [81, 9]. In this work, in order to conserve the reciprocity of interactions, the kernel radius R_k in $W(\mathbf{x}_i - \mathbf{x}_j, R_k)$ is taken equal to the half-sum $R_{k,ij} = (R_{k,i} + R_{k,j})/2$, as suggested in [37].

However, while a regular space distribution of the kernel radii is guaranteed at the start of the simulations, this situation can degrade later on due to the Lagrangian nature of the SPH method. Indeed, the particles are allowed to move according to the computed fluid velocity, which can lead to numerically unstable configurations where coarse and fine particles are improperly mixed. To circumvent this problem, other approaches were developed, based on local particle refinement.

1.6.2.2 Adaptive Particle Refinement

Particle refinement procedures were developed which aim to locally refine the resolution based on a chosen criterion, such as velocity gradient or density. The adaptivity aspect of such procedures lies in the fact that the refinement algorithm is applied and updated automatically throughout the simulations.

Initially proposed by Feldman [28], the fundamental idea of these procedures is to split the coarse particles, called 'parents', into several smaller particles, referred to as 'children'. The properties of the smaller particles are computed in a way that looks to conserve mass, momentum and energy.

Conversely, derefinement techniques are also made possible simply by reciprocating the refinement procedure as initially proposed by Vacondio et al. [98]. The child particles are merged into parent particles, coarsening the distribution whenever needed. Different derefinement techniques are available in the literature [98, 5].

Dynamic refinement/derefinement methods were investigated within the LHEEA laboratory. After an initial proposal by Barcarolo et al. [5], Chiron et al. [12] proposed an improved refinement technique called Adaptive Particle Refinement (APR), based on the Adaptive Mesh Refinement (AMR) technique of the mesh-based methods [6]. Its robustness and accuracy at the

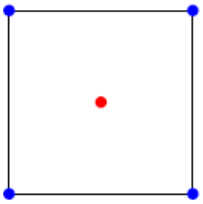

FIGURE 1.4: A parent particle (red) is split into four children particles (blue). Picture from Chiron et al. [12].

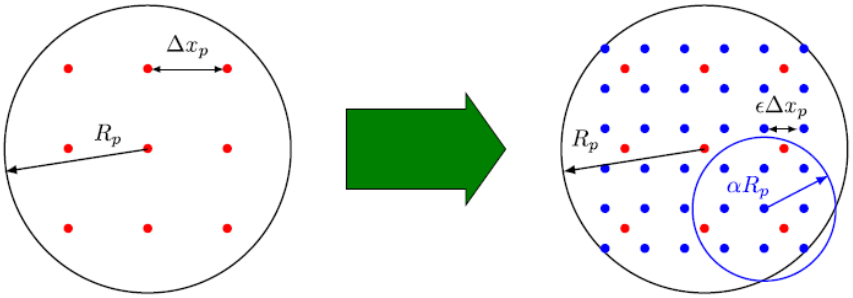

FIGURE 1.5: Particle refinement process. Here $\alpha = 0.5$ and $\epsilon = 0.5$. Picture from Chiron et al. [12].

coarse/fine interfaces was demonstrated. It also yielded results similar to fully refined spatial resolutions in terms of accuracy, but with much lower CPU times. The next section details the most important aspects of APR in 2D. The reader is referred to the original paper [12] for extensive details.

As proposed in Reyes López et al. [93], a parent particle is refined into four child particles as shown in Fig. 1.4. The radius of child particles and the spacing between them are defined following (see Fig. 1.5):

$$\Delta x_c = 0.5 \Delta x_p \tag{1.84}$$

and their radius is defined as:

$$R_c = 0.5 R_p \tag{1.85}$$

Throughout the refinement process the properties of child particles are ideally defined in a conservative way. For example, the mass of a child particle is computed as:

$$m_c = \frac{m_p}{4} \tag{1.86}$$

which ensures mass conservation.

The energy and momentum can be conserved simply by copying the parent velocity to the child particles. This is called injection. However this method is not considered to be sufficiently accurate. An alternative way of initializing the properties of the child particles can be drawn out from the Adaptive Mesh Refinement method used for structured Cartesian grid solvers (based on Finite Volumes for example) [6]. The initialization of child variables is done by prolongation, which means that the fine particle values

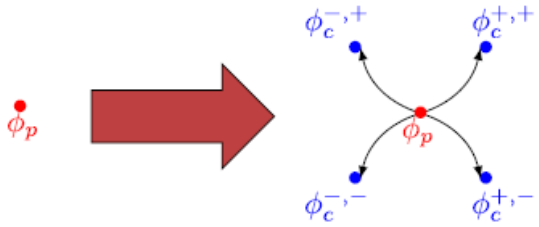

FIGURE 1.6: Prolongation procedure: the values of child particles are extrapolated from the parent particle. Picture from Chiron et al. [12].

ϕ_c are interpolated from the coarse particle ones ϕ_p (Fig. 1.6). A straightforward linear interpolation is used as follows:

$$\phi_c = \phi_p + \nabla(\phi)_p \cdot (\mathbf{x}_c - \mathbf{x}_p) \tag{1.87}$$

where $\nabla(\phi)_p$ is the parent particle's gradient of conservative variables. Here $\nabla(\phi)_p$ is computed through a renormalized gradient operator:

$$\nabla(\phi)_i = \mathcal{L}_i \cdot \sum_{j \in \Omega_p} (\phi_i - \phi_j) \otimes \nabla_i W_{ij} V_j \tag{1.88}$$

where $\mathcal{L}_i$ is the renormalized matrix given by Eq. (1.42) in Section 1.3.3.2, calculated only over the set of parent particles Ω_p. Note that unlike the injection method, this prolongation (1.87) technique conserves momentum but does not conserve kinetic energy nor angular momentum.

We have seen how the child particle properties are computed throughout the refinement technique. As for the reciprocal derefinement process, when child particles are merged, the properties of the ensuing parent particles must also be initialized. This is referred to as restriction. As seen in Section 1.3.3.1, in SPH the Shepard interpolation is usually used for field evaluation at a given location. Here the restriction process uses a Shepard interpolation over the set of child particles Ω_c, for any field ϕ:

$$\phi_p = \sum_{j \in \Omega_c} \phi_j W^S_{pj} V_j \tag{1.89}$$

where W^S is the Shepard kernel given by (1.39).

So far the child/parent particles values are computed through the (de)refinement process. However, this method still needs to be improved since adjacent coarse and fine particles have a radius ratio of 50%. This ratio is greater than the recommended value of 3% which can lead to numerical instabilities. Therefore, the child and parent particles still cannot interact directly with each other.

To circumvent this problem, the concept of guard cells of AMR is extended to the particular formalism of SPH. A third set of particles is created from either side of the coarse/fine interface, called guard particles. Their role is to act as boundary conditions of a SPH/SPH-like coupling between

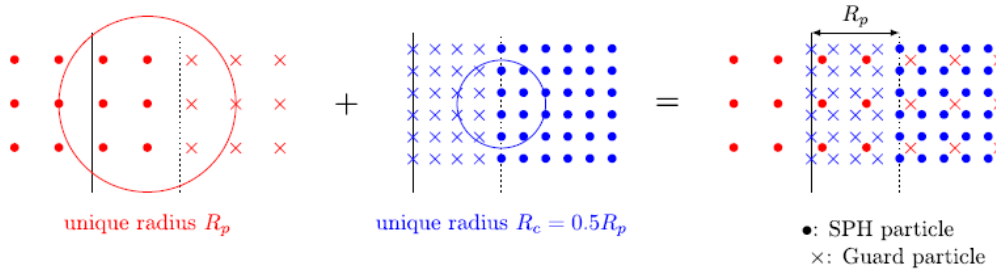

FIGURE 1.7: The child/parent guard particles are created at the fine/coarse interface. The coupling between both refinement levels is ensured via the guard particles. Picture from Chiron et al. [12].

the coarse and fine domains. The conservative variables of the guard particles are computed using the restriction operation over the neighboring parent and child particles, which ensures the coupling between the two refinement levels [12]. Note that this interpolation is carried out using the child particle radius for both parent and child guard particles, in order to minimize CPU times.

Therefore, as illustrated in Fig. 1.7, the APR method used in this work goes as follows:

- At the beginning of each substep of the temporal integration scheme, the guard particles × and × are initialized using a restriction operation.
- The derivatives of the child particles • are updated, taking into consideration both guard × and child • particles.
- Parent particles • are updated taking into account both guard × and parent • particles.

One last note concerns the concept of adaptivity. The adaptivity of AMR means that the refinement process is based on physical criteria, for examples in zones of high vorticity, of density gradients, etc. This is not the case for the present APR method. The adaptive aspect of APR lies behind the dynamic refinement zones that this method offers. For example, in practice many boxes covering the interest zone can be created, with increasing refinement levels. Moreover, a velocity can be associated to these boxes so that they can move inside the domain if required, as will be seen in Chapter 5 which is dedicated to the ditching simulations.

Chapter 2

Proposition of an accurate multiphase scheme

2.1 Multiphase SPH

2.1.1 Overview

Many hydrodynamic problems involve several non-mixing phases, possibly with high density ratios such as air-water problems. Many applications necessitate taking into account the presence of air, *e.g.* in the case of air trapping/cushioning. Thanks to its mesh-less and Lagrangian nature, the SPH method is well suited for simulating flows where two fluids with different densities interact as it allows to keep perfectly non-diffusive interfaces, unlike Eulerian numerical methods where interface tracking is necessary, possibly with difficulties due to numerical interface smearing.

Yet, when the density ratios become large, many difficulties arise at the interface between the fluids. Indeed, the equations of the Standard Scheme are suitable for single-phase flows where the variables are continuous without sharp jumps. However, in the case of flows where different fluids coexist, the density is discontinuous at the interface between these fluids. The classic SPH interpolation for the continuity equation leads to diffused density jumps especially if the density ratio is high. Therefore, one of the most important challenges facing the SPH community is to find ways to discretize the continuity and momentum equations so as to avoid the complete smoothing out of the density jumps across the interface between two different fluids.

A sound discretization of the $\nabla \cdot \mathbf{u}$ and $\nabla P/\rho$ terms in the continuity and momentum equations, respectively, is generally key for simulating multiphase flows. In the case of simulations involving fluids with high density ratios, a large density gradient exists at the interface. This means that the equations should not encapsulate any formulation involving $\nabla \rho$ terms, at the risk of facing very strong numerical instabilities.

From all the possible symmetrized discretization of the Euler equations [84]:

$$\begin{cases} \dfrac{\nabla P}{\rho} = \dfrac{P}{\rho^{\sigma}}\nabla\left(\dfrac{1}{\rho^{1-\sigma}}\right) + \rho^{\sigma-2}\nabla\left(\dfrac{P}{\rho^{\sigma-1}}\right), & \sigma \in \mathbb{R}^{+} \\ \rho\nabla\cdot\mathbf{u} = \dfrac{\nabla\cdot(\rho^{\sigma-1}\mathbf{u}) - \mathbf{u}\cdot\nabla\rho^{\sigma-1}}{\rho^{\sigma-2}} \end{cases} \tag{2.1}$$

only the case $\sigma = 1$ prohibits the existence of $\nabla\rho$ in the equations, which coincides exactly with the Standard Scheme (1.34)-(1.37).

As already pointed out in Section 1.5, it is very important to note the difference between what is called an "interface" and a "free-surface" throughout this work. For example in the case of air-water simulations, an interface implicates the modeling of both the water and the air phases, while the free-surface assumption means that only the water is modeled.

In this chapter, a new weakly-compressible multiphase SPH scheme is proposed, called the Multiphase δ-SPH scheme. It is capable of handling large density ratios and the presence of both interfaces and a free-surface, as well as yielding quality pressure fields. In order to understand the logical path towards this new scheme, the next sections will first present a summary of the main weakly-compressible multiphase SPH formulations in chronological order. They will include the specificities of each scheme in terms of the governing equations formulation for multiphase configurations, numerical tools for stabilization and accuracy improvements, together with some advantages and drawbacks of each scheme.

2.1.2 Colagrossi and Landrini scheme (2003)

In 2003, Colagrossi and Landrini [18] derived the first SPH multiphase model able to treat high density ratios. Despite being developed more than 15 years ago, it is still one of the most used multiphase schemes within the SPH community.

Colagrossi and Landrini kept the governing equations of the Standard Scheme (1.34)-(1.37). As explained in the previous section, they offer the advantage of not involving any $\nabla\rho$ terms. In order to remove nonphysical high-frequencies from the pressure field, they used a density filtering technique:

$$\langle\rho_i\rangle = \sum_j \rho_j W_j^{MLS}(\mathbf{x}_i) dV_j = \sum_j m_j W_j^{MLS}(\mathbf{x}_i) \tag{2.2}$$

where the moving-least-square kernel W_j^{MLS} is computed, *e.g.* in 2D, through:

$$\begin{cases} W_j^{MLS}(\mathbf{x}_i) = [\beta_0(\mathbf{x}_i) + \beta_1(\mathbf{x}_i)(x_i - x_j) + \beta_2(\mathbf{x}_i)(y_i - y_j)]W_{ij} \\ \beta(\mathbf{x}_i) = \begin{bmatrix} \beta_0 \\ \beta_1 \\ \beta_2 \end{bmatrix} = A^{-1}(\mathbf{x}_i) \begin{bmatrix} 1 \\ 0 \\ 0 \end{bmatrix} \\ A(\mathbf{x}_i) = \sum_j W_j(\mathbf{x}_i)\tilde{A}_{ij} \\ \tilde{A}_{ij} = \begin{bmatrix} 1 & (x_i - x_j) & (y_i - y_j) \\ (x_i - x_j) & (x_i - x_j)^2 & (y_i - y_j)(x_i - x_j) \\ (y_i - y_j) & (y_i - y_j)(x_i - x_j) & (y_i - y_j)^2 \end{bmatrix} \end{cases} \tag{2.3}$$

This procedure is carried out at a chosen frequency, *i.e.* at every chosen number of time steps, increasing the computational time due to the inversion of the matrix A for each fluid particle i. However, it presents advantages concerning more regular pressure distribution for both interfacial and free-surface flows. However, it introduced numerical instabilities close to the free-surface for long time simulations (i.e. large number of time steps). For instance, it does not preserve an hyperbolic situation. It is also not conservative.

For stabilization, Colagrossi and Landrini used a modified version of the Monaghan and Gingold artificial viscosity presented in Section 1.4.1. Through dam-break tests they showed that their version of the artificial viscosity coupled with the density filtering technique improves the total energy conservation. However, the modified artificial viscosity increases computational time as it requires an additional loop over the particles. Also for multiphase flows, the artificial viscosity terms are computed for each particle i considering exclusively particles j belonging to the same fluid.

Colagrossi and Landrini also used the XSPH velocity correction discussed in Section 1.6.1 which was shown to significantly improve the accuracy of the two-phase flows solutions. The XSPH correction was used only within the continuity equation, which was rewritten as follows:

$$\nabla.\mathbf{u}_i = \sum_j (\mathbf{u}_j - \mathbf{u}_i).\nabla W_{ji}\frac{m_j}{\rho_j} + \sum_j (\triangle\mathbf{u}_j - \triangle\mathbf{u}_i).\nabla W_{ji}\frac{m_j}{\rho_j} \tag{2.4}$$

where

$$\triangle\mathbf{u}_i = \frac{\epsilon}{2}\sum_j \frac{m_j}{\bar{\rho}_{ij}}(\mathbf{u}_j - \mathbf{u}_i)W_{ji} \tag{2.5}$$

and $\bar{\rho}_{ij} = \dfrac{\rho_i + \rho_j}{2}$.

For two-phase flows a constant background pressure p_0 is added to the Cole equation of state in confined domains to avoid tensile instability, and it is equal to 0 for free-surface flows. Moreover, in order to prevent particles mixing and keep the interface sharp, a cohesive force was also added to the

equation of state, which is rewritten as follows:

$$P(\rho) = \frac{\rho_0 c_0^2}{\gamma}\left[\left(\frac{\rho}{\rho_0}\right)^{\gamma} - 1\right] + p_0 - \bar{a}\rho^2 \tag{2.6}$$

where the last term, adopted from Nugent and Posch [80], acts as a cohesion force and the paramerter $\bar{a}$ controls its strength. The cohesion force acts only on the particles belonging to the lighter fluid Y.

2.1.3 Hu and Adams scheme (2006)

Another widely used scheme today is the Hu and Adams [42] formulation for multiphase SPH. It is based on the following approximation of the particle densites:

$$\rho_i = m_i / V_i = m_i \sum_j W_{ij} \tag{2.7}$$

where m_i is the mass associated to particle i, and V_i is approximated from the neighboring repartition of particles as $1/\sum_j W_{ij}$.

This formulation is able to take into account density discontinuities between different fluids since the the evaluation of the density of a particle i does not depend on the density of its neighboring particles, but only on their positions and kernel radii.

Nevertheless, the major drawback of the interpolation (2.7) is that it cannot be used for flows involving a free-surface since the kernel support is truncated in the free-surface region, which results in erroneous densities in this zone. However, the advantage of this method lies in the fact that there is no need for a temporal integration of a continuity equation, which guarantees mass conservation.

Grenier [33] proved the compatibility of the momentum equation proposed in the Hu and Adams model [42] with the density formulation (2.7) through a variational approach. A similar demonstration will be detailed in Section 2.3. The momentum equation of the Hu and Adams scheme reads:

$$m_i \frac{d\mathbf{u}_i}{dt} = -\sum_j (P_i V_i^2 + P_j V_j^2)\nabla_i W_{ij} + m_i \mathbf{g} \tag{2.8}$$

2.1.4 Multiphase Riemann-SPH scheme (2010)

The Riemann-SPH scheme developed by Vila and presented in Section 1.4.3 can be adapted to multiphase configurations by blocking mass fluxes between the particles at the interface between two fluids. The interfaces between particles of different fluids are considered here as contact discontinuities, which translates into taking the velocity of the interface between the particles equal to the velocity of the solution of the Riemann problem:

$$\mathbf{u}(\bar{\mathbf{x}}_{ij}) = \mathbf{u}_E \tag{2.9}$$

Therefore, the mass and momentum equations (1.57) and (1.58) of the Vila scheme, presented in Section 1.4.3, become:

$$\frac{d(\rho_i V_i)}{dt} = 0 \tag{2.10}$$

$$\frac{d(\rho_i V_i \mathbf{u}_i)}{dt} = \rho_i V_i \mathbf{g} - V_i \sum_j 2P_E \nabla_i W_{ij} V_j \tag{2.11}$$

The velocity solution of the Riemann problem is also introduced within the volume equation (1.56):

$$\frac{dV_i}{dt} = V_i \sum_j (\mathbf{u}_j - \mathbf{u}_i) \cdot \nabla_i W_{ij} V_j \tag{2.12}$$

$$= V_i \sum_j 2\left(\frac{\mathbf{u}_j + \mathbf{u}_i}{2} - \mathbf{u}_i\right) \cdot \nabla_i W_{ij} V_j \tag{2.13}$$

$$= V_i \sum_j 2(\mathbf{u}_E - \mathbf{u}_i) \cdot \nabla_i W_{ij} V_j \tag{2.14}$$

Consequently, we get the following system of discrete equations [54]:

$$\begin{cases} \dfrac{d\mathbf{x}_i}{dt} = \mathbf{u}_i & (2.15) \\ \dfrac{dV_i}{dt} = V_i \displaystyle\sum_j 2(\mathbf{u}_E - \mathbf{u}_i) \cdot \nabla_i W_{ij} V_j & (2.16) \\ \dfrac{d(\rho_i V_i)}{dt} = 0 & (2.17) \\ \dfrac{d(\rho_i V_i \mathbf{u}_i)}{dt} = \rho_i V_i \mathbf{g} - V_i \displaystyle\sum_j 2P_E \nabla_i W_{ij} V_j & (2.18) \end{cases}$$

This scheme was shown to handle large density ratios and avoid interface or pressure jump diffusion, while being very robust and stable [54]. However, it still requires the MUSCL method to avoid too much numerical dissipation (Section 1.4.3).

Moreover, this scheme does not allow mass fluxes which means that it cannot be written in an ALE formalism (contrary to the ALE version of the Vila scheme, (1.55)-(1.58)). However, in order to eliminate the anisotropic structures, it is still possible to move the particles at an arbitrary velocity, although non-consistently, through replacing Eq. (2.15) by:

$$\frac{d\mathbf{x}_i}{dt} = \mathbf{u}_{0i} \tag{2.19}$$

where $\mathbf{u}_{0i}$ is a velocity perturbation, *e.g.* the one proposed by Oger et al. [83] and presented in Section 1.6.1, which is the particle shifting technique used in conjunction with the Riemann-SPH scheme (2.15)-(2.18) throughout this work.

2.1.5 Monaghan and Rafiee scheme (2012)

The SPH form of the continuity equation adopted by Monaghan and Rafiee [75] is the standard one, *cf.* Eq. (1.35).

The momentum equation is retrieved through the derivation of the acceleration of particle i from Lagrange's equations, which yielded the expression of the momentum equation given in Eq. (1.36).

To stabilize their scheme, they added the viscosity term Π_{ij} (*cf.* Section 1.4.1) to the momentum equation, which reads:

$$\Pi_{ij} = -\frac{8\bar{\nu}_{ij}\mathbf{u}_{ij}\cdot\mathbf{x}_{ij}}{\bar{\rho}_{ij}|\mathbf{x}_{ij}|\bar{h}_{ij}} \tag{2.20}$$

where ν is the kinematic viscosity, and the notation $\bar{\rho}_{ij} = (\rho_i + \rho_j)/2$ is used. If the viscosity ratio between the considered fluids is large, the following replacement is made in Eq. (2.20):

$$\frac{\bar{\nu}_{ij}}{\bar{\rho}_{ij}} \rightarrow \frac{2\nu_i\nu_j}{\nu_i\rho_i + \nu_j\rho_j} \tag{2.21}$$

Moreover, a numerical treatment is enforced at the interface through adding a repulsive term R_{ij} between fluids of different types to the momentum equation, similarly to the one suggested by Monaghan in [74]. This repulsive force reads:

$$R_{ij} = 0.08\left|\frac{\rho_{0i}-\rho_{0j}}{\rho_{0i}+\rho_{0j}}\right|\left|\frac{P_i+P_j}{\rho_i\rho_j}\right| \tag{2.22}$$

Thus, the momentum equation of the Monaghan and Rafiee model reads (excluding boundary forces [75]):

$$\frac{d\mathbf{u}_i}{dt} = -\sum_j m_j\left(\frac{P_i+P_j}{\rho_i\rho_j} + R_{ij} + \Pi_{ij}\right)\nabla_i W_{ij} \tag{2.23}$$

Similarly to the Standard Scheme, the density is updated in time which makes the multiphase model of Monaghan and Rafiee capable of handling the presence of a free-surface. However, no information concerning the quality of pressure field was provided in their paper. Also, their scheme necessitates a damping technique in order to correctly initialize the simulation. Furthermore, their results showed visible nonphysical perturbations at the interface between two fluids with a medium density ratio of 100 (*e.g* Figure 3 in [75]).

2.1.6 Grenier et al. scheme (2013)

Grenier et al. [35] proposed a multiphase model for interfacial and free-surface flows. This scheme is detailed more than the previous ones here since it will be the basis for the scheme proposed in this thesis which extends it.

The continuity equation is expressed through the Volumetric Strain Rate equation:

$$\frac{d(\delta V)}{dt} = \delta V \mathrm{div}(\mathbf{u}) \tag{2.24}$$

where δV is the volume associated to the material point which moves with the flow velocity $\mathbf{u}$.

As usually performed in the SPH framework, the divergence operator can be approximated as:

$$\langle \mathrm{div}(\mathbf{u}) \rangle_i = \sum_j (\mathbf{u}_j - \mathbf{u}_i) \cdot \nabla_i W_{ij} V_j \tag{2.25}$$

From the above equations, the time evolution for the particle volumes can be derived as:

$$\frac{dV_i}{dt} = V_i \langle \mathrm{div}(\mathbf{u}) \rangle_i \tag{2.26}$$

and the mass m_i of the generic particle i is evaluated by the initial condition at time $t = 0$:

$$m_i = \rho_{i0} V_{i0} \tag{2.27}$$

where ρ_{i0} and V_{i0} are respectively the initial density and volume of particle i. Once the particle masses are initialized they do not change throughout the simulation, which explicitly guarantees mass conservation. Furthermore, a discussion about the volumes initialization is provided in Section 2.3.

The Grenier et al. [35] model differs from other SPH models where a continuity equation is written in terms of density. Indeed, in Grenier et al. [35] the particle volumes are evaluated before the density, similarly to the Español and Revenga [27] model. Here, after the time integration of (2.26), a Shepard interpolation of the particles masses is used to evaluate the density field:

$$\rho_i = \sum_{j \in \chi} m_j W^S_{ij}; \quad W^S_{ij} = \frac{W_{ij}}{\sum\limits_{k \in \chi} W_{ik} V_k}, \quad \forall i \in \chi \tag{2.28}$$

where χ indicates a generic fluid in the domain Ω, with the above summations computed only using particles belonging to the same phase as particle i. This allows for an explicit treatment of the density discontinuities since, unlike the kernel W_{ij}, the summation of the Shepard kernel is not affected by the truncation of the kernel support. Also, it is worth noting that the Shepard kernel W^S requires a priori the knowledge of the particles volumes V_k in Eq. (2.28), yielded by the evolution equation (2.26).

Once the density field is evaluated, the pressure is obtained through the use of the equation of state (1.4), for each phase χ:

$$P_i = f_\chi(\rho_i) = \frac{\rho_{0\chi} c^2_{0\chi}}{\gamma_\chi} \left[\left(\frac{\rho_i}{\rho_{0\chi}} \right)^{\gamma_\chi} - 1 \right] + p_0, \quad \forall i \in \chi \tag{2.29}$$

where γ_χ, $\rho_{0\chi}$ and $c_{0\chi}$ are respectively the polytropic coefficient, nominal density and nominal sound speed of phase χ.

Following the work of Colagrossi et al. [16], using the Principle of Virtual Works, the smoothed divergence operator defined by (2.25) leads to the following smoothed pressure gradient:

$$\langle \nabla P \rangle_i = \sum_j (P_i + P_j) \nabla_i W_{ij} V_j \tag{2.30}$$

Since the Shepard kernel is used in (2.28), in [34] the smoothed velocity divergence and the smoothed pressure gradient operators were modified as:

$$\begin{cases} \langle \text{div}(\mathbf{u}) \rangle_i = \sum_j (\mathbf{u}_j - \mathbf{u}_i) \dfrac{\nabla_i W_{ij}}{\Gamma_i} V_j, \quad \langle \nabla P \rangle_i = \sum_j \left(\dfrac{P_i}{\Gamma_i} + \dfrac{P_j}{\Gamma_j} \right) \nabla_i W_{ij} V_j \\ \Gamma_i = \sum_k W_{ik} V_k \end{cases} \tag{2.31}$$

where Γ_i is a renormalization factor that takes into account possible kernel support truncation. However, unlike the summation used in (2.28) for the evaluation of densities, the summation for the Γ_i factor incorporates the particles belonging to other phases as well.

Grenier et al. [34] underlined the fact that a non-physical inter-penetration of particles from different phases may occur when simulating multiphase flows where surface tension effects are negligible. In order to prevent this, a small repulsive force was introduced within the pressure gradient operator as follows [34]:

$$\nabla P_i = \sum_j \left(\frac{P_i}{\Gamma_i} + \frac{P_j}{\Gamma_j} \right) \nabla_i W_{ij} V_j + \epsilon_\chi \sum_{j \in \bar{\chi}} \left(\left| \frac{P_i}{\Gamma_i} \right| + \left| \frac{P_j}{\Gamma_j} \right| \right) \nabla_i W_{ij} V_j \tag{2.32}$$

where ϵ_χ is a parameter ranging between 0.01 and 0.1 that controls the intensity of the repulsive term. The second summation applies only to the set of particles that do not belong to the fluid of the i^{th} particle. This set of particles is noted by $\bar{\chi}$. This choice naturally implies that on the free-surface, this artificial pressure term is null.

2.1.7 Summary

In the previous sections we have seen that there multiple ways to derive SPH-discretized governing equations for the aim of multiphase configurations. Each method has its advantages and drawbacks, especially regarding their capabilities in terms of handling the presence of a free-surface, stabilization methods and quality of the pressure fields.

That being said, the Grenier et al. model [35] is able to treat multiphase flows in the presence of both interfaces and a free-surface. However, like other weakly-compressible SPH schemes, it suffers from numerical high-frequency oscillations within the pressure field. Therefore, one of the problems tackled during this thesis is the improvement of the Grenier et al. model, both in terms of computed pressure fields and stability. The next section will present the contributions of this work in this context.

2.2 Derivation of the Multiphase δ-SPH scheme

2.2.1 The proposed governing equations of the Multiphase δ-SPH scheme

Grenier et al. [35] modified the smoothed velocity divergence and pressure gradient operators by introducing a renormalization factor Γ_i (Eqs. (2.31)), for taking into account possible kernel truncation. However, conversely to the summation used in Eq. (2.28) for the evaluation of densities, the summation for the Γ_i factors incorporates the particle belonging to other phases as well. It follows that Γ_i remains close to unity and plays a role only when the particles are close to the free-surface. From a practical point of view we found that the effects of the Γ_i terms are always negligible. Their use does not improve the accuracy of the scheme and for this reason, they will not be adopted in the rest of this work. A simple heuristic proof of this is given in Section 3.2.

Therefore, we propose to rewrite the velocity divergence and pressure gradient operators (2.31) of the Grenier et al. scheme, as:

$$\langle \mathrm{div}(\mathbf{u}) \rangle_i = \sum_j (\mathbf{u}_j - \mathbf{u}_i) \nabla_i W_{ij} V_j \tag{2.33}$$

$$\langle \nabla P \rangle_i = \sum_j (P_i + P_j) \nabla_i W_{ij} V_j \tag{2.34}$$

More precisely, the modified pressure gradient proposed by Grenier et al. [34] was kept here, the only difference being the elimination of Γ_i factors from the equation:

$$\nabla P_i = \sum_j (P_i + P_j) \nabla_i W_{ij} V_j + \epsilon_\chi \sum_{j \in \bar{\chi}} (|P_i| + |P_j|) \nabla_i W_{ij} V_j \tag{2.35}$$

In order to remove the spurious oscillations of pressure that challenge the Grenier et al. scheme, we developed a simple yet effective treatment, inspired from the single-phase δ-SPH model of Antuono et al. [1]. Indeed, the diffusive δ-term presented in Section 1.4.2 was identified as a good candidate to extend to the multiphase framework.

Therefore, the complete set of ODEs for the proposed model, referred to as the Multiphase δ-SPH scheme in this work, written for a generic i^{th} particle

of a generic phase χ, is:

$$\begin{cases} \dfrac{d\mathbf{x}_i}{dt} = \mathbf{u}_i & (2.36) \\ \dfrac{dV_i}{dt} = V_i \sum_j (\mathbf{u}_j - \mathbf{u}_i) \cdot \nabla_i W_{ij} V_j + \delta h c_{0\chi} \sum_{j \in \chi} \psi_i^{VSR} \cdot \nabla_i W_{ij} V_j & (2.37) \\ \rho_i \dfrac{d\mathbf{u}_i}{dt} = -\sum_j (P_i + P_j) \nabla_i W_{ij} V_j + \rho_i \mathbf{g}_i + \alpha h c_{0\chi} \rho_{0\chi i} \sum_{j \in \chi} \pi_{ij} \nabla_i W_{ij} V_j & (2.38) \\ \rho_i = \sum_{j \in \chi} m_j W_{ij}^S & (2.39) \\ P_i = f_\chi(\rho_i) & (2.40) \end{cases}$$

The next section details the adaptation of the δ-SPH diffusive term ψ_i^{VSR} to the governing equations of the proposed Multiphase δ-SPH scheme.

2.2.2 The proposed diffusive term in the Volumetric Strain Rate equation

First, it is important to note that some fundamental differences exist between the governing equations of the Grenier et al. scheme and the Standard Scheme, which makes the adaptation of the diffusive δ-term not straightforward.

On the one hand, the δ-SPH diffusive term is added to equation (1.35) of the Standard Scheme which is a continuity equation written in terms of density, whereas in the Multiphase δ-SPH scheme a continuity equation does not exist per se. Instead it is replaced by a Volumetric Strain Rate (VSR) equation, while the density is computed via a Shepard interpolation. Therefore, any numerical diffusion to improve the pressure field should be added to the Volumetric Strain Rate equation and not to the Shepard interpolation of the density. Indeed, the main reason of computing density via a Shepard interpolation is to avoid any numerical diffusion at the interface between two different fluids in a multiphase context, and directly mixing it with a numerical diffusive term would defeat its purpose.

On the other hand, as seen for the δ-SPH scheme, in the continuity equation the δ-diffusive term has the dimension of a Laplacian of density. Since the Volumetric Strain Rate equation has the same form as the δ-SPH continuity equation, the correction terms in both equations should take the same form. Consequently, the numerical diffusive term within the Volumetric Strain Rate equation should logically have the dimension of a Laplacian of volume.

An intuitive approach is to directly replace the density by the volume inside the diffusive term, as follows:

$$\mathcal{D}_i^{VSR} = \sum_j \psi_{ij}^{VSR} \cdot \nabla_i W_{ij} V_j \tag{2.41}$$

where the superscript VSR denotes the terms adapted to the Volumetric Strain Rate equation, and:

$$\psi_{ij}^{VSR} = 2(V_j - V_i)\frac{\mathbf{x}_{ji}}{||\mathbf{x}_{ij}||^2} - [\langle \nabla V \rangle_i^{\mathcal{L}} + \langle \nabla V \rangle_j^{\mathcal{L}}] \tag{2.42}$$

This form of the diffusive term was tested on two problems, a dam-break and a hydrostatic case, both in a single-phase configuration as a first attempt. The results for the dam-break case were quite satisfactory, with smooth pressure all over the domain. However, the same formulation of the numerical diffusive term led to a solution that did not preserve the hydrostatic solution, where the particles near the free-surface tended to move upwards. This problem was also reported in Antuono et al. [1].

This nonphysical behavior of the particles near the free-surface can be explained by the fact that in a simulation like the hydrostatic problem, the variation of the particle volumes within the kernel support are very small, which means that the spatial gradient of the volumes is negligible. Therefore, the adapted correction term $\langle \nabla V \rangle_i^{\mathcal{L}} + \langle \nabla V \rangle_j^{\mathcal{L}}$ almost vanishes for the hydrostatic case, meaning that the diffusive term is simply reduced to its original form:

$$\psi_{ij}^{VSR} \approx 2(V_j - V_i)\frac{\mathbf{x}_{ji}}{||\mathbf{x}_{ij}||^2} \tag{2.43}$$

which diverges at the free-surface as already established in Section 1.4.2, rendering unstable the particles near the free-surface. Note that this problem does not affect the dam-break simulation since it involves complex movements of the particles, during which the gradient of volume has generally non-zero values.

Consequently, this problem was circumvented by adopting the following form of the numerical diffusive term:

$$\psi_i^{VSR} = V_i\left[2\left(1 - \frac{\rho_j}{\rho_i}\right) - \frac{1}{\rho_i}\left(\nabla\rho_i^{\mathcal{L}} + \nabla\rho_j^{\mathcal{L}}\right)\cdot\mathbf{x}_{ij}\right]\frac{\mathbf{x}_{ij}}{||\mathbf{x}_{ij}||^2} \tag{2.44}$$

In terms of dimension, this form of the diffusive term is still written for the particle volumes and not for the density as in Eq. (1.54), so it is compatible with the Volumetric Strain Equation. Moreover, the diffusion is still dependent on the density variations, which also keeps it suitable for free-surface flows.

In the Multiphase δ-SPH scheme (2.36)-(2.40), the parameter δ is always set to 0.1 independently of the simulation and $\alpha = \mathcal{O}(0.1)$, similarly to the single-phase δ-SPH model [62] (Section 1.4.2). Note that the sums in the density and in the diffusive terms are made only over particles of the same phase as particle i, as was proposed by Colagrossi et al. [18] and Grenier et al. [34, 35]. This is motivated by the fact that we do not want to alter the explicit treatment of the interface discontinuities by allowing a diffusion mechanism across the different phases. However, such a choice can lead to numerical instabilities at these interfaces which necessitates the addition of a numerical

surface tension term, as underlined in Section 2.1.6.

2.3 Alternative derivation of the Multiphase δ-SPH scheme equations

The starting point of the derivation of the second set of governing equations is to define the volume of a generic i^{th} particle as a direct function of the positions of its neighboring particles:

$$V_i = \frac{1}{\sum_j W_{ij}} \tag{2.45}$$

and its density as:

$$\rho_i(t) = \frac{m_i}{V_i} = m_i \sum_j W_{ij} \tag{2.46}$$

This definition of the particle volumes was introduced by Español and Revenga [27] within an SPH-DPD (Disspative Particle Dynamics) scheme. As highlighted in their paper, the volume V_i defined as (2.45) does not coincide with the geometrical volume occupied by the particle, as the sum of these volumes does not necessarily coincide with the total volume of the fluid domain V_T, i.e.:

$$\sum_i V_i \neq V_T \tag{2.47}$$

For this reason in [27] the quantity V_i is called "thermodynamic volume", in the sense that it is directly linked to W_{ij} which also determines the inter-particle forces in the momentum equation. This error in Eq. (2.47) decreases when increasing the ratio $R_k/\Delta x$ if the kernel function is not truncated.

In the present context of multiphase flows with free-surface, we circumvent the kernel truncation issue discussed in Section 2.1.3 by writing the time derivative of (2.45) as follows:

$$\frac{dV_i}{dt} = -\frac{\sum_j \frac{dW_{ij}}{dt}}{(\sum_j W_{ij})^2}, \quad \frac{dW_{ij}}{dt} = \frac{dW(\mathbf{x}_i(t) - \mathbf{x}_j(t), R_k)}{dt} = -(\mathbf{u}_j - \mathbf{u}_i) \cdot \nabla_i W_{ij} \tag{2.48}$$

which yields the following expression of the volume time derivative:

$$\frac{dV_i}{dt} = V_i^2 \sum_j (\mathbf{u}_j - \mathbf{u}_i) \cdot \nabla_i W_{ij} \tag{2.49}$$

In order to integrate Eq. (2.49) in time, the initial particle volumes V_{i0} should be defined. These are known from the particles positions inside the fluid at the initial time. Usually at $t = 0$ the particles are regularly positioned in the domain. Therefore, at least at the initial instant, the "thermodynamic"

volumes coincide with the geometrical ones, and can be initialized as such. One can also use the particle packing technique described in [20], in which case the volumes can be initialized by the obtained tessellation.

Next, we need to derive a momentum equation which is formally compatible with the volume equation (2.49) (see Section 1.3.2). To this aim, the continuum Lagrangian [26] L of the system is discretized for a generic set of SPH particles as:

$$L = \sum_j m_j \frac{u_j^2}{2} - m_j U(t, \mathbf{x}_j) - m_j e(\rho_j) \tag{2.50}$$

where U is a generic potential energy per unit of mass whose gradient yields a force field $\mathbf{f}$, such as gravity in our case, *i.e.* $\mathbf{f} = -\partial U / \partial \mathbf{x}$, and e is the internal energy per unit of mass. e is supposed to be a function of the density field only. Indeed, in the scope of the present work, we suppose that the entropy is constant since we are not concerned with the irreversible thermodynamic exchanges between particles. Further details on these aspects are presented in Colagrossi et al. [19].

The dynamics of a particle i is described by Lagrange's system of equations:

$$\frac{d}{dt}\left(\frac{\partial L}{\partial \mathbf{u}_i}\right) - \frac{\partial L}{\partial \mathbf{x}_i} = 0 \tag{2.51}$$

where $\partial./\partial.$ denotes the partial derivative. The second term of (2.51) is written as:

$$\frac{\partial L}{\partial \mathbf{x}_i} = m_i \mathbf{f}_i - \sum_j m_j \left(\frac{de(\rho_j)}{d\rho_j}\right) \frac{\partial \rho_j}{\partial \mathbf{x}_i} \tag{2.52}$$

in which, following the first law of thermodynamics, the pressure P_j is equal to the variation of the internal energy e_j as a consequence of the variation of the density field ρ_j:

$$P_j = \rho_j^2 \frac{de_j}{d\rho_j} \tag{2.53}$$

which means that the term $\dfrac{de_j}{d\rho_j}$ can be replaced by $\dfrac{P_j}{\rho_j^2}$.

Next, we write the time derivative of the density equation (2.46):

$$\frac{d\rho_j}{dt} = m_j \sum_k \left(\frac{d\mathbf{x}_j}{dt} - \frac{d\mathbf{x}_k}{dt}\right) \nabla_j W_{jk} \tag{2.54}$$

which yields the following expression of the Lagrangian increment of density:

$$\delta\rho_j = m_j \sum_k (\delta\mathbf{x}_j - \delta\mathbf{x}_k) \nabla_j W_{jk} \tag{2.55}$$

From the last equation we finally obtain:

$$\frac{\partial \rho_j}{\partial \mathbf{x}_i} = m_j \sum_k (\delta_{ji} - \delta_{ki}) \nabla_j W_{jk} \tag{2.56}$$

where δ_{ji} is the Kronecker delta function.

Substituting (2.56) in (2.52) and (2.52) in (2.51), and after rearranging the summation indices, we obtain the following momentum equation:

$$m_i \frac{d\mathbf{u}_i}{dt} = m_i \mathbf{f}_i - \sum_j (P_i V_i^2 + P_j V_j^2) \nabla_i W_{ij} \tag{2.57}$$

Similarly to Grenier et al. [35], the density can finally be computed via a Shepard interpolation as Eq. (2.28) instead of Eq. 2.46 in order to keep a sharp density jump at the interface between different fluids. Moreover, the idea of adding the diffusive δ-term to the volume equation is maintained for this scheme, in order to improve the quality of the pressure field.

To sum up, the complete set of governing equations of the proposed alternative multiphase SPH formulation, written for the generic i^{th} particle of a generic phase χ, reads:

$$\begin{cases} \dfrac{d\mathbf{x}_i}{dt} = \mathbf{u}_i & (2.58) \\ \dfrac{dV_i}{dt} = V_i^2 \displaystyle\sum_j (\mathbf{u}_j - \mathbf{u}_i) \cdot \nabla_i W_{ij} + \delta h c_{0\chi} V_i \sum_{j \in \chi} \psi_i^{VSR} \cdot \nabla_i W_{ij} & (2.59) \\ m_i \dfrac{d\mathbf{u}_i}{dt} = -\displaystyle\sum_j (P_i V_i^2 + P_j V_j^2) \nabla_i W_{ij} + m_i \mathbf{f}_i \\ \qquad\qquad + \alpha h c_{0\chi} \rho_{0\chi} \displaystyle\sum_{j \in \chi} \pi_{ij} \frac{V_i^2 + V_j^2}{2} \nabla_i W_{ij} & (2.60) \\ \rho_i = \displaystyle\sum_{j \in \chi} m_j W_{ij}^S & (2.61) \\ P_i = f_\chi(\rho_i) & (2.62) \end{cases}$$

Comparing this alternative set of governing equations (2.58)–(2.62) with the Multiphase δ-SPH scheme (2.36)–(2.40), some minor differences arise in terms of the particle volumes averaging inside the equations of volume and momentum. However, in the weakly-compressible context of this work, the variations of particle volumes within the kernel support are always very limited. It follows that the differences in using the two different schemes are in practice always negligible, and are reduced when increasing the spatial resolution. This practical equivalence of the two formulations will be displayed in Chapter 3 (see Section 3.3.3).

2.4 Numerical stability of the Multiphase δ-SPH scheme

2.4.1 Choice of sound speeds

A fourth-order explicit Runge-Kutta scheme is used to march in time the system of equations (2.36)–(2.40). As described in [1], in order to reduce CPU costs and improve the stability of the scheme, the diffusive δ-term is updated outside the sub-time steps of the Runge-Kutta scheme while it is "frozen" inside.

The time step of the simulations is set as:

$$\Delta t = \min_i(\Delta t_i^c), \quad \Delta t_i^c = K\frac{R_k}{c_{0\chi}} \quad \forall i \in \chi \tag{2.63}$$

where Δt_i^c is the limit time step due to the acoustic constraint and K is the CFL factor. The time step Δt_i^c then depends on the specific speed of sound $c_{0\chi}$ of each phase χ. The K factor is set smaller than the maximum value K_{max} which depends on the specific time scheme and the chosen kernel function, and can also be problem dependent. For the simulations presented in Chapter 3, K was set heuristically to 0.75, as with this value the scheme was found to always be stable even for violent flow conditions.

As already stated before, this work focuses on interfacial flows in the presence of a free-surface, more specifically, problems where a liquid X interacts with entrapped gas pockets Y and a free-surface FS. The gas Y, in some conditions, can be compressed by the liquid phase, for example in the water entry problem of Section 3.4), or in gas pockets formed after wave breaking. For this reason, the compressibility of the gas matters. Since it is linked to the speed of sound c_{0Y}, the latter cannot be chosen freely for computational convenience, but has to be equal to the real physical one.

In general, for cases where compressibility effects are important for the gas dynamics, the Euler non-dimensional number should be preserved in the simulation. It is defined as:

$$\mathrm{Eu} = \frac{P_{0Y}}{\rho_X U_X^2}, \quad P_{0Y} = \frac{\rho_{0Y} c_{0Y}^2}{\gamma_Y} \tag{2.64}$$

where p_{0Y} is the pressure of the entrapped gas pocket in rest condition and U_X is the speed of liquid acting against the gas pocket.

Conversely, the liquid phase X is treated as a weakly-compressible medium (see Section 1.3.1), *i.e.* for computational convenience the speed of sound can be reduced with respect to the real one up to the limit:

$$c_{0X} \geq 10 \max\left(U_{max}, \sqrt{\frac{\Delta P_{max}}{\rho_{0X}}}\right) \tag{2.65}$$

where U_{max} and ΔP_{max} are the maximum expected velocity and pressure variation in phase X. The condition (2.65) guarantees the weakly-compressible regime, that is, the fluid density variations for X shall remain smaller than 1% (see *e.g.* [65]). This allows the adoption of a lower value of the sound speed with respect to the actual value which would lead to very small time steps and therefore, high computational costs.

The above conditions where the value of c_{0Y} is equal to the physical one and c_{0X} is set to guarantee the weakly-compressible approach, can lead to counter-intuitive situations in which the air phase is modeled using an air sound speed larger than the liquid one. However, as explained in [18] and [34] and shown in Section 3.4, the above choice remains a good approximation provided that the constraint (2.65) is respected.

In Colagrossi and Landrini (2003) [18] a further constraint, this time on the ratio between the speeds of sound c_{0X} and c_{0Y}, is included and reads as:

$$P_{0Y} = P_{0X} \Rightarrow \frac{c_{0X}}{c_{0Y}} = \sqrt{\frac{\gamma_X \rho_{0X}}{\gamma_Y \rho_{0Y}}} \tag{2.66}$$

The nature of this constraint was not justified by [18]. The present study will show that it is linked to a stability constraint of the scheme and can be rewritten in a more complete fashion.

Through the simple test cases discussed in Section 2.4.2, heuristically we found that the relation (2.66) allows for stable simulations when the CFL coefficient is set equal to $K = 1.13$. Conversely, by varying the K factor we found further regions of stability which can be generally indicated as:

$$K < f\left(\frac{c_{0X}}{c_{0Y}}, \eta\right), \quad \eta = \sqrt{\frac{\gamma_X \rho_{0Y}}{\gamma_Y \rho_{0X}}} < 1 \tag{2.67}$$

where f is a monotonically non-increasing function of the variables (c_{0X}/c_{0Y}) and η.

2.4.2 Stability regions through the Bagnold problem

In order to derive the regions of stability given by Eq. (2.67), a 1-D Bagnold problem [4] has been considered. In particular, the same configuration adopted in [38] has been used for the test case: a liquid fluid patch is confined between two gas pockets under gravity forcing. In the initial condition the velocity is zero everywhere (see sketch in Fig. 2.1).

As in [38], the total length of the tank is $H = 15m$. For all the simulations the following parameters have been used: $H/\Delta x = 240$, $R_k/\Delta x = 4$, for the liquid $\gamma_X = 7$, and for the gas $\gamma_Y = 1.4$, while $\delta = 0.1$, $\alpha = 0.07$, $\epsilon_\chi = 0.02$ for both phases. This simple test case is used to study the conditions in which the scheme stays stable. Several combinations of density ratios and speeds of sound have been tested.

In Fig. 2.2 the stability region is studied in the plane $(c_{0Y}/c_{0X}, K)$. Three different ratios $\rho_{0X}/\rho_{0Y} = 10, 100, 1000$ have been considered which corresponds to three η values of $0.71, 0.22, 0.071$ (see Eq. (2.67) and considering

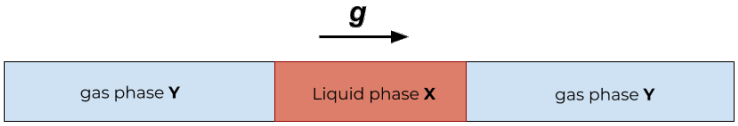

FIGURE 2.1: 1D two-phase Bagnold test: a patch of fluid **X** is confined by two gas pockets **Y**. At $t = 0$ the fluid velocity is zero and the fluid is subjected to gravity.

the ratio of the polytropic coefficients fixed to the value $\gamma_X/\gamma_Y = 5$). For this simple case the maximum CFL value reached is $K_{max} = 1.4$ which is much higher than the 0.75 value used in the SPH simulations discussed in Chapter 3.

It is worth noting that in this 1-D test case particles advection is very small which is not the case for the other SPH simulations presented in the paper. The bullet dots in Fig. 2.2 represent the maximum K value to obtain a stable SPH simulation for a given couple $(c_{0Y}/c_{0X}, \eta)$. The unstable simulations, not shown here for the sake of brevity, appear as being affected by numerical high frequency pressure oscillations inside the two gas cavities with increasing amplitude in time.

Using a set of forty-five simulations performed, the stability limits have been simplified using just two lines for each considered value of η, where the inclined lines present all the same steepness. A rule for the stability can be established with the equation:

$$K < \max\left\{\left[K^* - \kappa \log\left(\frac{c_{0X}}{c_{0Y}}\frac{1}{\eta}\right)\right], K^*\eta\right\}, \qquad \eta = \sqrt{\frac{\gamma_X \rho_{0Y}}{\gamma_Y \rho_{0X}}} < 1 \tag{2.68}$$

where $K^* = 1.13$. The steepness coefficient κ, as mentioned before, does not depend on η while it could be dependent on the dissipation of the scheme, *i.e.* in our case on the parameters δ and α.

In most of the simulations performed in this article the ratio c_{0X}/c_{0Y} is always less than one, since we consider the **X** phase as a liquid and **Y** phase as a gas. As explained above, in such a condition, where c_{0Y} is higher than c_{0X}, it follows that the first condition of Eq. (2.68) dominates. The optimal condition $c_{0X}/c_{0Y} = \eta$, which allows to use $K = K^*$, may not be adopted since the condition $c_{0X} = \eta\, c_{0Y}$ may not satisfy the weakly-compressible criterion (2.65). Therefore, in such a situation it is necessary to reduce the K parameter through Eq. (2.68) to adopt the right speeds of sound. As a consequence higher CPU costs are sometimes required.

On a theoretical note, Violeau and Leroy [101] performed a stability analysis of the weakly-compressible SPH equations using the von Neumann approach for single-phase unbounded flows. They obtained a theoretical stability criterion for the time step, depending on the kernel standard deviation, the speed of sound and the viscosity. Consequently, the constraints studied in this section deserve further investigation in order to theoretically understand the reasons behind the shapes and limits of the obtained stability regions, this

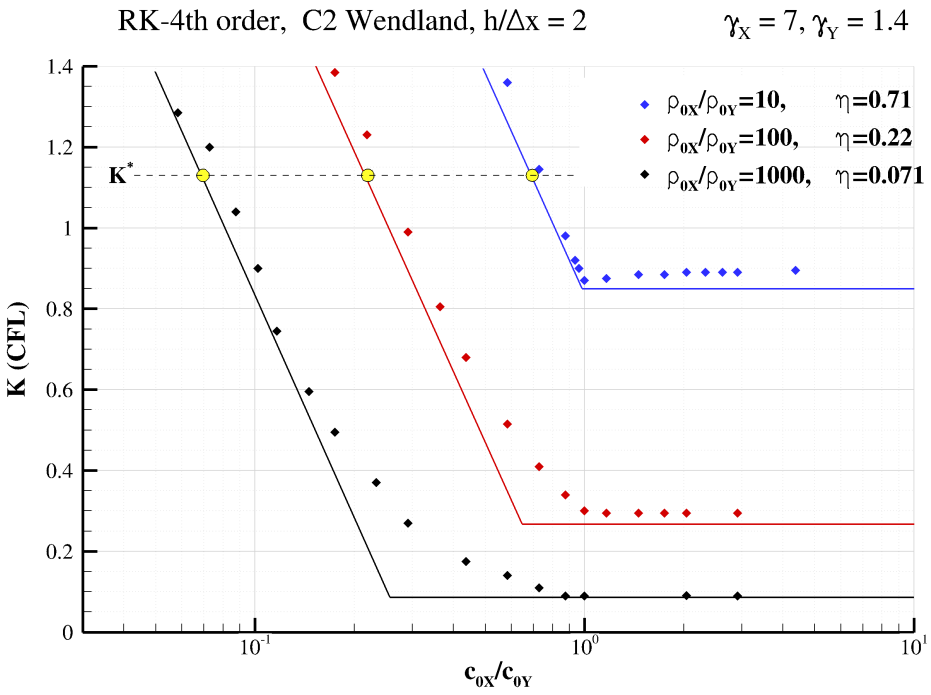

FIGURE 2.2: 1D two-phase Bagnold test: regions of stability. Each bullet represents the maximum CFL number reached for a given density ratio ρ_{0X}/ρ_{0Y} and speed of sound ratio c_{0X}/c_{0Y}, **X** and **Y** being the heavier and lighter phases, respectively. The solid lines represent the regression lines delimiting the stability region for each η value, η being the parameter defined in formula (2.66). The yellow bullets in the graph represent the points where $c_{0X}/c_{0Y} = \eta$ and $K = K^*$.

time in a multiphase context, and to derive possible solutions to go beyond these boundaries.

Chapter 3

Validation of the proposed model

The proposed model was validated through three classic test cases: a hydrostatic problem, an oscillating elliptic fluid patch and a dam-break. These simulations have the advantages of being easy to implement and widely used within the SPH literature, with well-known experimental data and/or analytical solutions. In order to highlight the capabilities of the model, each simulation was run in single-phase and multiphase configurations.

As a final test case, a more challenging problem is addressed: the water impact of a corrugated panel with an entrapped air cavity. This problem also presents complex free-surface dynamics and, therefore, is a good candidate for showing how the proposed SPH method is able to treat this kind of water impact flows.

3.1 Long-time evolution for the hydrostatic test-case

In this section the evolution of a tank partially filled with water at rest with a hydrostatic pressure distribution is simulated. This simple test case was chosen in order to test the ability of the model of maintaining a stable free-surface in both single and two-phase configurations. Indeed, new SPH formulations can induce non-physical particle re-settlement due to lack of consistency of the scheme in the presence of boundaries and volume forces. For instance in [1] it was shown that the use of diffusive terms in the continuity equation can induce instabilities at the free-surface if the latter is not properly taken into account.

In the present study, for the single-phase configuration a two-dimensional tank is half-filled with water at rest. For the air-water simulation, the other half is filled with air, and the density ratio is 1000. The filling height is H and a downward gravity acceleration $\mathbf{g}$ is present. The computed single-phase and two-phase solutions are shown in Fig. 3.1 at $t\sqrt{g/H} = 62.64$.

Similarly to [1], in both solutions the free-surface is stable and the hydrostatic solution is well respected. However, in the two-phase configuration a non-physical separation appeared at the interface region between air and water. This problem was reported in [51], and a correction was proposed based on a buoyancy model via the addition of a numerical term to the momentum equation. Here, we simply add a background pressure $P_b = 0.1\,\rho_{0w} g H$ where ρ_{0w} is the nominal density of water, which solves this issue, since we found

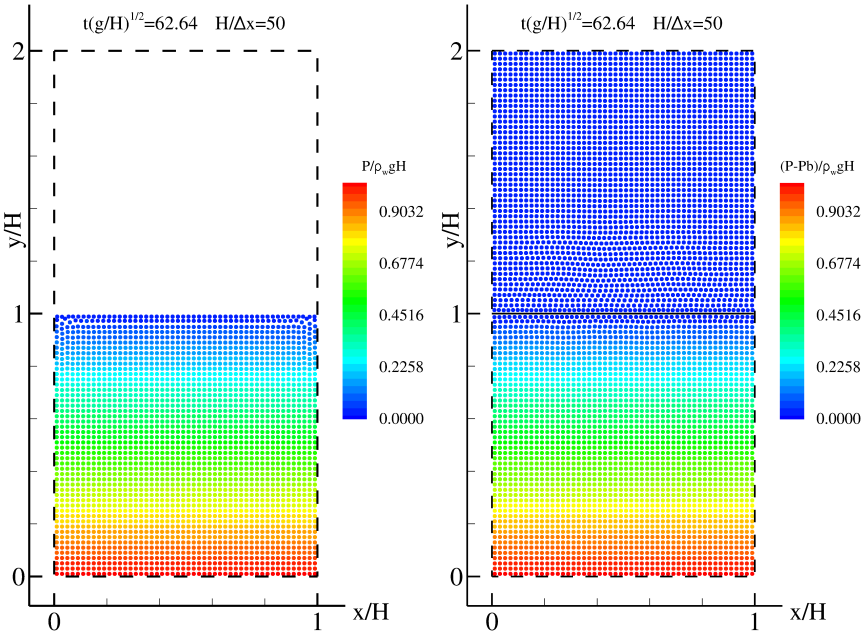

FIGURE 3.1: Hydrostatic solution: particle configuration and pressure distribution in single-phase (left) and two-phase (right), at $t\sqrt{g/H} = 62.64$.

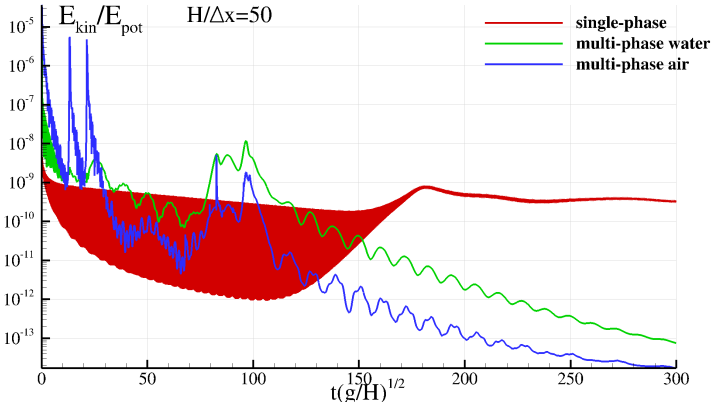

FIGURE 3.2: Hydrostatic solution: evolution of the kinetic energy for the single-phase and air-water configurations. The kinetic energy of each phase is made dimensionless using its initial potential energy.

that the interface separation is strongly linked to the appearance of negative pressure in the interface zone during the first time steps. The particles generally stay on the initial Cartesian grid, although a small perturbation is observed just underneath the free-surface and around the air-water interface.

Fig. 3.2 shows the normalized kinetic energy evolution up to $t\sqrt{g/H} = 300$. At the beginning of the simulation a small amount of potential energy is converted to kinetic energy due to the relaxation of the particle Cartesian lattice (see, e.g., [20]). Then the kinetic energy rapidly decreases towards zero for both single and two-phase simulations, showcasing the good stability and robustness of the model. The kinetic energy of the air-water simulation is initially higher and decays faster than its single-phase counterpart. This is due on the one hand to the already mentioned fact that particles move a bit more close to the interface in the multiphase simulation, and on the other hand to the addition of the background pressure in the multiphase case, which induces a higher level of numerical dissipation.

3.2 Oscillating drop: single/two-phase simulations

In the present section a 2D fluid patch evolving in a quadratic potential field $\Phi(x, y) = 1/2\Omega^2(x^2 + y^2)$ is considered, where Ω is a parameter that controls the oscillations of the fluid patch. The fluid is inviscid and the radius of the disk is R. The velocity field is assumed to have the following form:

$$\begin{cases} u = \quad A(t)x \\ v = -A(t)y \end{cases} \tag{3.1}$$

where the initial condition $A(t = 0)$ is set equal to the parameter A_0. The ratio Ω/A_0 is set equal to 1. Following the study by Monaghan and Rafiee [75], under these conditions the free surface evolves periodically with an elliptical shape. In the present work the objective of this test-case is to validate the proposed SPH scheme by monitoring the evolution of the mechanical energy, and by comparing our solutions of both the single and two-phase oscillating drops with their analytical counterparts.

3.2.1 Single-phase case

Fig. 3.3 presents the initial and deformed shapes of the fluid patch at three different time instants. The obtained free-surface configurations are compared with the analytical solution provided in [75], resulting in a very good agreement. This is further illustrated in the top plot of Fig. 3.4, where the predicted evolution of the ellipse semi-axis $a(t)$ is plotted against the analytical solution for 8 periods of oscillation.

A convergence study was made in order to evaluate the energy conservation properties of the scheme. The bottom plot of Fig. 3.4 shows the evolution of the normalized mechanical energy for three increasing discretization ratios

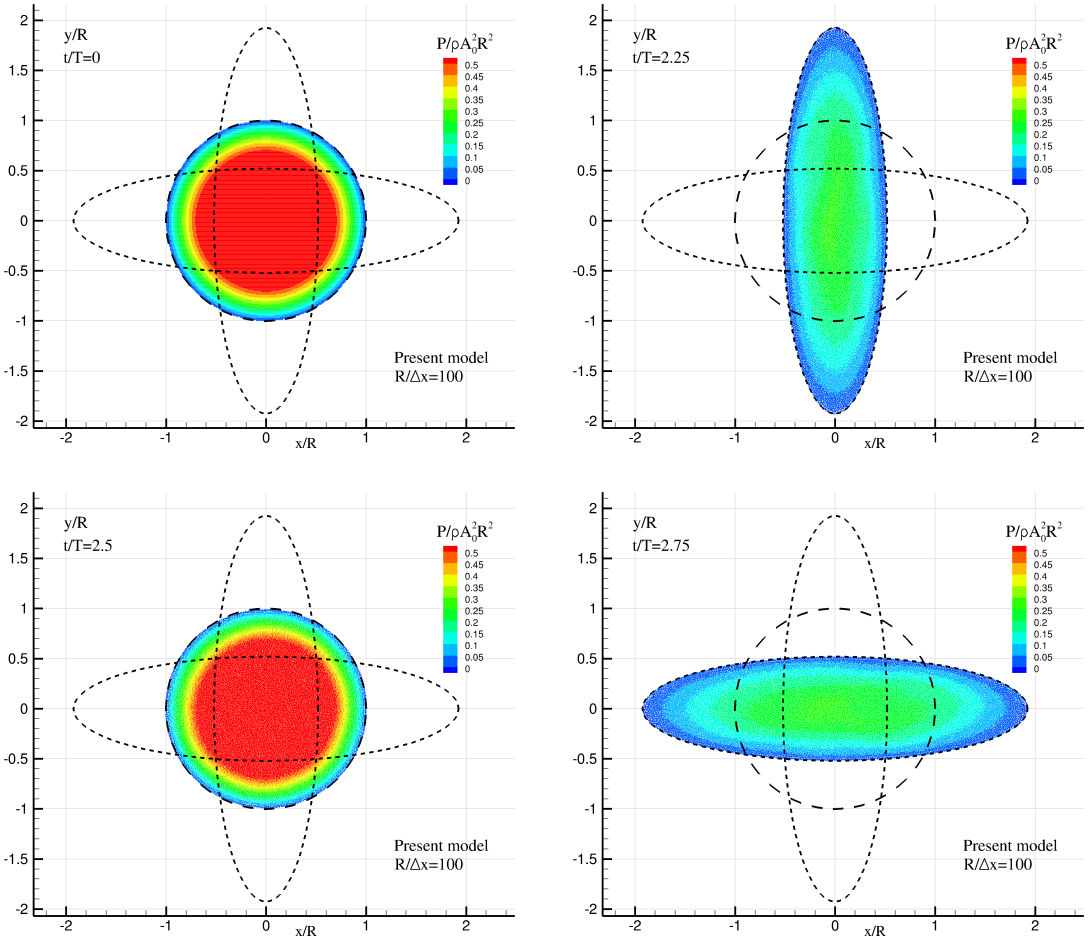

FIGURE 3.3: Single-phase oscillating drop: snapshots of the evolution at different times. The dashed line represents the analytical solution.

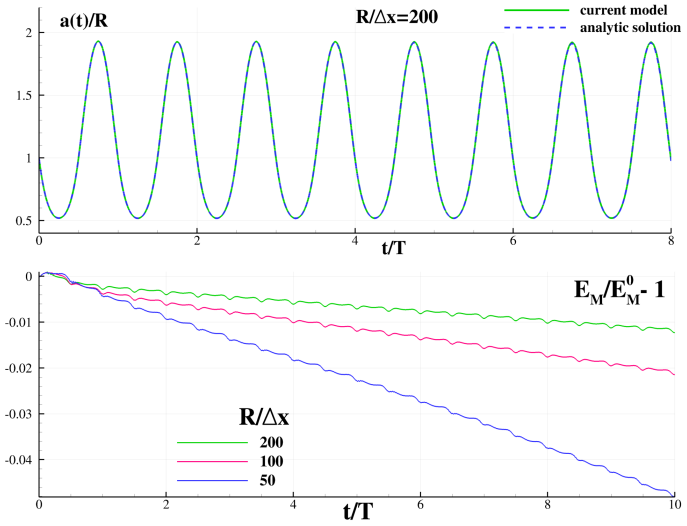

FIGURE 3.4: Single-phase oscillating drop: at the top, comparison between the predicted evolution of the semi-axis $a(t)$ and the analytical solution. At the bottom, time history of the normalized mechanical energy variation for different discretizations.

$R_k/\Delta x = 50, 100, 200$. Similarly to Antuono et al. [2], for increasing numbers of particles, smaller dissipations of the mechanical energy occur due to the presence of the δ-term in the continuity equation, as its contribution goes to zero when the inter-particle distance goes to zero. For the finest resolution the dissipated energy after 10 oscillation periods is about 1% with respect to the initial one.

The present test-case is also used to study the influence of the integrals Γ in the Grenier et al. [34] model which have been removed in the present scheme (see Section 2.1.6). Figure 3.5 shows the time history of the pressure recorded at the center of the oscillating bubble evaluated with and without taking into account the integral Γ, see Eq. (2.31). The two solutions remain quite close, although the scheme without the Γ factors seems to remove the acoustic pressure oscillations in a more effective way.

In the top plot of Fig. 3.5 a pressure oscillation is observed for both solutions around $t = 0.2T$. This is due to the destruction of the particles tessellation which originates from the initial Cartesian distribution. This leads to a numerical pressure wave which is damped later in time. This phenomenon was reported in [20], where a particle packing algorithm was used to circumvent this issue. Also, in our computations we found that initializing the particles according to a polar distribution helps relieving this issue, as shown in the bottom plot of Fig. 3.5. Besides, the initial particle configuration does not affect the solution later in its evolution.

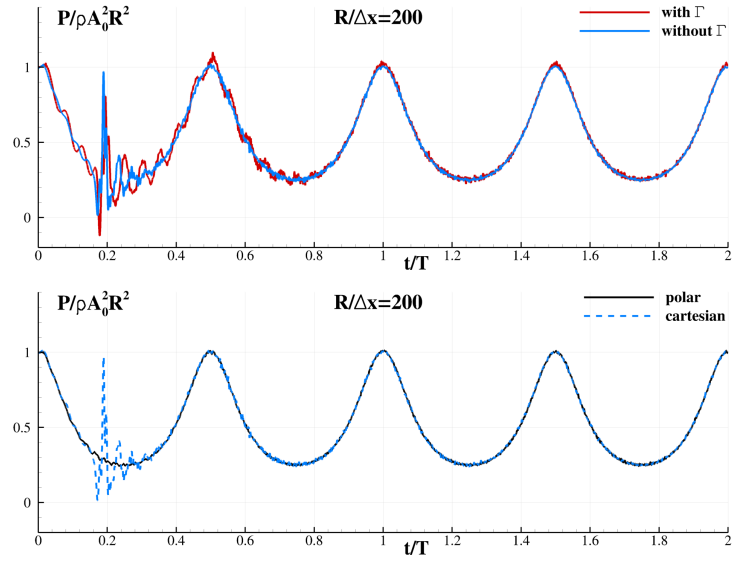

FIGURE 3.5: Single-phase oscillating drop: time history of the pressure at the bubble center $r = 0$. Top: computed with and without taking into account the integral Γ. Bottom: computed with initial polar/Cartesian particle distributions.

3.2.2 Multiphase case

Here we consider two initial concentric circular patches of fluid. The heavier fluid occupies the inner circular region of radius $R/2$, while the lighter fluid occupies the region between the outer circle of radius R and the inner circle. After initializing both fluids according to the quadratic potential $\Phi(x, y) = 1/2\Omega^2(x^2 + y^2)$, we compute their evolution with the proposed SPH model. Once again we keep the ratio $\Omega/A_0 = 1$. The heavier fluid needs to be in the inner region, because if the phases are swapped the flow will become unstable under the action of the potential Φ and a Rayleigh-Taylor instability will take place.

This second benchmark is particularly interesting for the validation of the present model since the multiphase domain is confined by a free surface. In the initial condition the pressure is correctly initialized, and unlike [75], no damping technique is needed to initialize the simulation. Fig. 3.6 illustrates the initial configuration of the problem, with a density ratio $\rho_{inner}/\rho_{outer} = 1000$.

Fig. 3.7 shows the evolution of the outer ellipse semi-axis $a(t)$ for two different density ratios, $\rho_{inner}/\rho_{outer} = 10$ and 1000. As predicted by the analytical solution, the time evolution of the outer axis, $a(t)$, is not affected by the density ratio $\rho_{inner}/\rho_{outer}$. This is not the case for the pressure at the center of the inner fluid which is plotted in Fig. 3.8.

Once again, a small perturbation at the end of the first quarter-period occurs due to the initial Cartesian distribution of the particles. Apart from that, the pressure predicted by the current model follows closely the analytic incompressible solution for both density ratios.

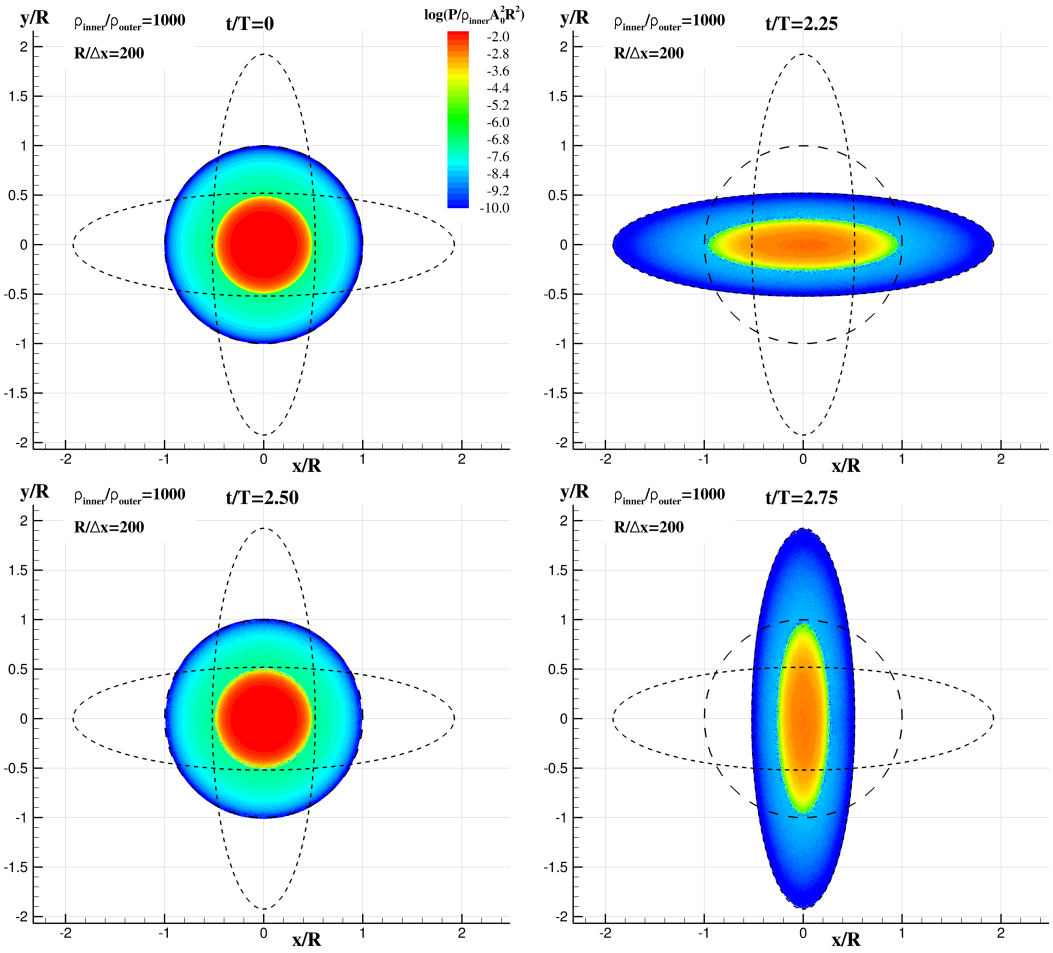

FIGURE 3.6: Two-phase oscillating drops: evolution of the pressure field for the concentric circular bubbles problem at different times. The dashed line represents the analytical solution

.

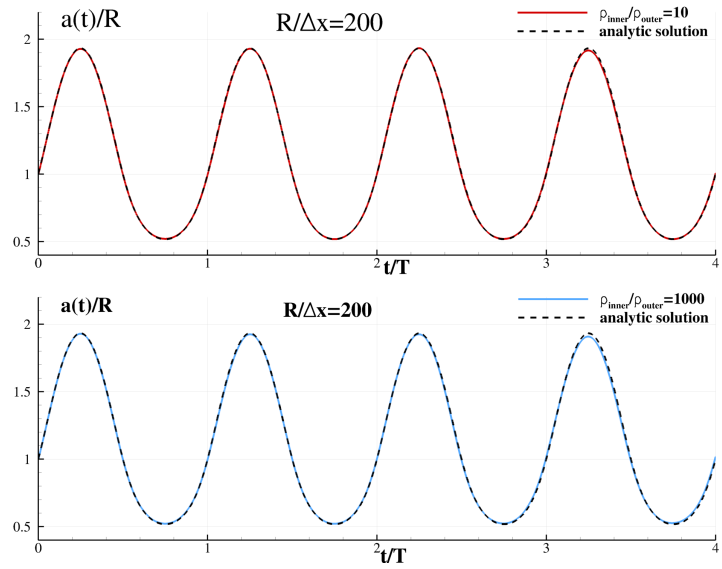

FIGURE 3.7: Two-phase oscillating drops: time evolution of the the outer ellipse semi-axis for a density ratio of 10 (top) and 1000 (bottom). The solution obtained by the proposed Multi-phase δ-SPH scheme is compared with the analytic incompressible flow solution. The axis time evolution $a(t)$ is hardly affected by the density ratio.

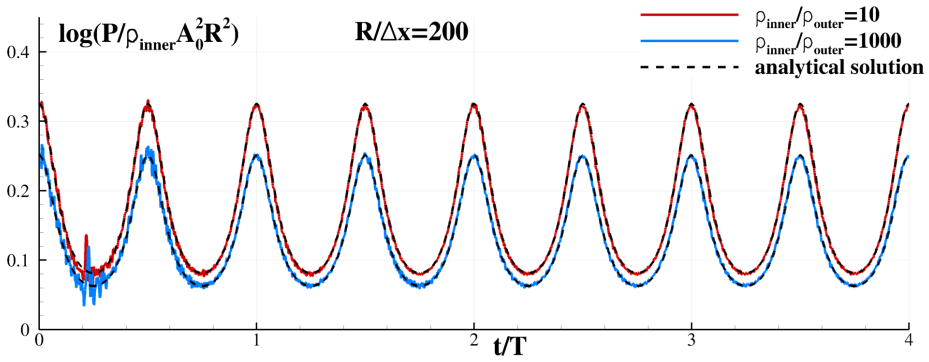

FIGURE 3.8: Two-phase oscillating drops: evolution of the pressure at the center of the inner bubble for the density ratios 10 and 1000.

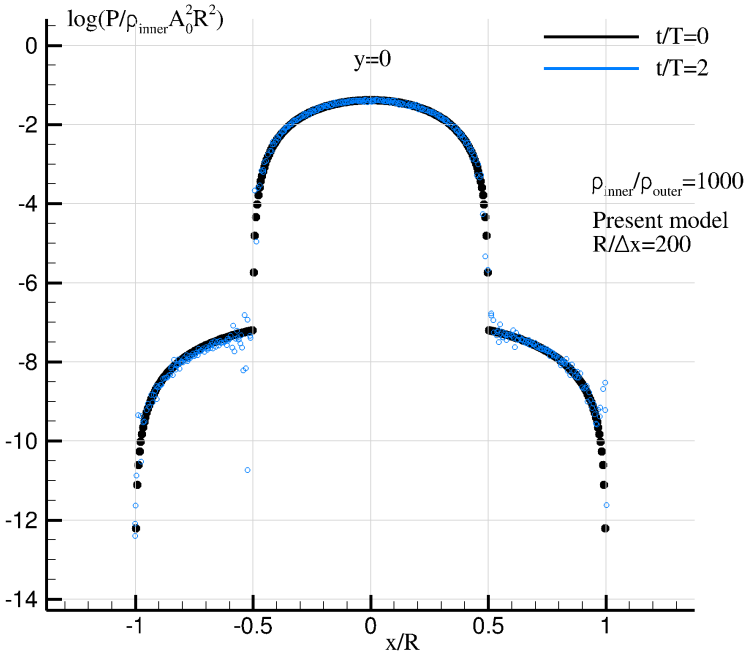

FIGURE 3.9: Two-phase oscillating drops: pressure in the inner and outer phases along the horizontal line y = 0, at the initial time and after 2 periods.

Fig. 3.9 shows the pressure in the inner and outer phases along the horizontal line $y = 0$ at the initial time and after 2 periods for the density ratio $\rho_{inner}/\rho_{outer} = 1000$. The pressure after 2 periods matches quite accurately the initial distribution as expected. At the interfaces, some particles, especially those from the lighter phase, deviate from the expected value. Aside from these drawbacks in the local solution, the proposed model reproduces the analytical incompressible kinematics with a satisfactory accuracy and yields smooth pressure fields in both the lighter and outer phases (see also Fig. 3.6).

3.3 Dam-break flow: single-phase and air-water configurations

The third test case is a dam-break flow impacting a vertical wall. It is one of the most popular test cases in the SPH community, due to the existence of experimental results [66, 95, 8] for different setups (tank geometry, water length and height, dry/wet bed etc.). Moreover, it is a challenging test case because of the free-surface fragmentation and the viscous dissipation due to the multiple breaking processes of the water splash-ups [65].

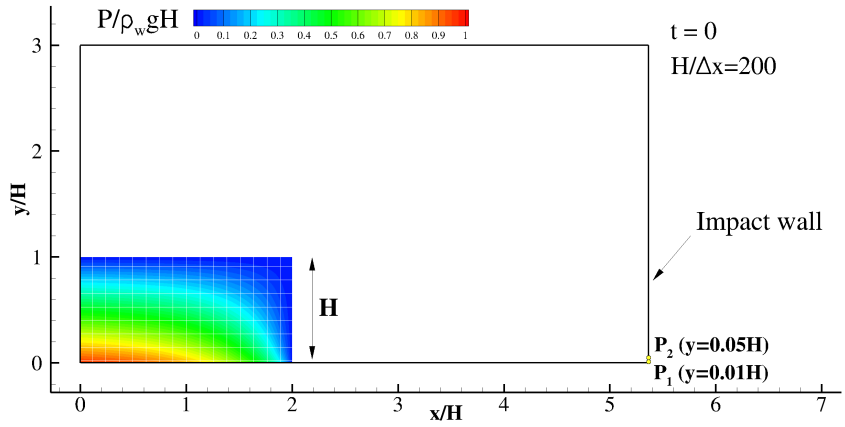

FIGURE 3.10: Single-phase dam-break: initial configuration.

In the present study, the dam-break configuration follows the experiments made by Lobovský et al. [58], where different impact pressure measurements on the vertical wall are provided. The probes locations in our simulations were chosen in accordance with the ones from their experiments.

3.3.1 Single-phase simulation

The initial single-phase configuration is illustrated in Fig. 3.10. The discretization ratio is $H/\Delta x = 200$. Snapshots of the dam-break flow evolution in the single-phase configuration are shown in Fig. 3.11.

The model clearly handles well the presence of the free-surface. Also, thanks to the addition of the diffusive terms in the present model, no spurious oscillations of pressure are observed. This is the main improvement upon [34] as illustrated in Fig. 3.12, which highlights the differences in the resulting pressure fields obtained with the proposed model and with the original Grenier et al. model [34], where local pressure oscillations occurred, also linked to bad particle arrangements.

3.3.2 Two-phase simulation

Another simulation of the same dam-break flow was run, this time in a multiphase configuration. The adopted density ratio is $\rho_{water}/\rho_{air} = 1000$. The background pressure value here is $P_b = 0.1\rho_{0water}gH$. Also, since the oscillations of the enclosed air cavity are of interest here, the sound speed of the air phase is taken equal to its physical value $c_{0air} = 343$ m/s. Fig. 3.13 shows the dam-break evolution and the pressure field in the water phase. The latter is in very good agreement with its single-phase counterpart (see Fig. 3.11), as the pressure levels inside the water are almost identical in both cases up to the cavity closure, after which the air cushioning effects become relevant (see third plot of Fig. 3.13) and the two flow evolutions do not behave in the same manner anymore.

This visual agreement is confirmed by monitoring the pressure signals at two probes P_1 and P_2. As observed in Fig. 3.14, both models are in very good

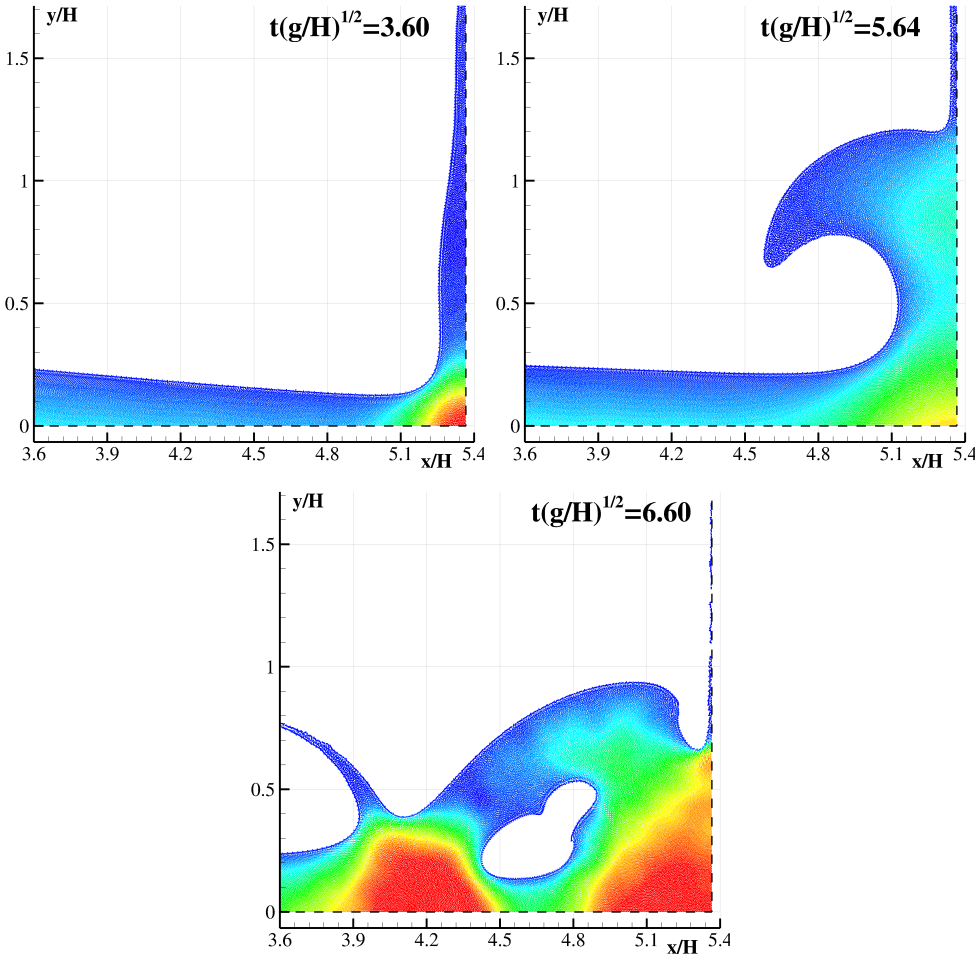

FIGURE 3.11: Single-phase dam-break: snapshots of the flow at different times. Colors are representative of the dimensionless pressure $p/(\rho_{water} g H)$ from 0 (blue) to 1 (red).

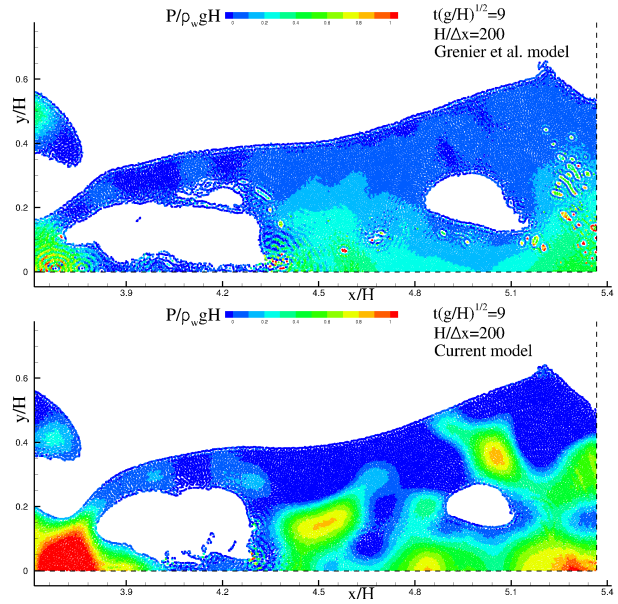

FIGURE 3.12: Single-phase dam-break: snapshot of the flow at $t(g/H)^{1/2} = 9$, using the original Grenier et al. model (top) and the proposed model (bottom).

agreement up to around $t(g/H)^{1/2} = 6$, which corresponds to the first cavity closure. Then the two-phase model predicts a pressure oscillation due to the air cushioning effect of the entrapped air bubble, similarly to what was reported in [18]. A different behavior is observed in the single-phase simulation, in which this cavity is void. In this case the cavity collapses in a flat impact around $t(g/H)^{1/2} = 8$, transforming some of the mechanical energy into internal energy, in the form of traveling acoustic waves (see also [60] for a detailed discussion about this phenomenon).

In Fig. 3.14 the pressure recordings from [58] are also reported. A satisfactory agreement between numerical output and experimental data is achieved for the first pressure peak for both probes whilst some discrepancies are observed further in time. These differences are to be ascribed to relevant 3D effects observed in [58]. In any case, the pressure signals obtained by the present scheme are very close to those recently obtained by Meringolo et al. [68] using a dynamic δ-SPH scheme.

3.3.3 On the equivalence between the two proposed multiphase SPH formulation

3.3.3.1 Effect of particle volumes averaging

The single-phase dam-break configuration was also run using the proposed alternative derivation of the multiphase SPH formulation presented in Section 2.3 and compared to the modified Grenier et al. formulation (2.36)–(2.40). Snapshots of the obtained dam-break flow using both formulations are presented in Fig. 3.15. The pressure fields obtained using both models are quasi-identical, illustrating in practice the negligible effect of the difference

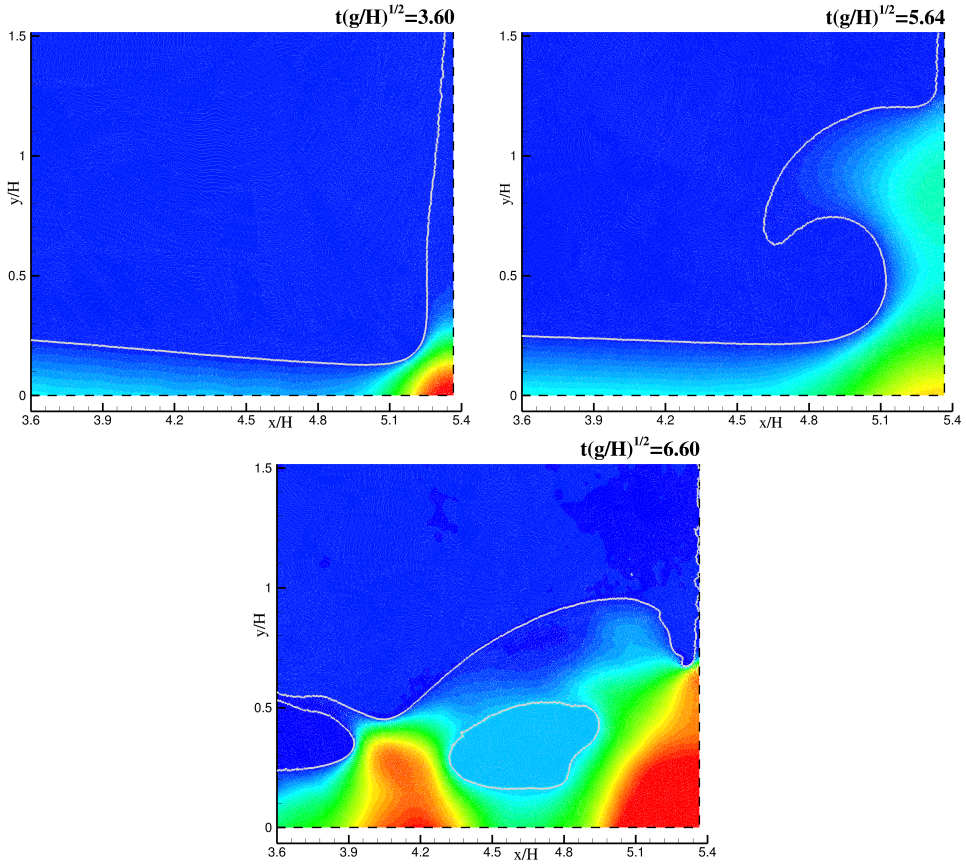

FIGURE 3.13: Two-phase dam-break: snapshots of the flow evolution at different times. Colors are representative of the dimensionless pressure $(P - P_b)/\rho g H$ from 0 (blue) to 1 (red) while the solid gray line is the air-water interface.

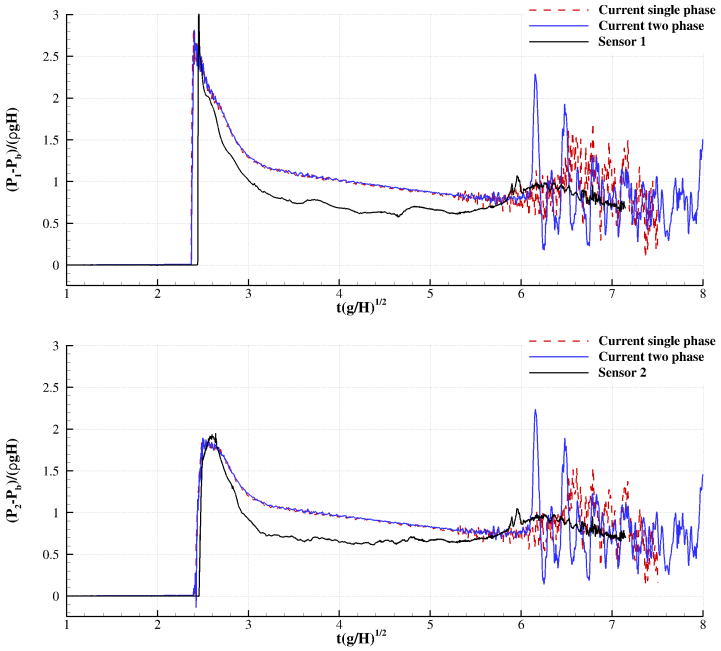

FIGURE 3.14: Single/two-phase dam-break: time history of the pressure signals at the probes P_1 and P_2. Comparison between the Multiphase δ-SPH and experimental results from Lobovský et al. [58].

in particle volume averaging between the two models within the weakly-compressible context (as analyzed at the end of Section 2.3).

3.3.3.2 Mass conservation

On the one hand, both formulations use a Shepard correction to compute the density (see, *e.g.*, (2.28)). On the other and, the volumes are obtained via their time evolution either through (2.37) or (2.45). This means that the quantity $\rho_i V_i$ is not necessarily equal to the initial mass of the particles m_i, which is supposed to stay constant (see Section 2.1.6). In the original Grenier al. paper [34], this is called a "relaxed link" between the particles masses, densities and volumes.

Nevertheless, throughout our computations it was found that the mass is indeed conserved despite the use of the Shepard correction. Keeping the current single-phase dam-break configuration as an example, the time evolution of the total "relaxed mass", defined as the product $\sum_i \rho_i V_i$, was monitored and compared to the initial total mass $\sum_i m_i$. Fig. 3.16 shows the results of a convergence study of the relaxed mass, which was carried out on both formulations. The discretization ratio $H/\Delta x$ is taken as 50, 100 and 200. A juxtaposition of the time evolution curves of the relaxed mass of both models is shown on Fig. 3.17.

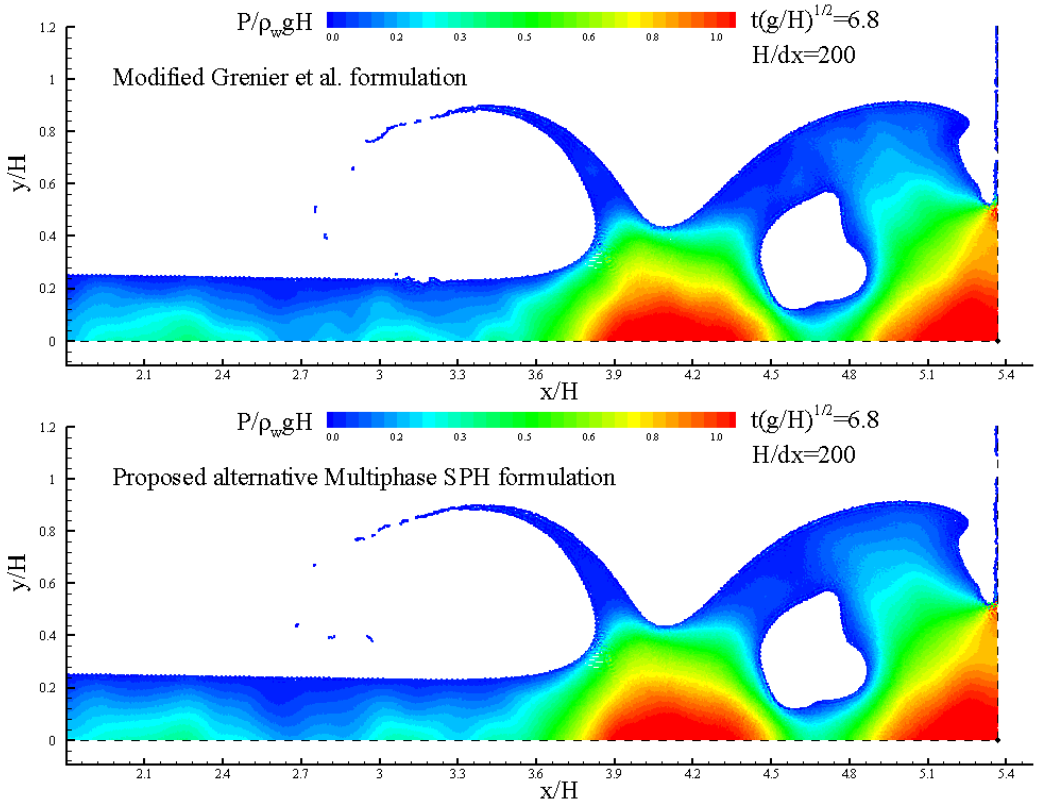

FIGURE 3.15: Single-phase dam-break: snapshots of the flow at $t(g/H)^{1/2} = 6.8$. Top: modified Grenier et al. model (2.36)–(2.40). Bottom: proposed alternative derivation of the SPH multiphase formulation (2.58)–(2.62). The obtained pressure fields are quasi-identical.

First, the convergence study shows for both models that even though the relation $m_i = V_i \rho_i$ is not strictly satisfied, the maximal error between the initial constant mass and the relaxed mass is less than 0.001%. Also, note that the highest peaks of mass variation occur after $t(g/H)^{1/2} = 6$, the time of the aforementioned cavity closure, after which the flow is quite chaotic and stronger dissipation will occur anyway. However, these small errors keep decreasing while increasing the particle resolution. Finally, Fig. 3.17 highlights once again the equivalence between the two proposed formulations, displaying practically the same time evolution of the relaxed mass, with small perturbations registered post-cavity closure.

3.4 Fluid impact of a corrugated panel with trapped gas cavity

In order to test the ability of the proposed model to correctly compute the pressure in challenging problems such as water impacts, the problem of the water entry of a corrugated panel on a liquid free-surface with a trapped gas cavity is considered.

Khabakhpasheva et al. (2012) [49] provided a semi-analytical solution for this problem derived from the Wagner theory. In that work they studied the initial stage of an incompressible liquid impact onto both rigid and elastic corrugated panels, accounting for a compressible gas pocket trapped between the corrugations, see the sketch in Fig. 3.18. The corrugation shape is described by the following function:

$$f(x) = h\left[1 - \cos^4\left(\frac{\pi x}{2\tilde{L}}\right)\right] \tag{3.2}$$

where h and $\tilde{L}$ are the corrugation's height and half-width respectively. This panel shape is noted in literature as Mark III panel which is a type of containment tank of Liquified Natural Gas (LNG) carriers (for more details see, *e.g.*, [61]).

The distance between the two corrugations is $2L$ (see Fig. 3.18) whereas the total panel length is $2c$. Similarly to [49] the following dimensions are adopted in all the simulations: $h = 3.6$ cm, $2\tilde{L} = 5.6$ cm and $2L = 34$ cm.

At the initial time $t = 0$, the corrugations touch the free-surface at two points $x = \pm L$ and the fluids are at rest. The gas cavity is bounded by the panel and the interface, and the panel penetrates the liquid surface with a forced purely vertical velocity U. In [49], the gas in the cavity is modeled adopting the polytropic state equation (1.4). In that work the pressure inside the cavity is assumed to be a function of the gas volume, which means that the pressure is considered uniform in the gas phase. The solution provided in [49] is general and valid for any density ratio between the liquid and the gas phase.

Since the focus is on high density ratios configurations, in the following test cases the considered fluids are air and water, respectively, with a density

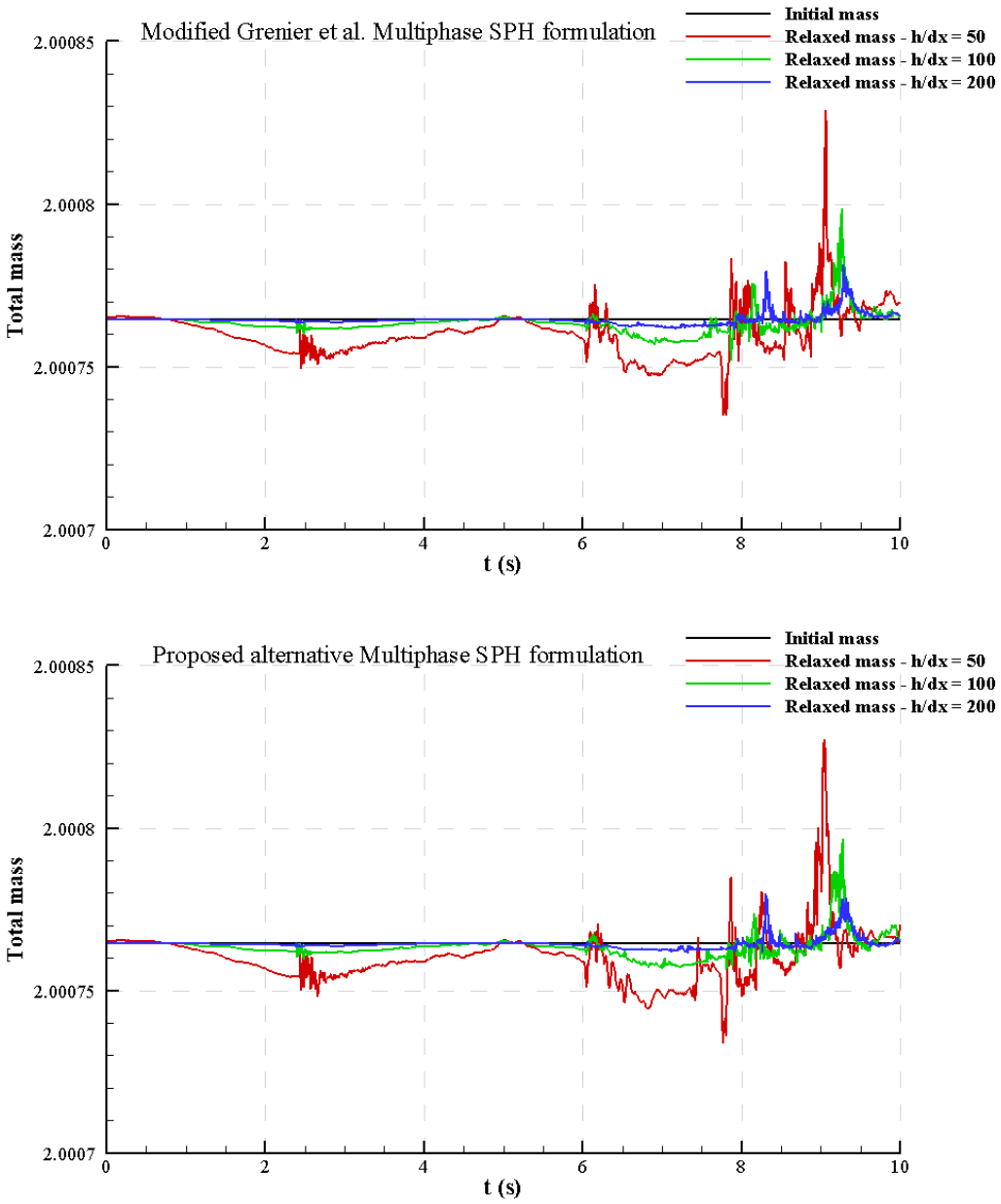

FIGURE 3.16: Single-phase dam-break: convergence study of the total relaxed mass $\sum_i \rho_i V_i$, using the modified Grenier et al. (2.36)–(2.40) scheme (top) and the proposed alternative derivation of the multiphase SPH formulation (2.58)–(2.62) (bottom), for increasing discretization ratios $H/\Delta x$ of 50, 100 and 200.

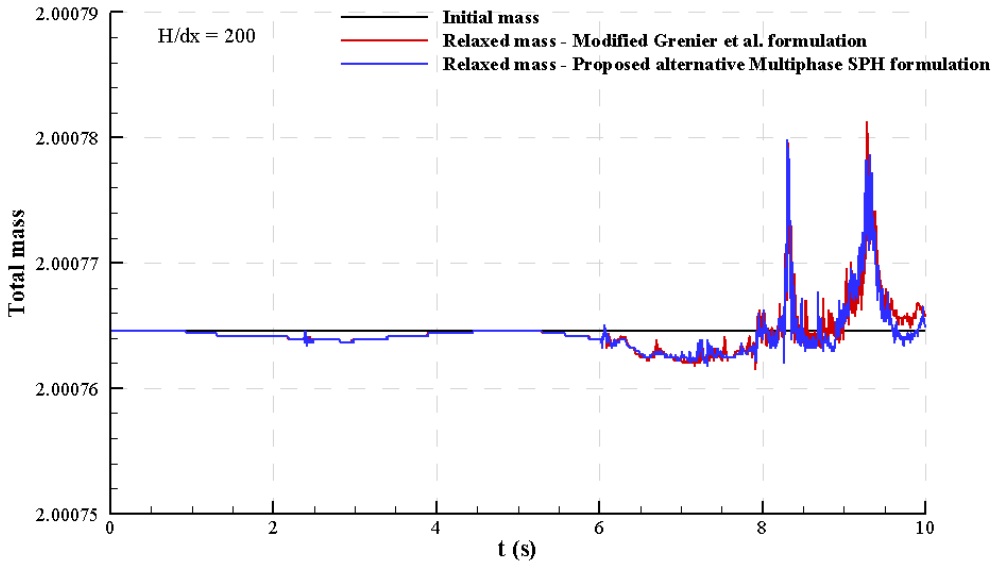

FIGURE 3.17: Single-phase dam-break: time evolution of the total relaxed mass $\sum_i \rho_i V_i$ with the initial constant mass $\sum_i m_i$, using the modified Grenier et al. (2.36)–(2.40) scheme and the proposed alternative derivation of the multiphase SPH formulation (2.58)–(2.62).

ratio of 1000, and the polytropic coefficients are set to $\gamma_{air} = 1.4$ and $\gamma_{water} = 7$.

In order to correctly take into account the compressibility effects in the air cavity the same value used in [49] for the gas speed of sound is adopted, that is $c_{0air} = 343$ m/s. As for the water sound speed, formula (2.65) is used to guarantee the weakly-compressible hypothesis in the impact region, this being the common choice in SPH to approximate incompressible fluids. Based on the expected maximum pressure variation $\Delta P_{\max} = 1$ atm in the cavity, the sound speed in water is obtained as:

$$c_{0water} = 10\sqrt{\Delta P_{\max}/\rho_{water}} = 100 \text{ m/s}.$$

Note that, following the stability conditions described in Section 2.4.2, the CFL coefficient is set equal to $K = 0.25$, with $\alpha = 0.07$. In order to avoid the mixing of air and water, the artificial surface tension correction of Eq. (2.32) is used, and the parameter ϵ_χ is set to 0.02.

In the following, the dimensionless variables are denoted by the superscript *. The length L is taken as reference length scale of the problem, unless specified otherwise; U and h/U are chosen as, respectively, the velocity and time scales; the ratio $P_{0air} = c_{0air}^2 \rho_{0air}/\gamma_{air}$ is taken as the pressure reference scale in the gas cavity.

Two discretizations were tested, $L/\Delta x = 160$ and 640. These values are based on the work of Marrone et al. [61], where the same type of corrugated panel was tested with a dead-rise angle of 4°, and in which these resolutions

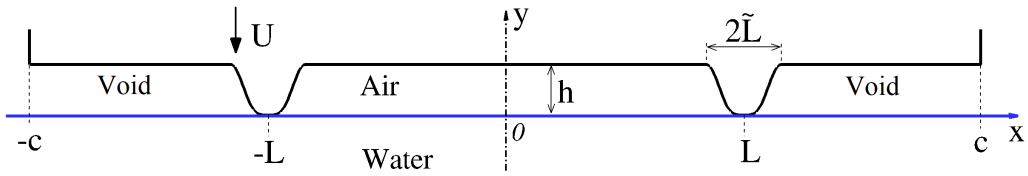

FIGURE 3.18: Fluid impact of a corrugated panel with trapped gas cavity: sketch of the initial configuration of the problem.

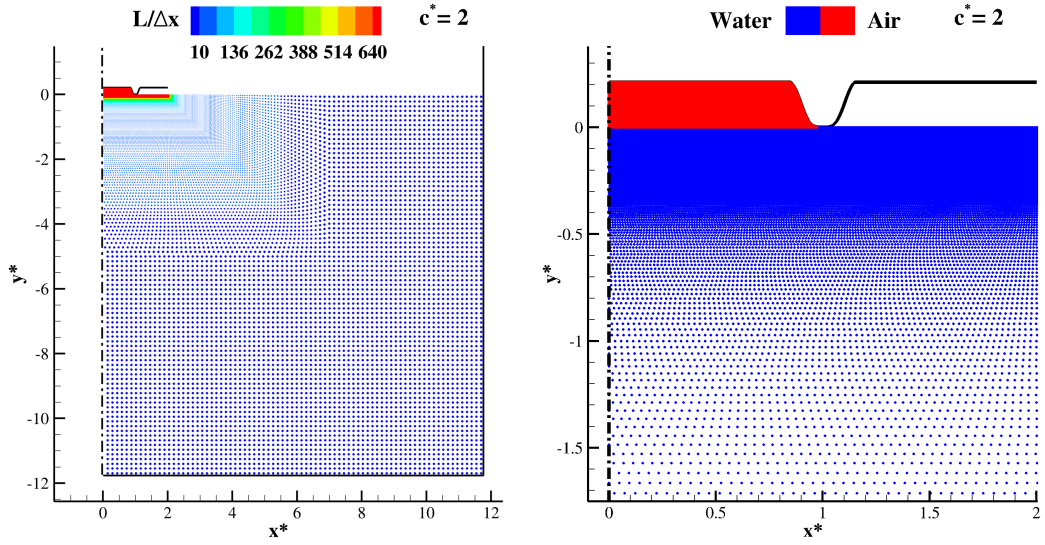

FIGURE 3.19: Fluid impact of a corrugated panel with trapped gas cavity. Left: Multi-resolution discretization of the domain. Right: Zoom on the gas cavity vicinity.

yielded satisfactory, convergent results.

Note that the panel impact generates several acoustic waves which would be reflected on the domain boundaries if the latter is not large enough, resulting in noisy pressure fields even in the air phase. Therefore, the domain is made sufficiently large and its dimensions were chosen simply by computing the distance which acoustic waves would travel during the impact at the adopted water sound speed.

The variable-h scheme discussed in [84] and described in Section 1.6.2.1 was used since the focus is on the gas cavity and its vicinity. The particle size varies between the air cavity and the domain boundaries from fine to coarse respectively, with a magnification factor of 100 between the smallest and biggest particles.

Since the problem is 2D symmetrical with respect to the line $x^* = 0$, a symmetry boundary condition was used. The adopted discretization for the finest case is shown in Fig. 3.19. Note that outside the corrugations, *i.e.* when $x^* > 1$, the air phase is not modeled so as to follow the configuration of the semi-analytical solution of Khabakhpasheva et al. [49] (see Fig. 3.18, the zones $|x| > L$ are not air but void).

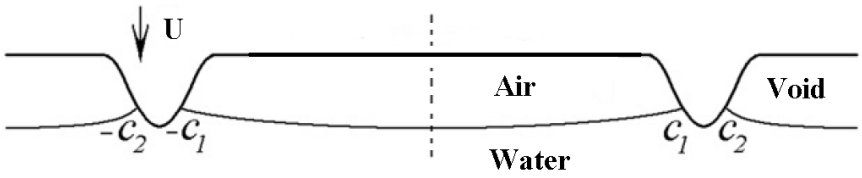

FIGURE 3.20: Fluid impact of a corrugated panel with trapped gas cavity: illustration of the inner and outer contact points.

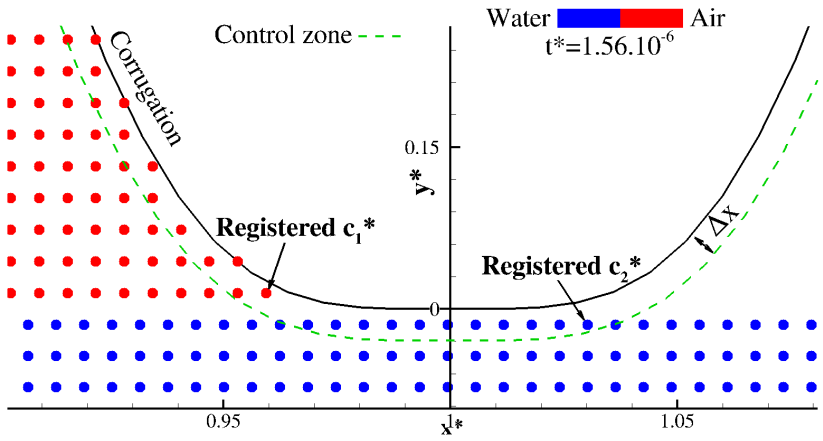

FIGURE 3.21: Fluid impact of a corrugated panel with trapped gas cavity: definition of the contact points after the first iteration.

3.4.1 Results and analysis: Kinematics

The focus here is on the case where the impact velocity and the non-dimensional length of the rigid panel are set to $U = 2$ m/s and $c^* = 2$. The obtained flow kinematics is studied by comparing and tracking the time evolution of the inner and outer contact points, referred to as c_1^* and c_2^* respectively, with the ones provided in [49]. The contact point are defined as the abscissa of the intersection between the water front and the panel for the outer contact point c_2^*, and as the triple point air/water/panel for the inner contact point c_1^*, which are illustrated in Fig. 3.20.

In our simulations, the contact points definition was implemented as follows (see Fig. 3.21):

- First, a control zone is defined by setting a criterion of distance to the corrugation wall. In particular, only particles with maximal distance to the panel smaller than Δx are considered in the control zone, in order to guarantee the presence of at least one particle.
- Then, at each iteration the abscissas of the two air and water particles inside the control zone and with the highest absolute x*-coordinates, are recorded as the inner and outer contact points, respectively (see Fig. 3.21).

Fig. 3.22 shows the evolution of the air/water flow through four snapshots at different instants. After the panel hits the water surface, its corrugations penetrate it, and the air cavity starts to compress. Shortly after, the extremities of the cavity start to creep under the corrugations and towards the outside of the panel. This air movement is accompanied with the water jet in the outer region freely moving towards the outside of the panel.

In Fig. 3.23 the evolution of the SPH contact points c_1^* and c_2^* are plotted against the ones from [49]. The general trend of the predicted outer contact point follows closely its semi-analytical counterpart. Also, the slope of both curves changes at around $t^* = 0.5$, when the water front reaches the intersection between the corrugation and the horizontal part of the panel, where a change of convexity occurs. Finally, both these curves stagnate at $c_2^* = 2$ since it corresponds to the extremity of the panel.

The time evolution of the contact points is subdivided into four stages:

Stage 1) $t^* \leq 0.45$ is the compression stage of the entrapped cavity. At $t^* = 0.41$ an increase of the inner contact point abscissa is registered, which means the creeping of the cavity towards the outside of the corrugation.

Stage 2) It is characterized by the formation of a high speed water jet which sucks the cavity towards the outside of the corrugation.

Stage 3) After the jet reaches the end of the panel, the suction effect decays. As the panel continues to penetrate the water, the cavity resumes its compression in this stage.

Stage 4) Around $t^* = 0.9$, the gas cavity begins its decompression, as better explained in the upcoming subsection 3.4.2 where the dynamic part of the solution is investigated.

Note that the curves do not begin exactly at the same starting x*-coordinate. This is a consequence of the adopted definition for the contact point. Indeed, as shown in Fig. 3.21, at the beginning of the simulation the particles identified as contact points do not lie exactly on the axis $x^* = 1$, this difference decreasing as the resolution increases.

There are some differences between the SPH and semi-analytical slopes which are limited and reflect the different natures of the solutions being compared. As for the inner contact point c_1^*, it is strictly linked to the volume variations of the air cavity. In Khabakhpasheva et al. [49] the air cavity was prevented from reaching the head of the corrugation ($x^* = 1$) by imposing the condition $\dot{c}_1 \leq 0$; with this constraint the horizontal velocity of the inner contact point always points towards the center of the cavity, which means that the air will never flow under the corrugation. In the present simulations however, no condition on the inner contact point's velocity is enforced, so that the cavity is left to freely evolve in time.

This difference in behavior can be observed in Fig. 3.23 for c_1^* at $t^* \simeq 0.45$. As expected, the condition $\dot{c}_1 \leq 0$ strongly influences the kinematics of the air cavity. Indeed, the constrained contact point does not deviate much from its original position whereas, without constraints, the air cavity starts

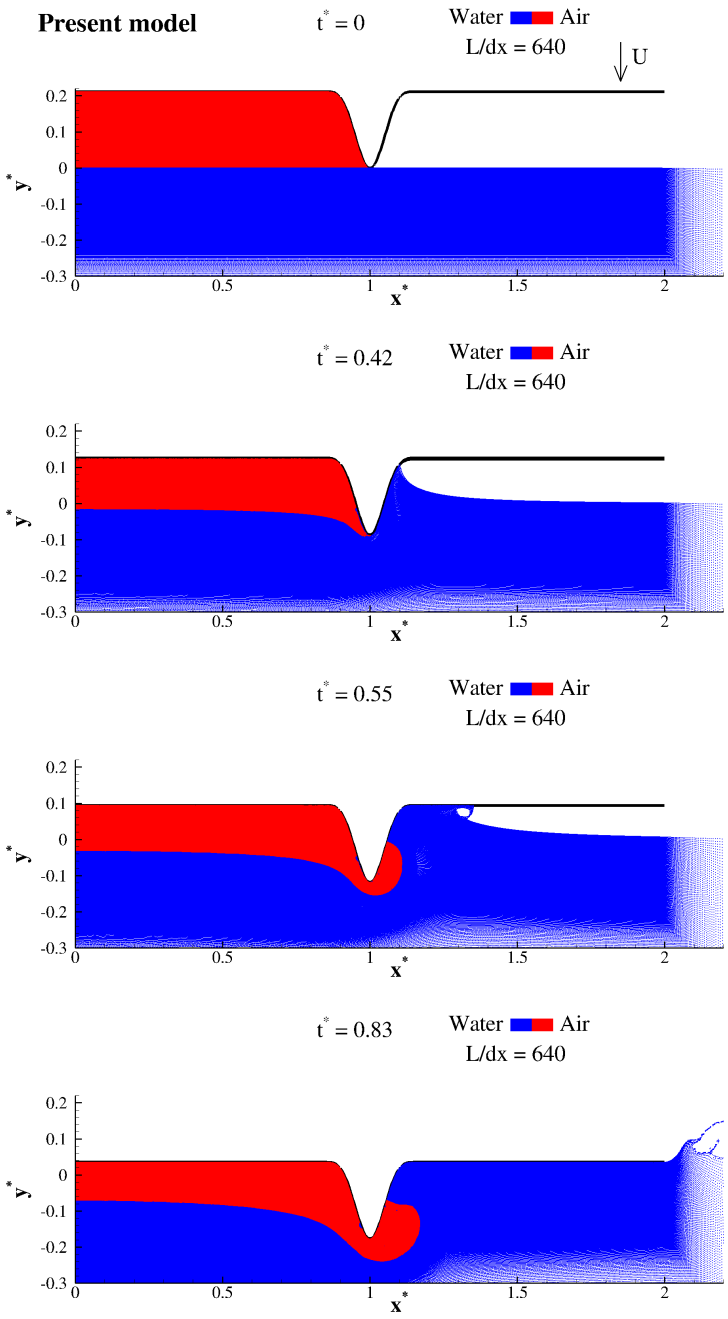

FIGURE 3.22: Fluid impact of a corrugated panel with trapped gas cavity: evolution of the air/water interface and free-surface flows upon impact, at four different instants.

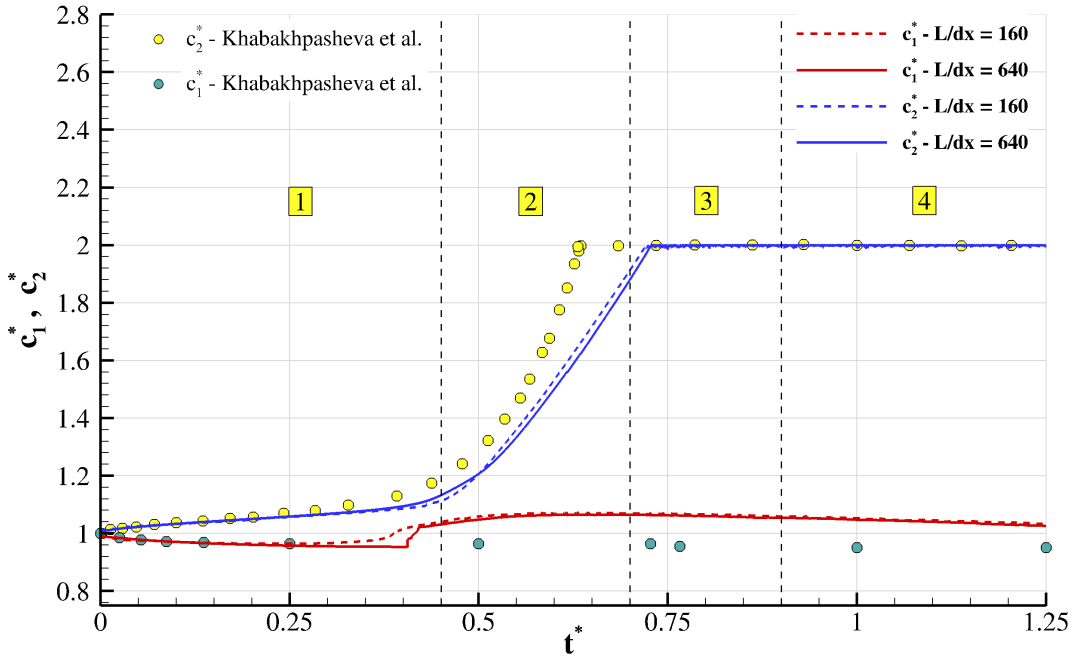

FIGURE 3.23: Fluid impact of a corrugated panel with trapped gas cavity: evolution of the SPH/semi-analytical inner and outer contact points c_1^* and c_2^* for a panel length $c^* = 2$. The time evolutions are divided into 4 stages.

to move towards the outer region under the corrugation, as seen in Fig. 3.22. Moreover, up to $t^* = 0.25$ both models predict the same evolution of the air cavity.

3.4.2 Results and analysis: Dynamics

In this subsection, the pressure evolution inside the gas cavity is analyzed and compared to its semi-analytical counterpart. First, the simulation results using coarse ($L/\Delta x = 160$) and fine ($L/\Delta x = 640$) discretization levels are plotted in Fig. 3.24, showing close to converged results, even in terms of pressure (see also Fig. 3.23 to observe this convergence). The SPH solution can be viewed as a succession of 4 stages as was done for the discussion of the solution kinematics (see subsection 3.4.1):

Stage 1) A compression of the gas occurs up to $t^* = 0.45$, during which the pressure grows linearly akin to an elastic reaction, due to the homogeneous water load around it as shown in Fig. 3.25.

Stage 2) During the high speed water jet motion, the cavity is sucked towards the outside of the corrugation inducing a relaxation in the gas cavity during which the pressure decreases.

Stage 3) After the jet reaches the end of the panel, the suction effect decays and is counterbalanced by the water pressure from under the gas cavity. Therefore, as the panel continues to penetrate the water, the cavity resumes its compression in this stage.

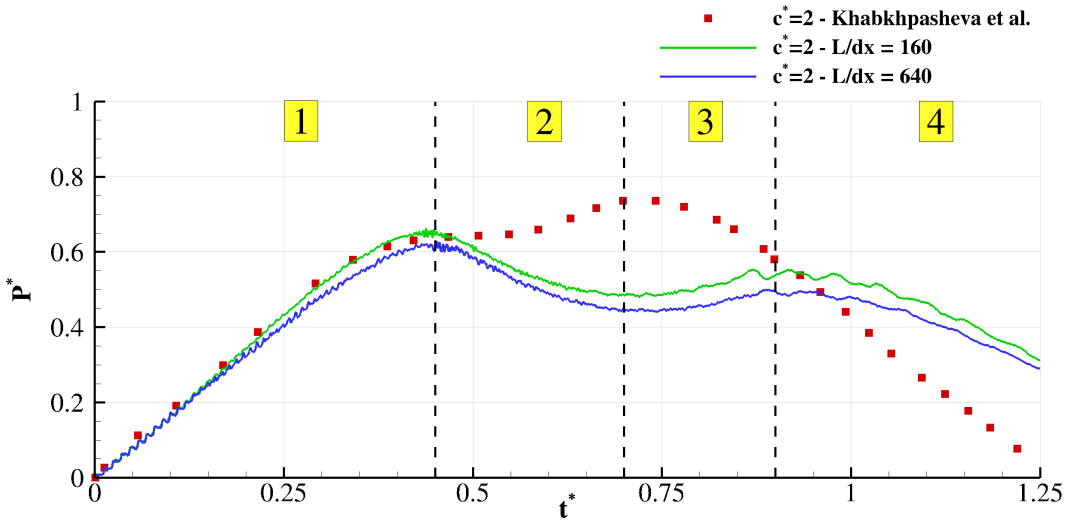

FIGURE 3.24: Fluid impact of a corrugated panel with trapped gas cavity: comparison with the semi-analytical solution of the pressure inside the cavity, for a panel length $c^* = 2$. The pressure curve is divided into 4 stages.

Stage 4) Around $t^* = 0.9$, the pressure reaches its second peak then the gas cavity begins its decompression as the loads balance out during this final stage.

Interestingly, both the SPH and semi-analytical solutions predict these four phases. The major difference is in Stage 2 where the SPH pressure decreases but the semi-analytical one stagnates. In [49], the pressure is directly linked to the volume through the following equation:

$$P(t) = [V(t)]^{-\gamma} - 1 \tag{3.3}$$

and the volume itself is strongly dependent on the inner contact point evolution $c_1(t)$. The speed $\dot{c}_1$ is computed at each time step and is set to zero if the computed value is positive. The reasoning behind this condition is extensively covered in [49]. Thus the contact point is prohibited from ever moving towards the outside of the corrugation, which means that the cavity volume either decreases or stagnates. Consequently, following Eq. (3.3), the semi-analytical pressure can only stagnate or increase. Nevertheless, both models predict the elastic compression in Stage 1, a second pressure rise in Stage 3, and a final decompression in Stage 4, although at different times/pressure levels due to the differences in constraints between the SPH and semi-analytical frameworks. Note that authorizing c_1 to go outwards would largely increase the complexity of the semi-analytical solution where a shape of the pocket leakage outside the corrugation would have to be imposed.

Next, the effect of the panel length on the cavity pressure is investigated. The numerical and geometrical configurations are kept unchanged, however this time the panel length $c^* = 3$. The simulation was run with the fine discretization ratio $L/\Delta x = 640$. Fig. 3.26 compares the evolutions of the

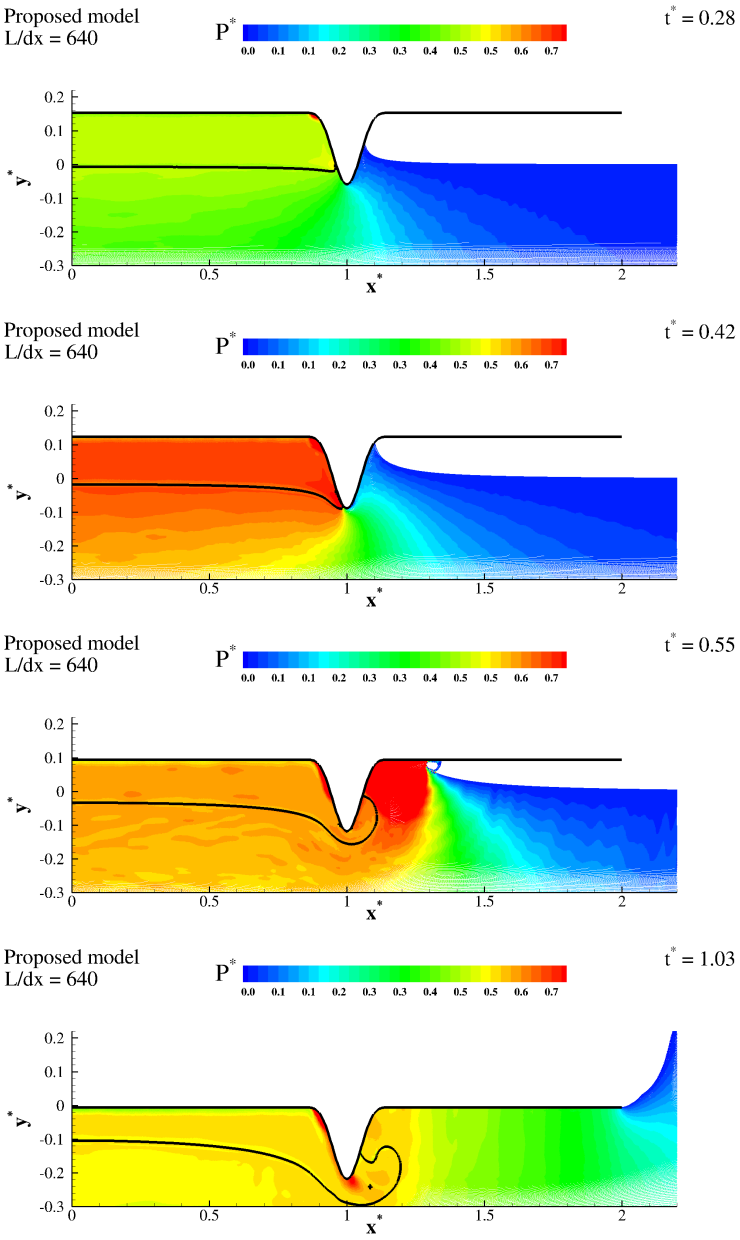

FIGURE 3.25: Fluid impact of a corrugated panel with trapped gas cavity: pressure field during the impact stages for four different time instants $t^* = 0.014, 0.42, 0.55, 0.90$. The panel length is $c^* = 2$.

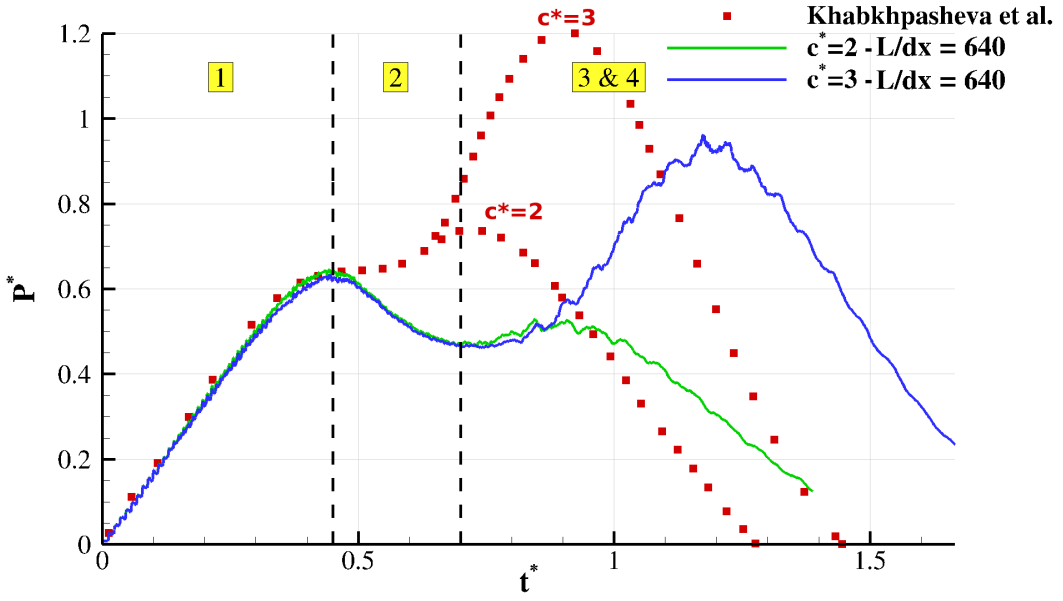

FIGURE 3.26: Fluid impact of a corrugated panel with trapped gas cavity: semi-analytical and computed pressure profiles in the cavity, for panel lengths of $c^* = 2$ and 3.

cavity pressures for both panel lengths $c^* = 2$ and $c^* = 3$. Fig. 3.26 regroups the semi-analytical and computed pressure solutions for both panel lengths $c^* = 2$ and 3, from which some general conclusions can be made.

First, in accordance with [49], the shorter the panel, the lower the pressure inside the cavity. Also, right away it can be seen that both pressure curves follow the same general trend, in the sense that they both predict the aforementioned 4 stages. The curves are superimposed during Stages 1 and 2 which is expected since the water does not reach c^* yet. The solution with the larger panel agrees with the conclusions made for the shorter panel, meaning that the SPH pressure follows closely the semi-analytical one in terms of compression + relaxation in Stage 3 and 4, albeit at different pressure levels since the air cavity is not constrained within the SPH model, while it is set to move only towards the inside within the semi-analytical model.

Chapter 4

A comparison between the Multiphase δ-SPH scheme and Riemann-based SPH schemes

The Riemann-based SPH schemes were introduced as a way of improving the stability and robustness of the SPH method. Contrary to the SPH schemes based on diffusive/viscous terms, Riemann-SPH schemes do not rely on parameters dedicated to tune the diffusive terms. However, this feature can be considered as a disadvantage of the method as much as it is an advantage, since without parameter tuning the numerical diffusion of Riemann-SPH schemes cannot be controlled.

As presented in Section 1.4.3, Riemann-SPH schemes are more expensive than diffusive term-based SPH schemes. Indeed, on the one hand, it absolutely necessitates the MUSCL correction to increase its convergence order [55], and on the other hand, a particle shifting algorithm is highly recommended in order to avoid the anisotropic particle clustering discussed in Section 1.6.1.

This being said, despite these drawbacks many works in the literature proved the interesting improvements that the Riemann-SPH schemes offer, especially in terms of stability, regularity of the pressure field and energy conservation. Therefore, the present chapter aims to compare the proposed Multiphase δ-SPH scheme with the Riemann-SPH scheme presented in Section 2.1.4. This investigation focuses on the differences between the pressure fields yielded by each scheme, their mechanical energy dissipation, and their regions of stability in a multiphase context, as it was established for the Multiphase δ-SPH scheme in Section 2.4.

The test cases presented in Section 3 are performed here using the Riemann-SPH scheme. For the sake of balance, the Riemann-SPH simulations were run with and without the particle shifting method of Oger et al. [83]. Indeed, no particle shifting algorithm was implemented for the Multiphase δ-SPH scheme, which means that the comparison with Riemann-SPH with shifting would skew the results in favor of the latter.

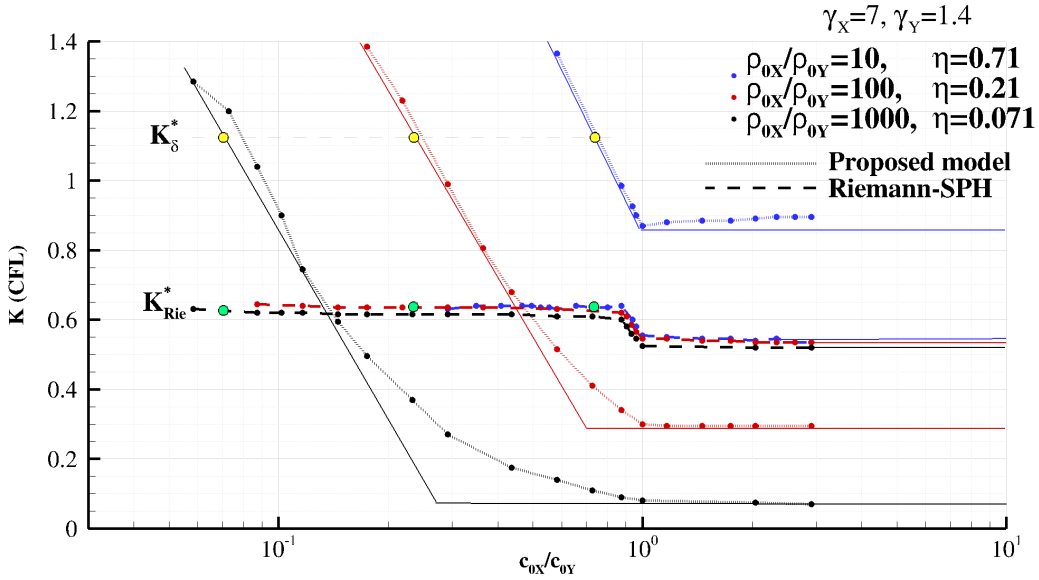

FIGURE 4.1: Two-phase 1D Bagnold problem: comparison of the stability regions of the Riemann-SPH and Multiphase δ-SPH schemes. The dotted and dashed lines represent respectively the Multiphase δ-SPH and Riemann-SPH schemes. The regression lines delimiting the regions of stability of each scheme are plotted in solid lines, and each density ratio is represented by a specific color. The yellow/green bullets represent the points where $c_{0X}/c_{0Y} = \eta$ and $K = K^*$ for the Multiphase δ-SPH/Riemann-SPH schemes.

4.1 Stability regions in a multiphase context

The 1-D Bagnold problem [4] studied in Section 2.4 is rerun here using the Riemann-SPH scheme. The idea is to compare its stability region with the Multiphase δ-SPH scheme's one in a multiphase configuration. All the numerical parameters are kept similar to the ones used in Section 2.4.

The flow is 1-D in the vertical direction so the particles are not expected to stray from their initial Cartesian abscissas. Therefore, there is no need to use a particle shifting algorithm in this particular case.

The three density ratios $\rho_{0X}/\rho_{0Y} = 10, 100, 1000$ are again considered here. The stability region of the Riemann-SPH scheme is plotted in Fig. 4.1 in the plane $(c_{0Y}/c_{0X}, K)$, along with the stability curves of the Multiphase δ-SPH scheme for comparison purposes.

Many interesting stability properties can be drawn out from this figure. It should be noted that one sound speed ratio in particular stands out from all the graphs corresponding to the different tested permutations of the Multiphase δ-SPH/Riemann-SPH schemes and density/sound speed ratios, which is the ratio $c_{0X}/c_{0Y} = 1$. Indeed, before and after this point the stability regions of both schemes do not exhibit the same properties. Therefore, the analysis of the results plotted in Fig. 4.1 is segmented into two zones: before $c_{0X}/c_{0Y} = 1$ and after $c_{0X}/c_{0Y} = 1$.

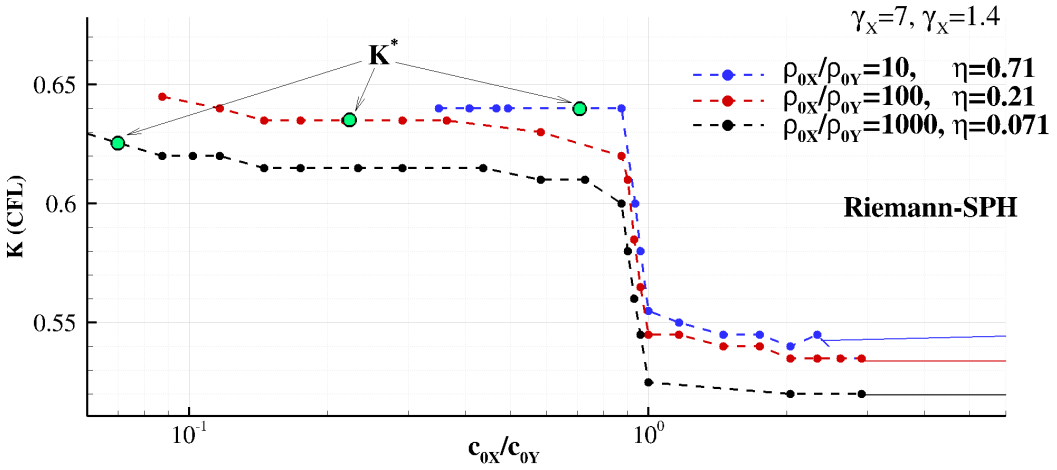

FIGURE 4.2: Two-phase 1D Bagnold problem: zoomed view of the stability regions of the Riemann-SPH scheme. The green bullets represent the points where $c_{0X}/c_{0Y} = \eta$ and $K = K^*$ for the Riemann-SPH scheme.

Firstly, in the zone where $c_{0X}/c_{0Y} > 1$ the stability regions of both schemes is delimited by a horizontal line regardless of the density or sound speed ratios. Any horizontal line can be viewed as a threshold below which the simulations are always stable.

Secondly, the stability regions of the Multiphase δ-SPH scheme seem to be very sensitive to the variation of density ratios in comparison to the Riemann-SPH scheme. As seen in Fig. 4.1, increasing the density ratio imposes lower CFL coefficients for the Multiphase δ-SPH scheme. For example, at $c_{0x}/c_{0y} = 1$, the parameter K goes from 0.87 to 0.08 between the density ratios 10 and 1000, signifying a considerable decrease of 90%.

In contrast, the stability of the Riemann-SPH scheme is not as sensitive to this change of density ratio, as the stability curves corresponding to the three density ratios are close to be superimposed. Indeed, for instance at $c_{0X}/c_{0Y} = 1$, K goes from 0.55 to 0.52 which corresponds to a decrease of only 5% for the Riemann-SPH scheme.

For clarity purposes, Fig. 4.2 shows a zoom on the stability curves of the Riemann-SPH scheme. The zone $c_{0X}/c_{0Y} < 1$ can also be divided in two sound speed intervals. The first interval is defined by $c_{0X}/c_{0Y} \in [0.87, 1]$, where regardless of the density ratio the parameter K undergoes a linear decrease. The second interval corresponds to $c_{0X}/c_{0Y} < 0.87$ where the stability curves are once again quasi-horizontal, similarly to the zone $c_{0X}/c_{0Y} > 1$ where the CFL threshold slightly changes depending on the density ratio. Consequently, within this zone, the maximal stable CFL coefficients allowed when using the Riemann-SPH schemes are capped by this threshold ($K^*_{Rie} \approx 0.62$). On the other hand, the Multiphase δ-SPH scheme allows up to nearly double this value ($K^*_\delta \approx 1.13$) when $c_{0X}/c_{0Y} = \eta$, which is very advantageous in terms of CPU costs.

However, as explained in Section 2.4, choosing the sound speed is usually linked to physical considerations, which means that the ratio $c_{0X}/c_{0Y} = \eta$

may not be achievable in order to guarantee the weakly-compressible regime. Therefore, smaller time steps can sometimes be unavoidable with the Multiphase δ-SPH scheme.

Next, the dam-break flow and the fluid impact on a corrugated flat panel test cases, presented in Section 3.3 and 3.4 respectively, will be performed using the Riemann-SPH scheme, and the results will be compared to the Multiphase δ-SPH scheme validations results. These more complex simulations involve a free-surface and are much more susceptible to particle clustering compared to the 1-D Bagnold test, which sheds more light on the computational demands of each SPH model.

4.2 Pressure field and mechanical energy decay

4.2.1 Single phase case: dam-break flow

The configuration of the single-phase dam-break flow described in Section 3.3 is kept unchanged. In this study, the case where the parameter α of the Multiphase δ-SPH scheme is taken equal to 0 is studied first.

The highest adopted particle discretization for all configurations is $H/\Delta x = 400$. The speed of sound is chosen so as to verify the weakly-compressible approach based on the expected maximal pressure P_{max} within the flow. The value of P_{max} is taken directly from the experimental results of Lobovský et al. [58], which for our case is $P_{max} \approx 9.1$ kPa. Thus, following Eq. (2.65), the adopted sound speed is $c_0 = 32$ m/s in all the following simulations.

4.2.1.1 Pressure field

Fig. 4.3 shows the first impact of the fluid against the impact wall for the Multiphase δ-SPH scheme and for the Riemann-SPH scheme with and without shifting, for the finest discretization $H/\Delta x = 400$. A zoom on the bottom right corner of the tank is also provided.

At first glance, the three schemes seem to yield a similar repartition of pressure within the fluid, with the Multiphase δ-SPH scheme exhibiting slightly more pressure oscillations. However, by zooming on the impact corner, we can observe in the bottom plot of Fig. 4.3 the anisotropic particle structures of the purely Lagrangian Riemann-SPH scheme, which completely vanish when using particle shifting (middle plot) [83].

More interestingly, the top plot shows that the Multiphase δ-SPH scheme does not exhibit such particle structures even in the absence of a particle shifting technique, which can be considered as a plus of the proposed model. Indeed, this technique is linked to a free-surface capturing algorithm to maintain the kinematic free-surface condition by avoiding shifting onto the free-surface particles (*cf.* Marrone et al. [63]). Consequently, this increases the number of loops over the particles which naturally inflates the CPU time.

For instance, Table 4.1 presents the CPU times of the dam-break simulations using the Multiphase δ-SPH scheme and both Riemann-SPH schemes

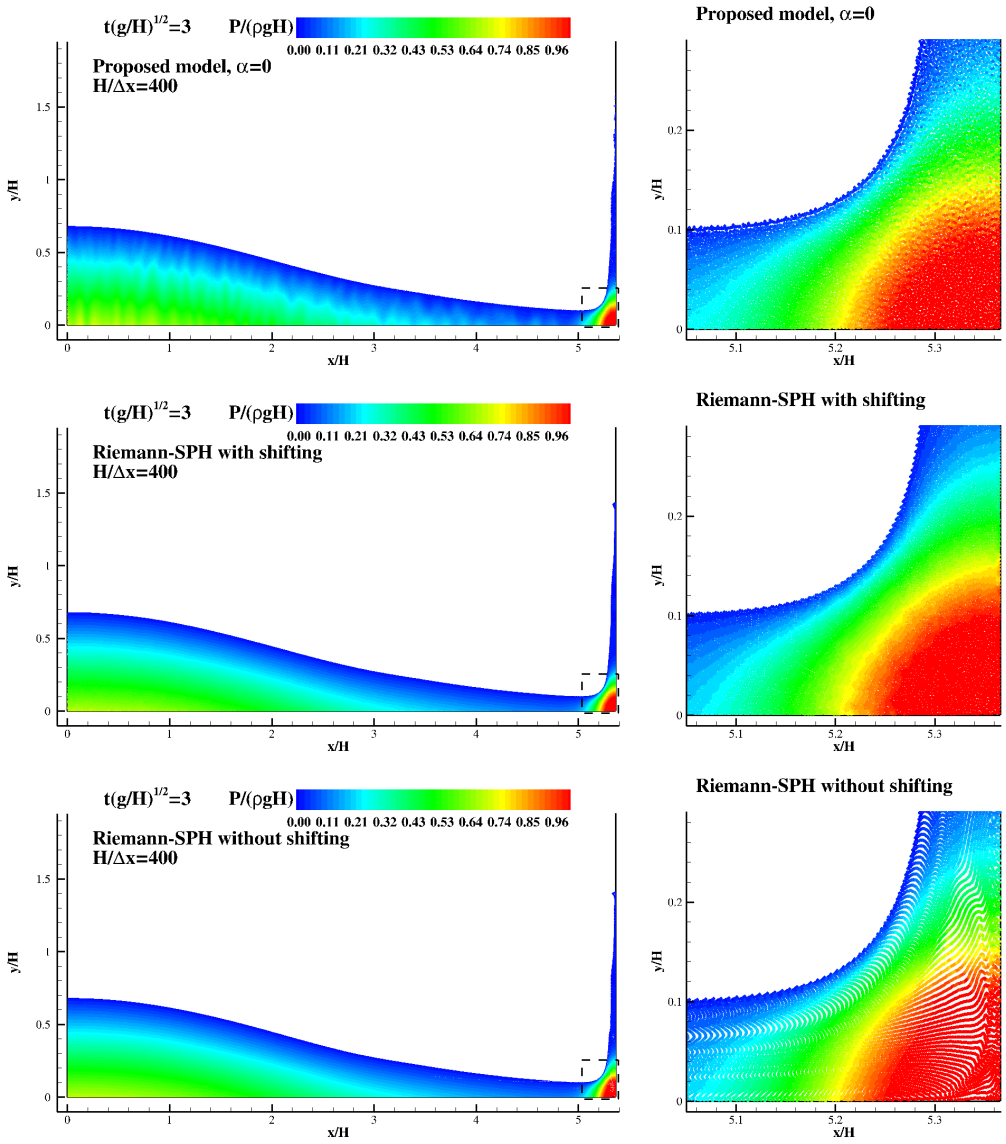

FIGURE 4.3: Single-phase dam-break: snapshots of the flow at $t\sqrt{g/H} = 3$, obtained with the Multiphase δ-SPH scheme, and with the Riemann-SPH scheme with and without particle shifting. Zoomed views of the impact corner are provided on the right of each snapshot.

SPH model	CPU time (s)	
Proposed model	446	3921
Riemann-SPH without PS	1151	7202
Riemann-SPH with PS	1434	9069
$H/\Delta x$	200	400

TABLE 4.1: Single-phase dam-break: comparison of the CPU times between the Multiphase δ-SPH, and Riemann-SPH schemes with and without particle shifting (PS), for two spatial resolutions.

(without and with particle shifting), for two spatial resolutions $H/\Delta x = 200, 400$. The CFL coefficient $K_\delta = K_{Rie}$ was taken equal to 0.375 to accommodate the stability of the single-phase Riemann-SPH model, although with the Multiphase δ-SPH scheme it is possible to increase the CFL coefficient up to 0.75 for single-phase simulations. The highest resolution dam-break simulation took only 1.1h using the Multiphase δ-SPH scheme, compared to 2.5 h and 2 h using the Riemann-SPH with and without particle shifting, respectively.

Note that, to moderate this positive comment, leaving Lagrangian alignments as in the Riemann-SPH solution without shifting is per se a sign of accuracy since the Lagrangian nature of the method is better respected.

Fig. 4.4 shows the recorded pressure on sensor P_1 for the three schemes. The pressure signals have the same evolution, the only difference being that the Multiphase δ-SPH scheme exhibits more oscillations upon the plunging wave impact. The three models predict the same pressure peak as the experimental data by Lobovský et al. [58], and the pressure offset that follows the impact can be explained by the 3D effects present in the experiments, and which cannot be captured using the current 2D simulations. All in all, the Multiphase δ-SPH scheme seems to yield satisfactory pressure results with regard to the Riemann-SPH scheme, while being less demanding in terms of CPU costs (*cf.* Table 4.1).

Note that the Multiphase δ-SPH scheme displays more pressure oscillations upon the wave impact than Riemann-SPH, as observed in Fig. 4.5. This is due to taking the viscous parameter α equal to 0. An additional computation with the Multiphase δ-SPH scheme was performed, this time taking $\alpha = 0.005$, which yielded clearly better results in terms of further filtering out the oscillations from the pressure field, see Fig. 4.6.

4.2.1.2 Mechanical energy decay

Next, the mechanical energy is monitored for the three schemes. Fig. 4.7 shows the mechanical energy decay obtained using the Multiphase δ-SPH scheme with $\alpha = 0$ and $\alpha = 0.005$, and using the Riemann-SPH scheme with and without shifting. As in Oger et al. [83], the mechanical energy is non-dimentionalized by the difference between the initial and final potential

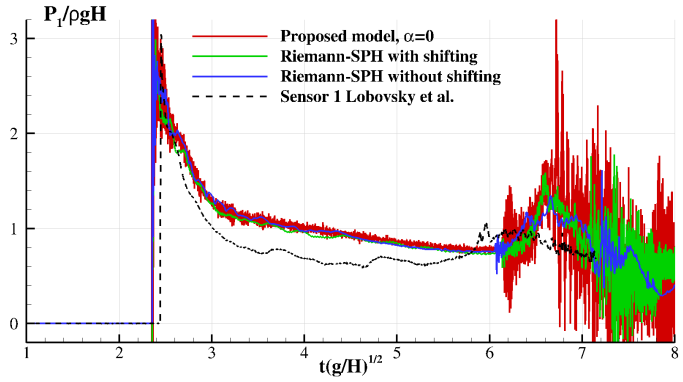

FIGURE 4.4: Single-phase dam-break: pressure signals recorded on sensor P_1 using the Multiphase δ-SPH scheme ($\alpha = 0$), and Riemann-SPH with and without shifting.

energy, the latter corresponding to the configuration where the fluid is at rest and filling the whole tank width.

As expected, the Riemann-SPH scheme without shifting is the more dissipative of the three schemes. As explained in [83], the anisotropic particle distribution damages the accuracy of the SPH operators which in turn leads to larger energy dissipation.

The four schemes seem to dissipate energy at the same rate up to about $t\sqrt{g/H} = 2.36$ which corresponds to the first impact of the fluid on the right wall (illustrated in Fig. 4.3). Then, the Riemann-SPH scheme without shifting starts to dissipate the energy at a higher rate. Moreover, increasing α to 0.005 induces a slight increase in the energy dissipation, which is an expected result [68]. However, the dissipations of the Multiphase δ-SPH scheme without artificial viscosity and the Riemann-SPH scheme with shifting are quite similar throughout the simulation.

Later in time, at around $t\sqrt{g/H} = 6.1$ the plunging motion occurs as shown in Fig. 4.5. All models display a second, more abrupt change of mechanical dissipation rate. This is explained by the fact that the plunging jet is a phenomenon that triggers numerical dissipation [60, 83]. At the end of the simulation, the registered dissipation rate of the Multiphase δ-SPH scheme and the Riemann-SPH scheme is less than half the dissipation rate of the Riemann-SPH scheme without shifting.

4.2.2 Multiphase case: fluid impact of a corrugated panel with entrapped gas cavity

The problem of water entry of a corrugated panel with a trapped gas cavity described in detail in Section 3.4 is rerun using the Riemann-SPH scheme. The physical parameters of the water and air phases and, for the proposed Multiphase δ-SPH model, the numerical parameters $\alpha = 0.07$ and $\delta = 0.1$, are all kept unchanged from Section 3.4.

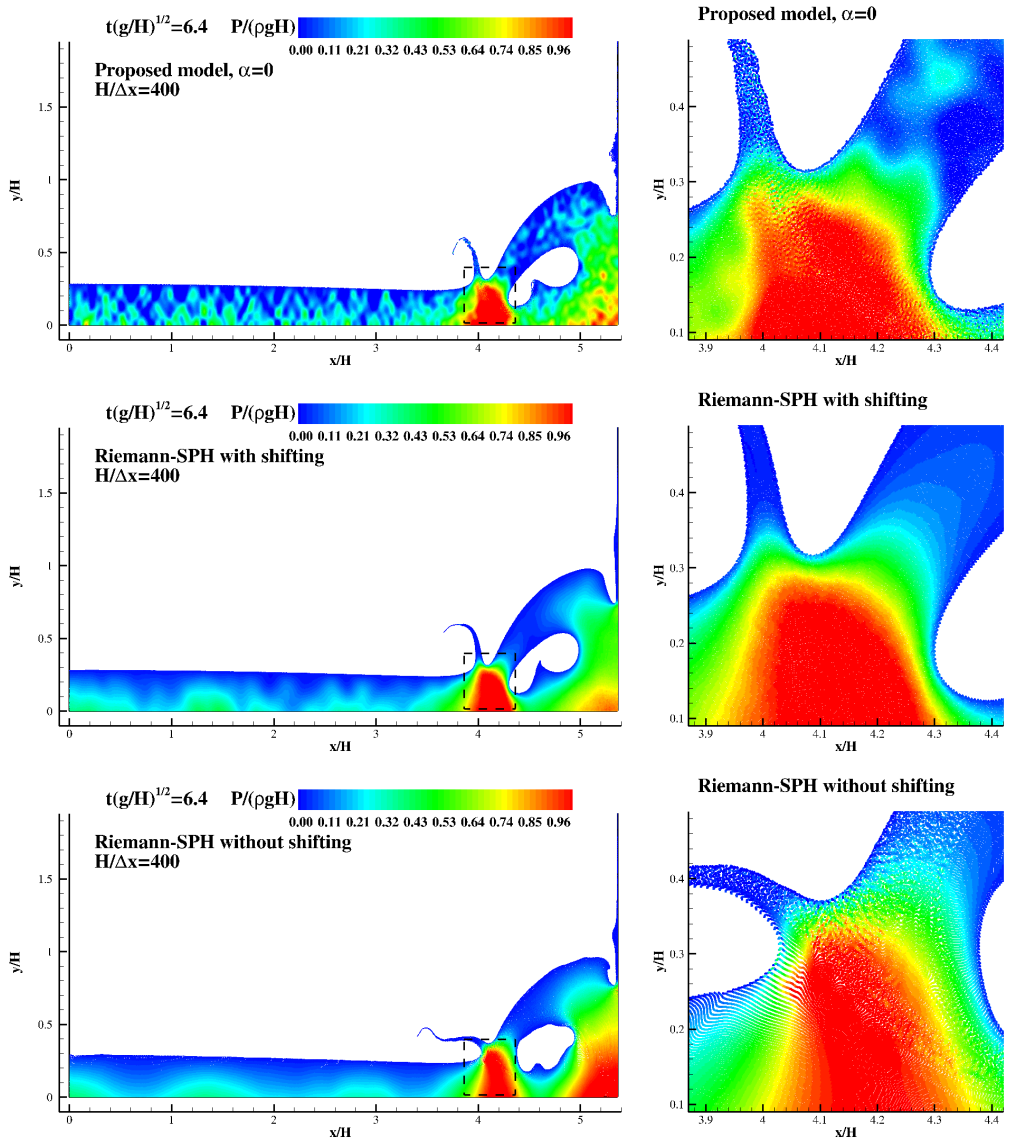

FIGURE 4.5: Single-phase dam-break: snapshots of the flow at $t\sqrt{g/H} = 6.4$, obtained with the Multiphase δ-SPH scheme and the Riemann-SPH scheme with and without particle shifting. Zoomed views on the plunging wave impact zone are provided on the right of each snapshot.

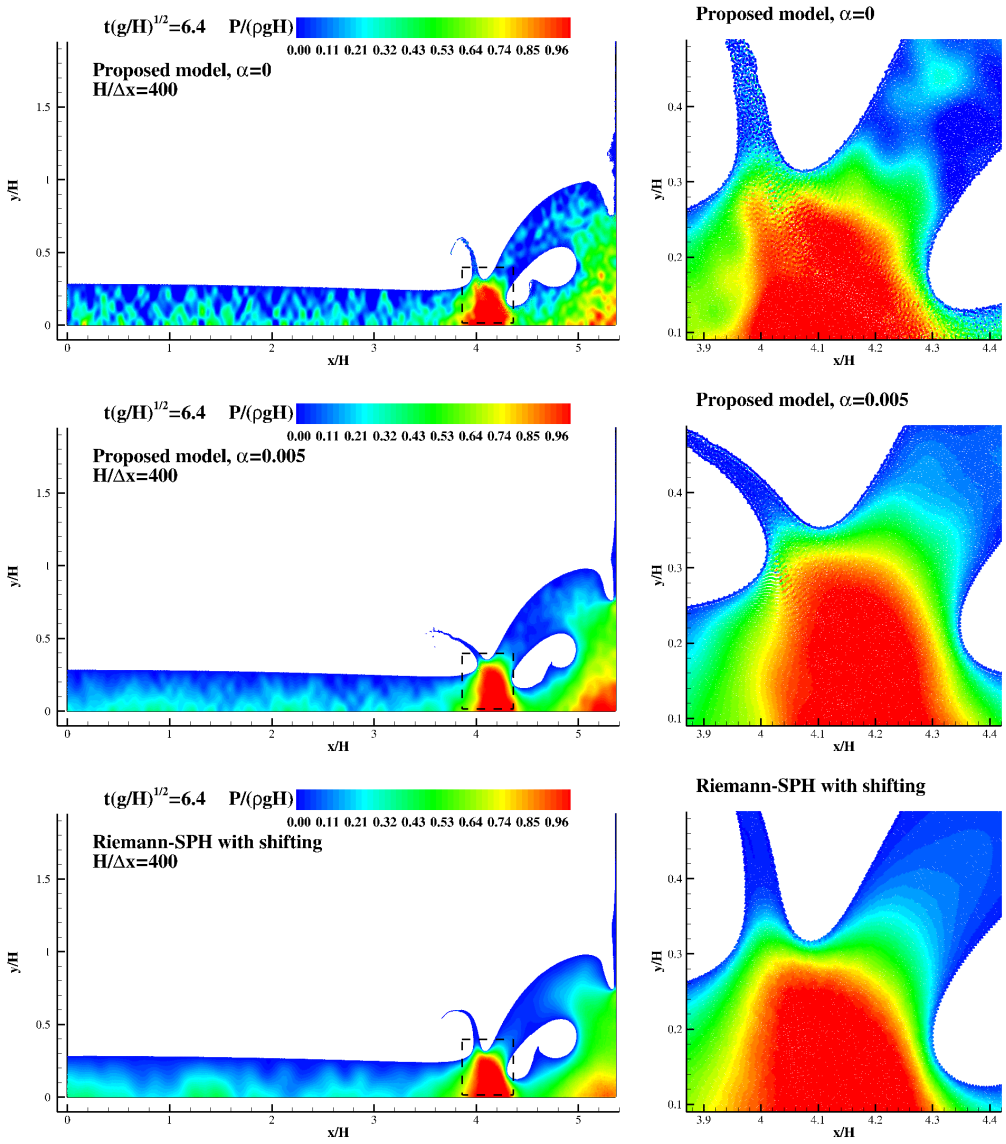

FIGURE 4.6: Single-phase dam-break: snapshots of the flow at $t\sqrt{g/H} = 6.4$, obtained with the Multiphase δ-SPH scheme with $\alpha = 0$ and $\alpha = 0.005$, and the Riemann-SPH scheme with shifting. The small increase of α strongly improves the pressure field.

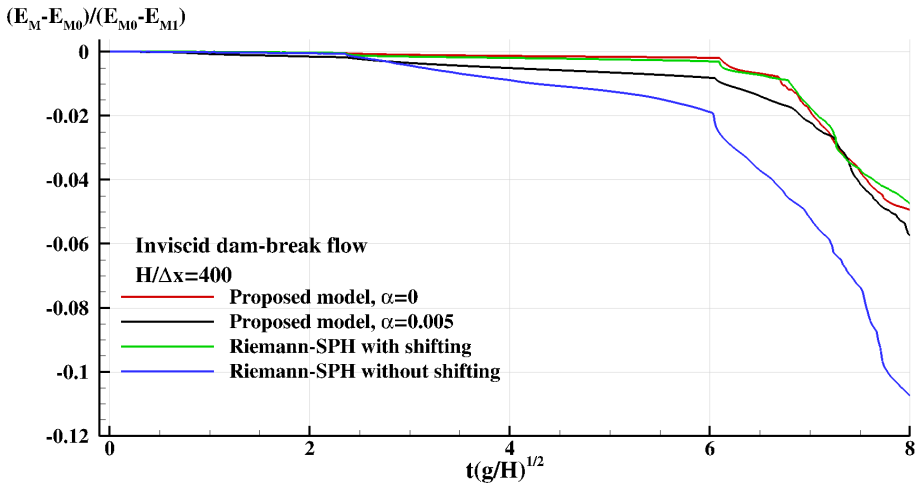

FIGURE 4.7: Dam-break flow: comparison of the mechanical energy decay between the Multiphase δ-SPH scheme (with $\alpha = 0$ and $\alpha = 0.005$) and the Riemann-SPH scheme (with and without shifting).

The choice of the fluid sound speeds is based on the weakly-compressible approach as in Section 3.4, *i.e.* $c_{0water} = 100$ m/s and $c_{0air} = 343$ m/s, which corresponds to a sound speed ratio of $c_{0water}/c_{0air} = 0.29$. Following the stability analysis of the Riemann-SPH scheme presented in Section 4.1, the CFL coefficient K_{Rie} is taken equal to 0.6 (while $K_\delta = 0.25$ for the Multiphase δ-SPH scheme, as in Section 3.4). All the computations have been run with the finest spatial resolution, $L/\Delta x = 640$.

Fig. 4.8 compares the time evolution of the contact points c_1^* and c_2^* obtained through the Multiphase δ-SPH scheme and the Riemann-SPH scheme, for the panel length $c^* = 2$. We can observe that the Riemann-SPH scheme predicts an evolution of the contact points which is very similar to the one obtained via the Multiphase δ-SPH scheme. Indeed, both models yield a time evolution that could be divided into the four stages already discussed in Section 3.4.1.

Fig. 4.9 shows the pressure field inside the air and water phases yielded by the Multiphase δ-SPH and Riemann-SPH schemes, at different time instants which represent the four impact phases described in Section 3.4.1.

Overall both models yield the same repartition of pressure within the air and water phases, despite some minor differences. Indeed, the Multiphase δ-SPH scheme predicts a slightly higher pressure within the entrapped air cavity. This observation is verified by comparing the average pressure within the air phase plotted for both schemes in Fig. 4.10. Moreover, on this figure some small oscillations of pressure are observed for the Multiphase δ-SPH scheme throughout Phases 2 and 3. Although they do not seem to affect the solution, it is possible to eliminate them simply via a small increase of the viscous parameter α, similarly to the dam-break case where $\alpha = 0 \rightarrow 0.005$ was sufficient to eliminate the noise within the pressure field (see, *e.g.*, Fig. 4.6).

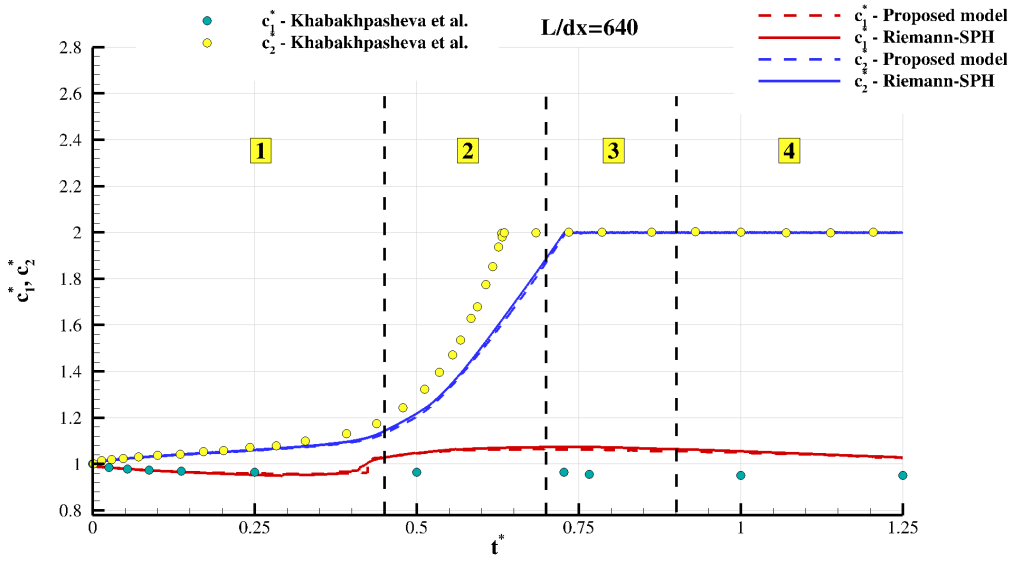

FIGURE 4.8: Fluid impact of a corrugated panel with entrapped gas cavity: comparison of the time evolution of the contact points c_1^* (in red) and c_2^* (in blue) predicted by the Multiphase δ-SPH (dashed lines) and Riemann-SPH schemes (solid lines).

SPH model	K	CPU time (s)
Proposed model	0.25	4456
Riemann-SPH with PS	0.6	4991

TABLE 4.2: Fluid impact of a corrugated panel with entrapped gas cavity: comparison of the CPU times between the Multiphase δ-SPH and Riemann-SPH with particle shifting (PS) schemes.

Moreover, a local increase of pressure is predicted by the Multiphase δ-SPH scheme in the air phase at the inner corner of the corrugation, which propagates throughout the simulation across and beyond the corrugation, as seen between $t^* = 0.28$ and $t^* = 1.03$. This difference is due to the lack of particle shifting near these round corners. Indeed, the same overpressure was registered in the simulation using the Riemann-SPH scheme without shifting, as illustrated in Fig. 4.11.

Table 4.2 presents the CPU times of the simulations. The Multiphase δ-SPH scheme still yields slightly faster results even though the maximal stable CFL coefficient (0.25) is 2.4 smaller than the Riemann-SPH model (0.6). In fact, at equivalent K, the Multiphase δ-SPH scheme seems to be around 2.7 times faster in this multiphase context.

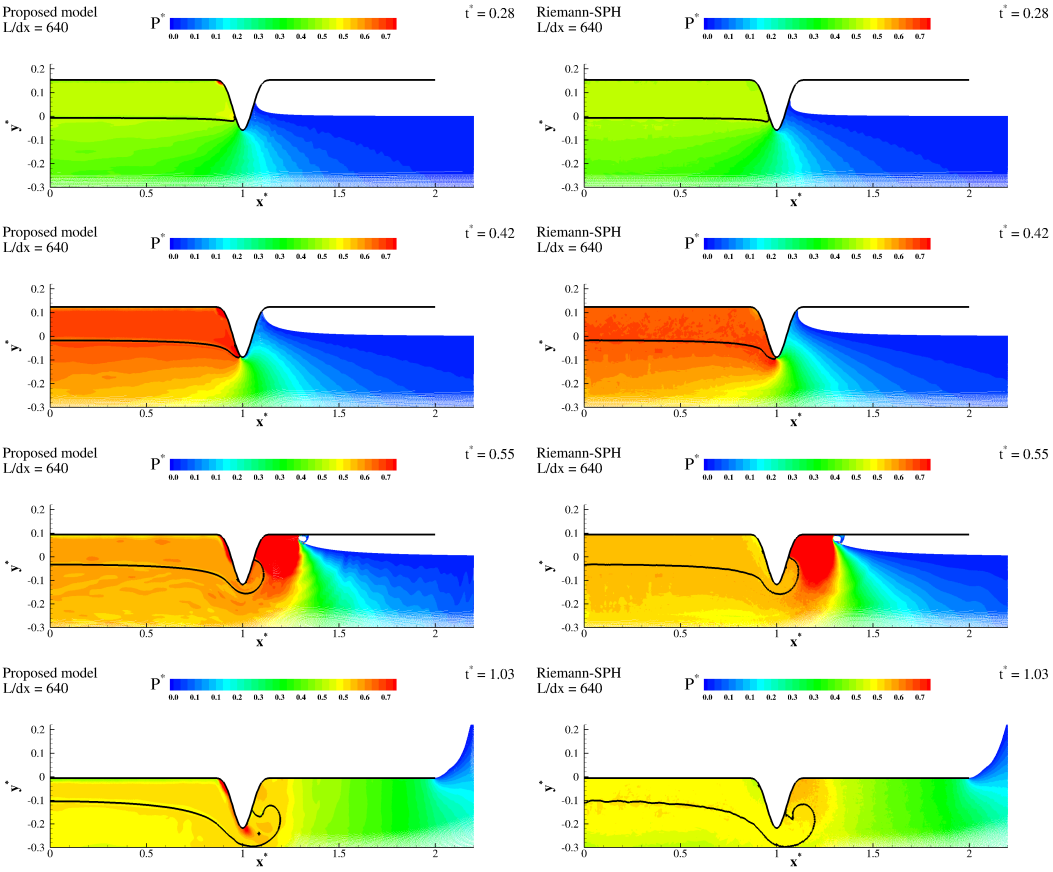

FIGURE 4.9: Fluid impact of a corrugated panel with entrapped gas cavity: comparison of the pressure field within the air and water phases yielded by the Multiphase δ-SPH scheme (left column) and the Riemann-SPH scheme (right column), during the impact stages at four different time instants $t^* = 0.28, 0.42, 0.55, 1.03$. The panel length is $c^* = 2$.

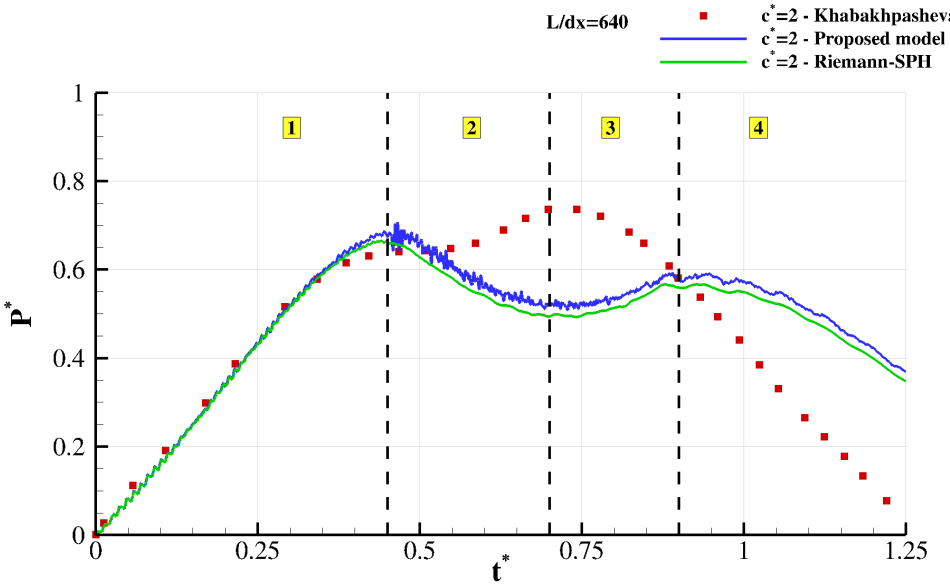

FIGURE 4.10: Fluid impact of a corrugated panel with entrapped gas cavity: comparison of the time evolutions of the pressure inside the entrapped air cavity predicted by the Multiphase δ-SPH (blue) and Riemann-SPH (green) schemes.

.

4.3 Summary of the comparison

In this chapter, the proposed Multiphase δ-SPH scheme was compared to the Riemann-SPH scheme in terms of stability, pressure field and mechanical energy decay. First, similarly to the Multiphase δ-SPH scheme in Section 2.4, the stability regions of the Riemann-SPH scheme was heuristically established in the multiphase framework through the 1-D Bagnold test case. It was found that the maximal stable CFL coefficients allowed by the Riemann-SPH scheme were far less sensible to the changes in density or sound speed ratios. It was also found that these maximal stable CFL values exceed the ones commonly used within the community (0.75 for δ-SPH and 0.375 for Riemann-SPH).

Secondly, a single-phase configuration of a dam-break test case was performed using the two models in order to compare their respective resulting pressure field and mechanical energy diffusion. Even in the absence of a particle shifting technique, the Multiphase δ-SPH scheme yields results that are very comparable to the Riemann-SPH scheme with particle shifting in terms of noise-free pressure and mechanical energy decay. Moreover, these satisfactory results come at a lower CPU cost (2.3 times less that the Riemann-SPH scheme for the highest resolution dam-break, using the same CFL coefficient for both models).

Finally, the complex multiphase case of the water impact of a corrugated panel on the water with entrapped air cavity was run using the Riemann-SPH scheme. Small oscillations were observed for the Multiphase δ-SPH

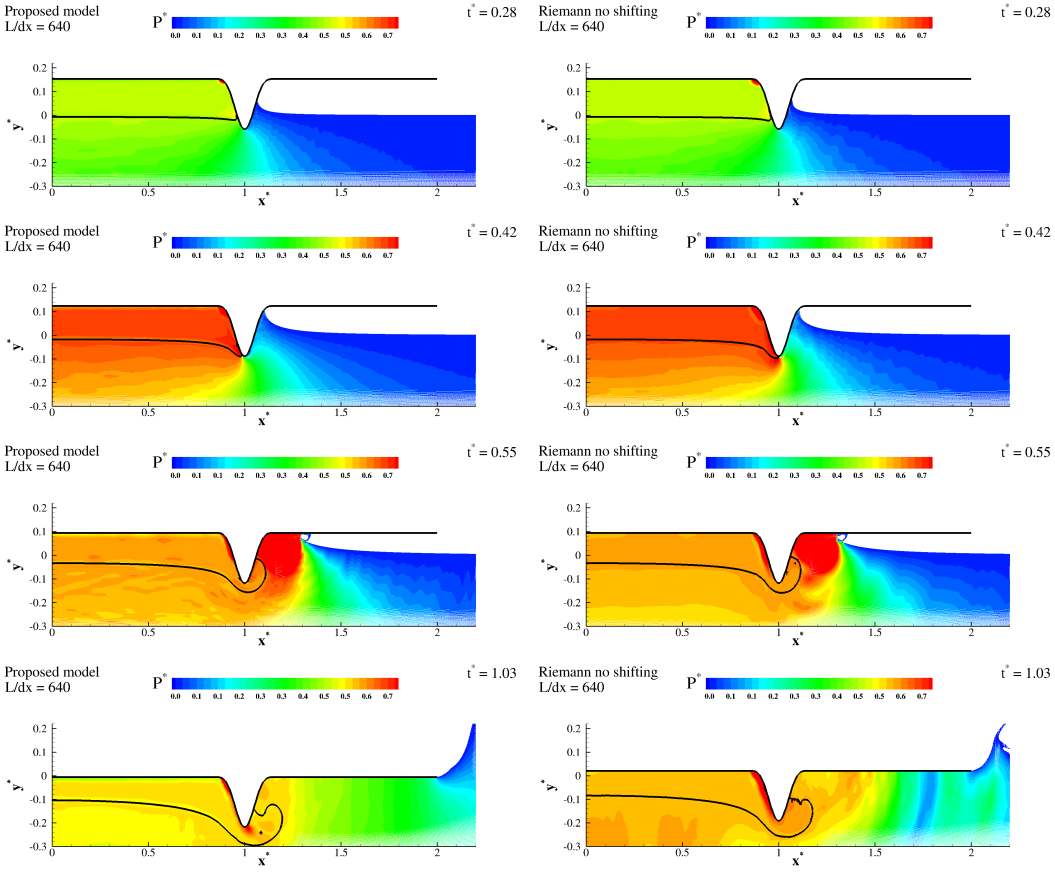

FIGURE 4.11: Fluid impact of a corrugated panel with entrapped gas cavity: comparison of the pressure field within the air and water phases yielded by the Multiphase δ-SPH scheme (left column) and the Riemann-SPH scheme (right column), during the impact stages at four different time instants $t^* = 0.28, 0.42, 0.55, 1.03$. The panel length is $c^* = 2$. The same overpressure at the round corners of the corrugation is observed for both the Multiphase δ-SPH scheme and the Riemann-SPH scheme without shifting.

scheme pressure which can easily be eliminated via a small increase in the viscous parameter α, while both models suffer from small errors near the corrugation corners in the absence of particle shifting. Nevertheless, both models seem to predict the same evolution of the contact points and of the pressure inside the air cavity, with no significant difference between the two models in terms of CPU costs, although the Riemann-SPH scheme with particle shifting allowed a higher CFL coefficient ($K_{Rie} = 0.6$ against $K_\delta = 0.25$).

Chapter 5

Numerical investigation of an aircraft ditching problem

Aircraft ditching poses many physical and numerical challenges over a wide variety of themes. Indeed, aircrafts should be properly designed to survive such an extremely dangerous landing process. In particular, it should be able to withstand huge loads during the emergency landing. Therefore, its kinematic and dynamic responses should be well studied through experimental and numerical investigations.

Full-scale aircraft impact tests have been performed in order to measure the pressure response [88, 89]. However, due the cost of such tests, usually scaled-model experiments are preferred [15], offering more possibilities in terms of the tested impact conditions.

These experimental investigations are generally complemented by a numerical approach. Indeed, the latter does not suffer from the classic limitations that hinder the experimental testing, such as repeatability and scaling issues.

In the context of the SARAH project, numerical investigations are carried out using advanced, coupled numerical methods called "high fidelity" models, which are suited for the treatment of non-linear hydrodynamics. These models are accurate but computationally costly compared to a "low fidelity" approach, which is based on analytical or semi-analytical methods for the simulation of water impacts. Classic examples of these can be found in [48, 103]. However, the hydrodynamic phenomena that occur during the ditching process are highly non-linear and coupled with the complex geometries of the aircraft structures, which greatly hinders the capabilities of the low fidelity models. However, the high fidelity approach can be used to calibrate the low fidelity models, which are faster but less accurate when not properly calibrated.

Recently, the SPH method has been identified as a good candidate for the numerical simulation of aircraft and helicopter ditching [107]. For this task it offers many advantages. It is mesh-free which avoids the problem of mesh distortion that challenges mesh-based methods such as the Finite Volume Method or the Finite Element Method which has been used for ditching investigation [99, 85]. Furthermore, contrary to ALE/FVM models [47, 104], it does not need any treatment to track or to capture the free-surface. In view of its advantages, the SPH method can also be coupled with the FEM in order to simulate aircraft ditching while taking also into account its structural

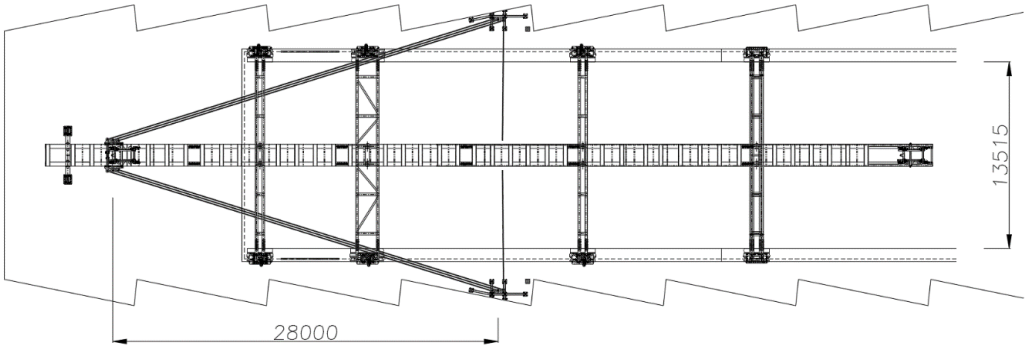

FIGURE 5.1: Top view of the CNR-INM High Speed Ditching Facility. The cords are V-shaped, and propel the specimen along the guide rails from left to right [44].

response [94, 36].

In this work, we are focusing on the response of rigid aircraft fuselages. The SPH method is used to numerically investigate the flow taking part in the rear part of a fuselage which should be the part of the aircraft that touches the water first, and compare the results with the findings of the experimental campaign led by Iafrati et al. (2019) [44] during the SARAH project. The first part of this chapter will present a recap of the experimental setup, including the instrumentation and the fuselage geometry. In the second part, the present numerical investigation is covered in detail, where the simulations results are confronted to their experimental counterpart.

5.1 The experimental setup

5.1.1 Instrumentation

Iafrati et al. [44] performed their tests within the High Speed Ditching Facility (HSDF) at CNR-INM in Rome, Italy (Fig. 5.1). The HSDF consists of a guide suspended over a water basin, at the opposite of a towing tank which is 470 m long, 13.5 m wide and 6.5 m deep. The guide enables vertical to horizontal velocity ratios (V/U) ranging from 0.03 to 0.05.

A set of elastic cords accelerate a trolley that brings the specimen and the acquisition box. The cords are attached to a U-shaped bar that pushes the trolley. The latter is left to move freely just before the impact via a braking system which acts on the cords. This way no external forces are acting on the trolley during the impact, apart from the hydrodynamic forces and the reaction of the guide. The pitch angle of the specimen can be varied from 4° to 10°. The maximum horizontal velocity U is 47 m/s.

The trolley is connected to the acquisition box (Fig. 5.2) that measures the loads exerted by the fluid in the horizontal and normal directions of the specimen referential. A total of 30 pressure probes are installed on the specimen as shown in Fig. 5.3. These are crucial for the numerical investigation as the pressure signals measured by these probes are the main results used

FIGURE 5.2: The trolley is attached to the guide. It carries the acquisition box and the tested specimen [44].

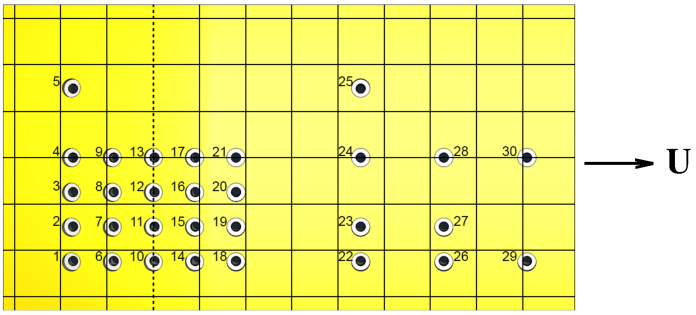

FIGURE 5.3: Location of the pressure probes on the tested specimen. Most of them are located in the rear part of the specimen, the trailing edge being to the left. The dashed line passes through the mid-line point that touches the water surface first at 8° pitch angle [44]. The arrow indicates the direction of U, the longitudinal speed of the specimen.

for the comparison. More details on the measurement tools used during the experimental campaign are available in [44].

Underwater visualizations are made possible through two high-speed cameras, which are synchronized with the pressure signal acquisition. One camera is located at the side in order to capture the impact velocity, and the other is located underwater deep enough to cover the entirety of the impact phase. The latter revealed the occurrence of cavitation/ventilation phenomena depending on the test speed. Fig. 5.4 shows underwater snapshots at the middle of impact at two different horizontal velocities, 21 m/s and 34.5 m/s. The prediction of these air or vapor cavities is one of the main targets of the present numerical investigation.

5.1.2 Fuselage geometry

The fuselage shapes, from which the full scale tested specimen are extracted, are described by analytical functions. The fuselages have a circular-elliptical

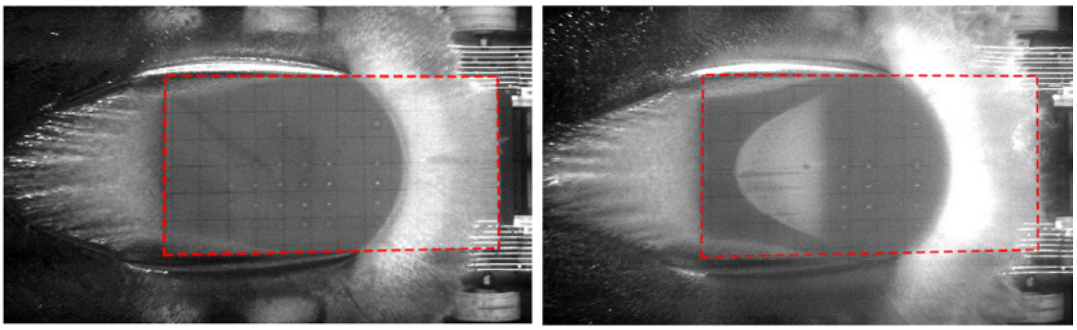

FIGURE 5.4: Snapshots of the underwater flow at two impact horizontal velocities: 21 m/s (left) and 34 m/s (right). The cavitation pocket is clearly visible at 34 m/s underneath the specimen (the latter is delimited by the red dashed lines [44]).

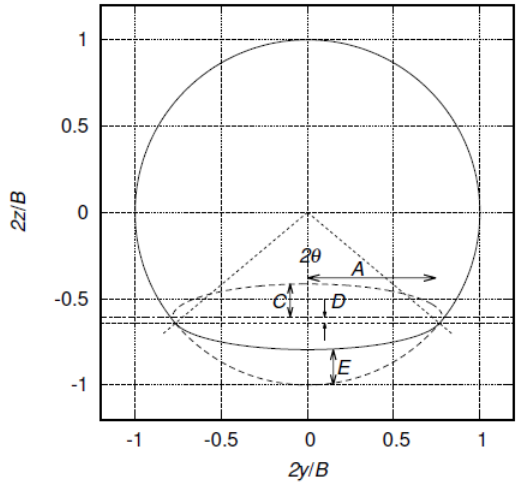

FIGURE 5.5: Circular-elliptical cross section of the fuselage [44].

cross section. As displayed in Fig. 5.5, two parameters define the non-dimensional cross section contour: the angle of tangency θ between the circle and the ellipse and the ratio C/D.

The ellipse semi-axes are given by:

$$A = \frac{C}{D}\frac{\sin\theta}{\sqrt{(\frac{C}{D})^2 - 1}}, \qquad C = \frac{A\tan\theta}{\sqrt{(\frac{C}{D})^2 - 1}} \tag{5.1}$$

with

$$E = 1 - \cos\theta - C\left(1 - \frac{D}{C}\right) \tag{5.2}$$

The dimensional equation of the ellipse is:

$$\left(\frac{y/r(x)}{A}\right)^2 + \left(\frac{z/r(x) + 1 - (E/C)}{C}\right)^2 = 1 \tag{5.3}$$

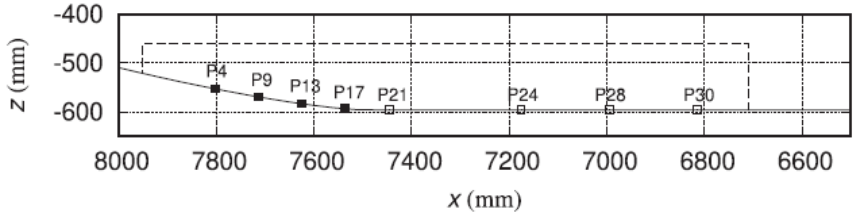

FIGURE 5.6: Longitudinal section of the specimen. The solid line is the bottom profile of the fuselage midline. The empty/full boxes represent the position of the front/rear pressure probes [44].

where $r(x)$ is the radius of the circular portion of the fuselage at the longitudinal position x, and the origin of the x axis is located at the fuselage bow ($x_I \leq x \leq x_E$ with $x_I = 6.71$ m and $x_E = 7.95$ m). The local radius is given by:

$$
\begin{aligned}
r(x) &= 0.5B\sqrt{1-\left(\frac{x-F_B.B}{F_B.B}\right)^2}, \qquad 0 < x < F_B.B \\
r(x) &= 0.5B, \qquad F_B.B < x < x_H \\
r(x) &= 0.5B + O(x), \qquad x_H < x < L_B.B
\end{aligned}
$$

where L_B, F_B and R_B are respectively the total, forward and rear portions lengths of the fuselage, all scaled by the fuselage breadth B. $x_H = B(L_B - R_B)$ is the rear end of the main fuselage. $O(x)$ is an offset function given by:

$$
O(x) = -\frac{B}{E}\sin\left(\frac{x-x_H}{K.R_B.B}\right)\left[\frac{x-x_H}{\sin(1/i)R_B.B}\right]^{1/i} \tag{5.4}
$$

The center of the cross section is located at $(x,0,0)$ for $0 < x < x_H$ and at $(x,0,-O(x))$ for $x_H < x < B.L_B$. For the considered shape, $L_B = 7.5$, $F_B = 1.5$, $R_B = 2.5$, $K = 1.55$, $i = 2.6$, $C/D = 5$, $\theta = 50°$ and $B = 1.5$ m. The fuselage portion used for the test is with $|y| \leq 0.33$ m. A view of the longitudinal section of the test specimen along with the probes of interest are shown in Fig. 5.6.

5.2 Numerical investigation

5.2.1 Proposed cavitation capturing technique

Cavitation is a phenomenon in which rapid changes of pressure in a liquid lead to the formation of vapor-filled cavities, in places where the pressure is sufficiently low. These cavities then collapse under higher pressures which generates intense shock waves.

Cavitation is usually an undesirable phenomenon that frequently occurs within industrial machinery, where it can cause massive wear, for example

the erosion of the surface of turbines and propellers. Lately, avoiding cavitation has been identified as an important factor for the design of ditching aircrafts [15]. The experiments of Iafrati et al. [44] showed the formation of cavitation pockets underneath the tested fuselage parts, with a strong dependence on the impact horizontal velocity. Therefore, one of the aims of the present study is to check whether it is possible to predict the occurrence of this phenomenon numerically.

Cavitation is inherently a multiphase problem where normally the liquid and vapor phases must be both modeled. However, the density ratio between liquid and cavitation water vapor is about 80000, which is too high a value for any state-of-the-art SPH multiphase model. In a first attempt, in the present work, it is assumed that the cavitation problem is in fact a single-phase phenomenon, which could be captured through the following proposed technique.

Physically speaking, cavitation will only occur if the local pressure declines to some point below the saturated vapor pressure of the liquid, noted P_{sat}. The water temperature during the ditching experiments is between 18° and 21° [44], which corresponds to a saturated vapor absolute pressure ranging between 2.0 kPa and 2.7 kPa, corresponding to relative values of ΔP_{sat} between -99.3 kPa and -98.6 kPa ($P_{atm} = 101.3$ kPa).

The proposed cavitation capturing technique works as follows. The pressure P is compared at each time step to a set value of ΔP_{sat}, and is reset to $P_{sat}^{SPH} = \Delta P_{sat}$ if $P < \Delta P_{sat}$. In that case, the density is reset to:

$$\rho_{sat} = \rho_0 \left(1 + \frac{P_{sat}^{SPH}}{B}\right)^{-\gamma}, \qquad B = \frac{\rho_0 c_0^2}{\gamma} \tag{5.5}$$

in order to maintain the use of the equation of state (1.4) linking the density and the pressure.

Although this pressure manipulation is not physical, it at least guarantees maintaining the cavitation pressure level in the zone of interest. However, it poses the problem of not respecting the real mass of the cavitation pocket. With our technique, the cavitating particles still belong to the liquid water phase instead of a water vapor phase, whose density is many orders of magnitude smaller. Therefore, a potential numerical cavitation pocket will be naturally heavier than in reality.

5.2.2 2D configuration

5.2.2.1 Numerical setup

The effect of the horizontal velocity on the pressure and the loading on the specimens is investigated in this section. The chosen pitch angle for the comparisons is 6°. The vertical to horizontal velocity ratio V/U is taken equal to 0.0375. The underwater camera in [44] highlighted the occurrence of cavitation starting from the impact speed $U = 30.6$ m/s. Therefore, in this work two horizontal speeds are simulated, 21 m/s and 34 m/s, without and with expected cavitation occurrence respectively.

For these simulations and similarly to the corrugated flat panel impact of Section 3.4, the adopted numerical sound speed in the water is based on the expected maximal pressure, recorded for each horizontal velocity. For the impact speed $U = 21$ m/s, the highest experimental pressure value is $P_{max}^{exp} \approx 462$ kPa, while in the case of 34.5 m/s, the highest pressure value was $P_{max}^{exp} \approx 1260$ kPa [44].

As explained in Section 1.3.1, in order to guarantee the weakly-compressible regime, the maximal numerical Mach number reached within our SPH simulations is $Ma = U/c_0 = 0.1$. Formula (2.65) is once again used in order to determine the numerical sound speed in the water based on the maximal experimental pressure. Therefore, the water sound speed is set to $c_0 = 215$ m/s for $U = 21$ m/s and $c_0 = 355$ m/s for $U = 34.5$ m/s.

Starting from these sound speed values, the domain size was taken large enough so as to avoid the reflection of acoustic waves on the domain boundaries. The numerical tank is 20 m long, 4 m wide and 6 m deep. Besides, the simulations have been conducted using the Adaptive Particle Refinement (APR) technique described in Section 1.6.2.2, which allows to keep a high spatial resolution around the fuselage part and a coarse discretization elsewhere during the simulation. Indeed, the APR boxes are first initialized around the fuselage part, then are made to follow its kinematics throughout the water impact simulation.

Today the APR technique is developed solely for Riemann-SPH type schemes in our lab. Consequently, instead of the Multiphase δ-SPH scheme, throughout this study the Riemann-SPH scheme presented in Section 2.1.4 is used. Furthermore, the boundary integral method based on a Cut-Face Approach (CFA, *cf.* Chiron et al. [13]) presented in Section 1.5.1.2 is exclusively used for the imposition of the solid boundary conditions (tank and fuselage) due to its ability to handle complex wall geometries.

In any case, a good calibration of the refinement boxes is crucial for the simulations, in the sense that a fine enough discretization level must be achieved without making the computation time prohibitive. Also, the refinement boxes must be soundly placed in order to capture the main investigated physics, which are the pressure/loads on the fuselage, and the possible occurrence of cavitation in the water underneath the rear part of the specimen.

Consequently, a 2D study is perfect for this kind of calibration, through which the placement and numbers of refinement boxes can be optimized, and a convergence study can be made in order to determine the minimal acceptable discretization ratio, with faster CPU times compared to the 3D case.

In order to obtain the 2D configuration, the 3D domain and the fuselage geometry are both sliced through the $y = 0$ plane. Following [64], the 2D computations were run using two discretization levels, $\Delta x_{min} = 3$ mm and $\Delta x_{min} = 0.39$ mm, both with seven refinement boxes.

As pictured in Fig. 5.6, the pressure probes of interest (P4, P9, P13, P17, P21, P24, P28 and P30) are all located on the piercing edge (middle line of the bottom surface) of the tested specimens. Fig. 5.7 shows the equivalent numerical setup of the 2D fuselage (plane XZ cutting the piercing edge). The

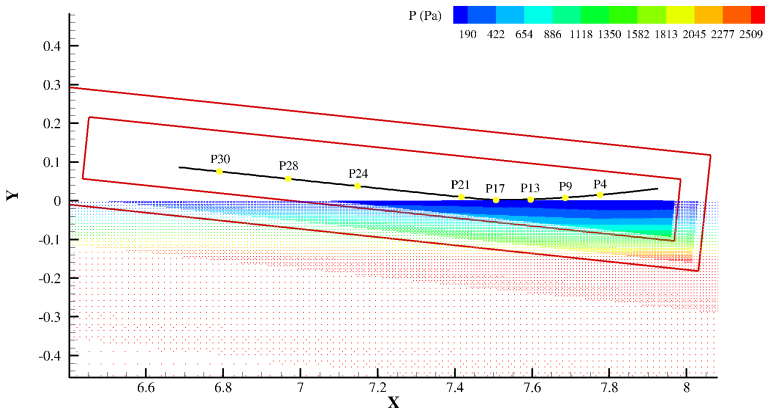

FIGURE 5.7: 2D ditching: zoom on the profile and the nearby refinement boxes. The APR boxes (in red solid lines) are rotated to follow the pitch angle of the profile. The yellow circles depict the pressure probes of interest. For the sake of clarity, only the refinement boxes corresponding to the two highest refinement levels are shown.

refinement boxes were positioned so as to follow the pitch angle of the fuselage. The choice of angling the refinement boxes is made in order to offer the finest discretization level in the jet root zone, which is crucial for the computation of the local impact pressures.

The configuration shown in Fig. 5.7 ensures that the refinement boxes completely envelop the profile, so that it offers the finest resolution in the rear water zone just underneath the fuselage, where the targeted cavitation phenomenon is expected to occur (rear probes P17 to P4). The number of particles at the start of the simulations is 201844.

5.2.2.2 U=21 m/s - Results and comparison

First, the ditching behavior of the 2D profile is shown in Fig. 5.8 at different time instants, for the impact speed $U = 21$ m/s. Similarly to the classic case of a wedge impact [61, 109, 50], a high pressure zone is formed at the water jet root, and continues to move along the specimen as it enters the free-surface. The jet is very thin and follows the trajectory of the profile, which confirms the choice of angling the highest resolution APR box.

Fig. 5.9 shows the 2D SPH pressure signals registered by the probes P17, P21, P24 and P28 for the coarse and fine resolutions, in comparison with the experimental results of Iafrati et al. [44]. The pressure signals were all shifted in time so as to make the experimental and numerical pressure peaks P17 coincide.

The SPH pressure peaks are quicker to appear compared to the experiments. This is explained by the fact that the 2D jet has less degrees of freedom than in a 3D configuration, which means that it will be confined and forced to move following the direction of the profile. Nevertheless, the jet propagation

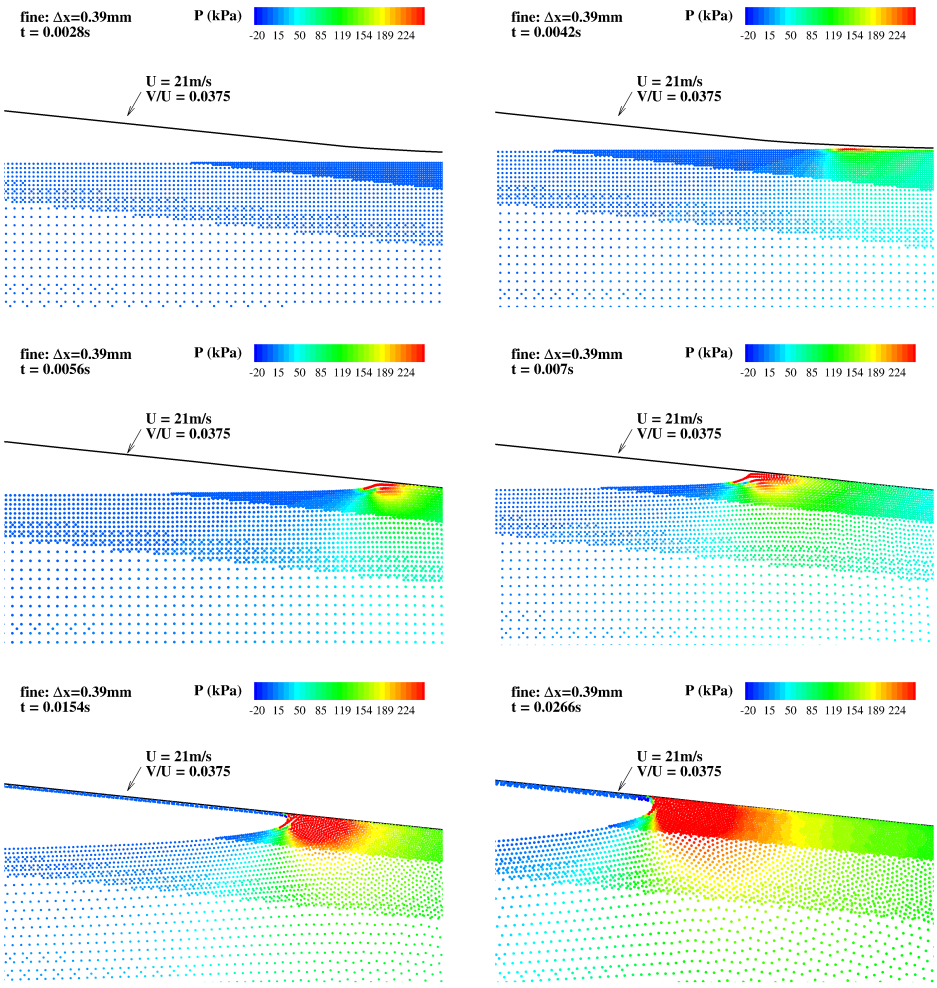

FIGURE 5.8: 2D ditching: zoom on the high pressure zone at the water jet root.

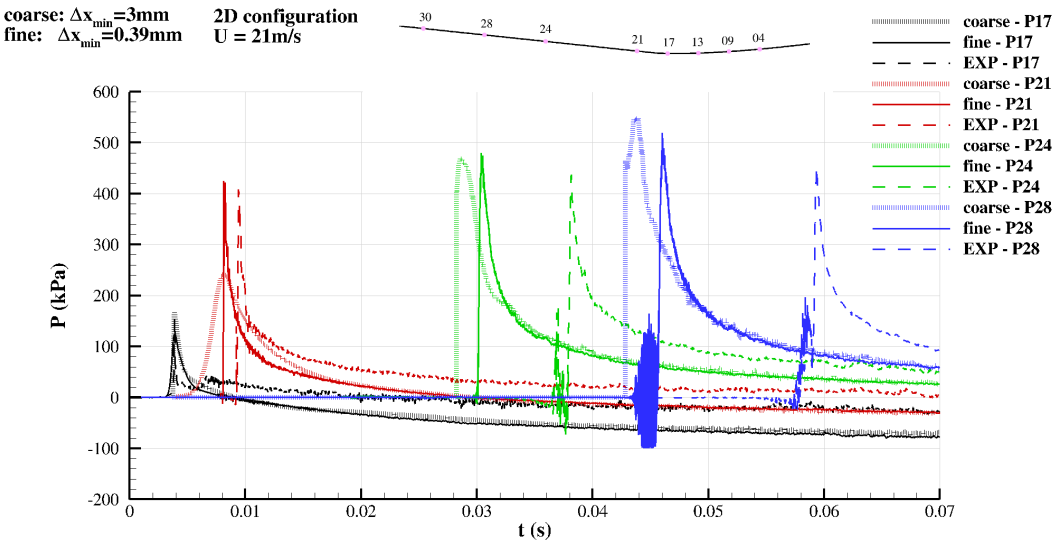

FIGURE 5.9: 2D ditching: experimental vs numerical pressure signals registered by the probes P17, P21, P24 and P28 with the coarse and fine resolutions, for the impact speed $U = 21$ m/s.

speed is relatively closer to the experiments when using the finer discretization. The SPH solutions also seem to slightly over-predict the pressure amplitudes. This is expected since the 3D effects occurring in the experiments will tend to lower maximal pressures, due to the flow evacuation through the sides of the specimen. The simulation with the fine resolution yields the closest results to the experiments at all the pressure probes. On the other hand, as expected the coarse simulation yields less accurate pressure signals especially at the early stages of the simulation, where the impact regions are still under-resolved.

Both the experimental and SPH results register high-frequency fluctuations of pressure which are captured by the probes P24 and P28, as seen in Fig. 5.10. Those are due to fragmented jet of water that hovers over the numerical probes, and to the general chaotic behavior at the water free-surface that follows the impact of the specimen in the experiments. Another reason behind these oscillations is the choice of the sound speed of water which does not take into account the weakly-compressible assumption inside the jet, since it is based on the maximal registered experimental pressure, regardless of the maximal jet sped. Indeed, the magnitude of velocity in the jet on the probe P28 at $t = 0.0448$ s is around 60 m/s (Fig. 5.10) corresponding to a Mach number of 0.28, which is beyond the weak-compressibility limit. Also, note that the Cut-Face-based boundary integral approach (CFA) [13] used for our ditching simulations was developed for the weakly-compressible regime, the absence of which could damage the accuracy of the predicted pressure field, as observed here. This point should be further investigated in the future.

More importantly, for this impact speed the 2D SPH pressures registered by the probes P17-P9, located at the rear part of the profile, do not reach the water saturation pressure, as seen in Fig. 5.11. This effectively means

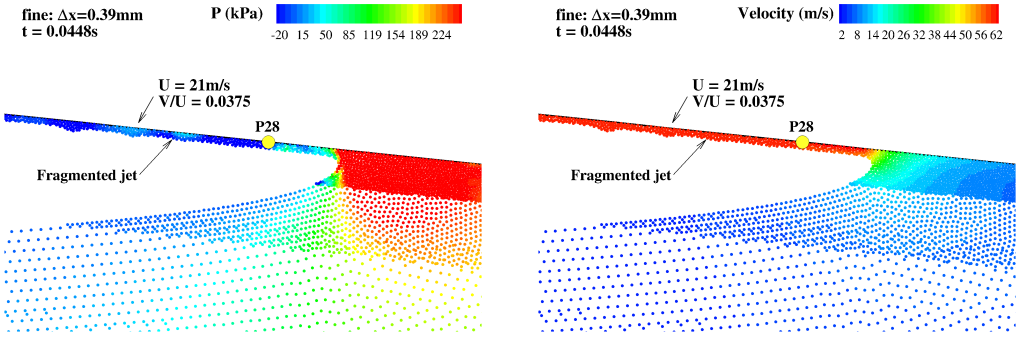

FIGURE 5.10: 2D ditching: pressure oscillations (left) and velocity (right) within the fragmented jet, captured by the probe P28.

that both the SPH and experiments agree on the fact that the cavitation phenomenon does not appear at this impact speed, even though the SPH computations predict lower values of pressure. Note that the numerical pressures in this zone are negative, which means that an air suction phenomenon would probably have occurred had an air phase been modeled within our simulations. Thus, the discrepancy between the experimental/numerical pressure signals could be caused by the absence of the air phase in the current numerical configuration, and by the fact that the experiments are not 2D but 3D.

In the next section, the same numerical 2D configuration is kept, but with a higher impact speed of $U = 34.5$ m/s, which according to the experiments of Iafrati et al. [44], is enough to induce cavitation within the water.

5.2.2.3 U=34.5 m/s - Results and comparison

The time evolution of the pressure registered by the front probes is shown in Fig. 5.12. Similarly to the previous impact speed, the pressure peaks are still over-predicted by our SPH method in terms of amplitude and propagation speed along the edge of the profile, with the finer resolution yielded slightly more accurate results in comparison to the experimental curves of Iafrati et al. [44].

Fig. 5.13 plots the time evolution of the pressure signals captured by the rear probes P17-P4, for the impact speed $U = 34.5$ m/s in the 2D configuration. Contrary to the previous impact speed, here the SPH registered pressures at the rear of the profile do reach the saturation pressure level, and stagnate at this value thanks to the proposed cavitation capturing technique presented in Section 5.2.1.

However, it is important to note once again the significant discrepancy between the experimental and numerical negative pressures captured at the rear probes P17-P4. A close inspection of the underwater snapshots of the experimental flow reveals the existence of bubbly flow on the rear edges of the specimens, as can be observed in Fig. 5.4 for both impact speeds U=21 m/s and U=34.5 m/s. These highly three-dimensional bubbly flows result from

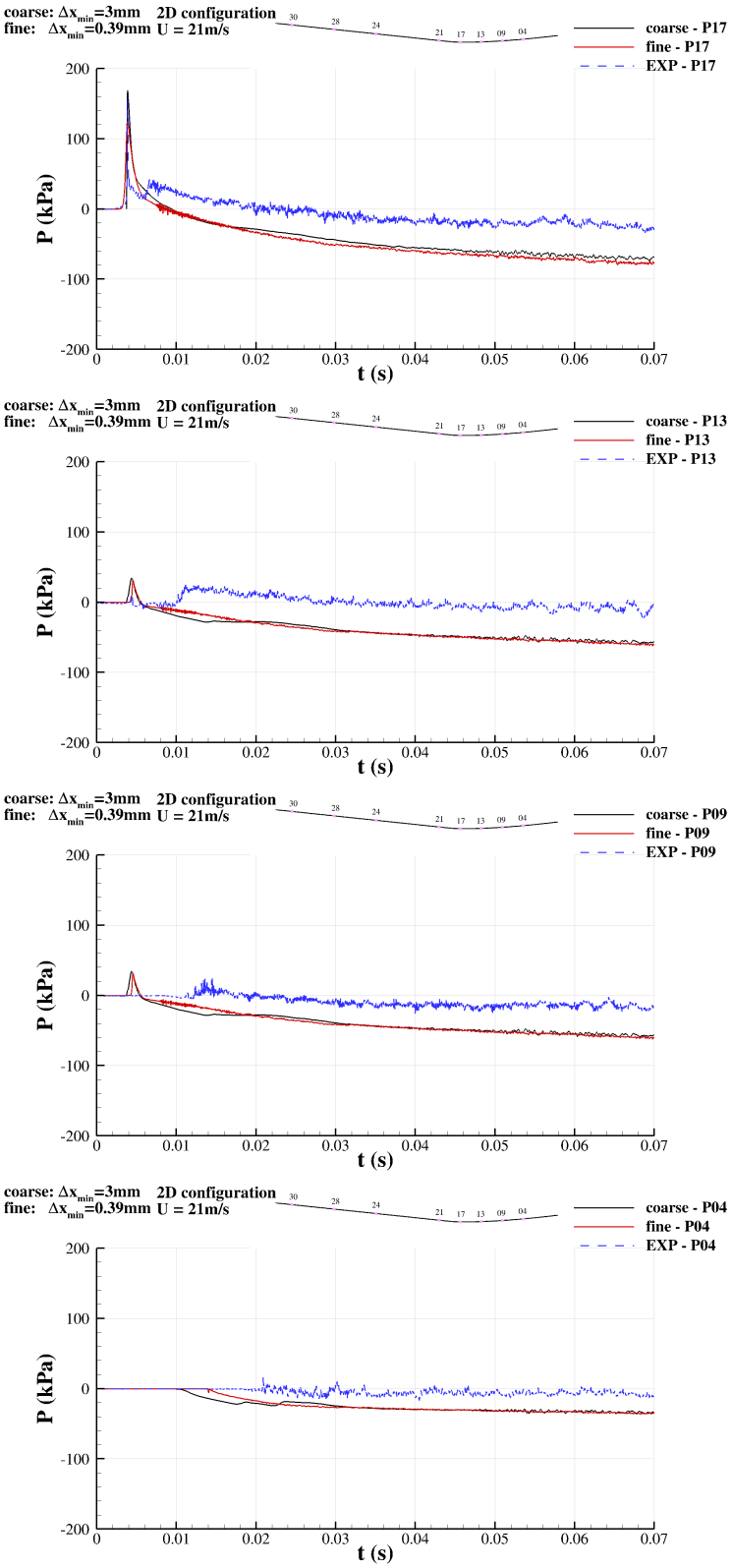

FIGURE 5.11: 2D ditching: experimental vs numerical pressure signals registered by the rear probes P17-P4 with the coarse and fine resolutions, for the impact speed $U = 21$ m/s. The experimental and SPH results agree on the absence of cavitation.

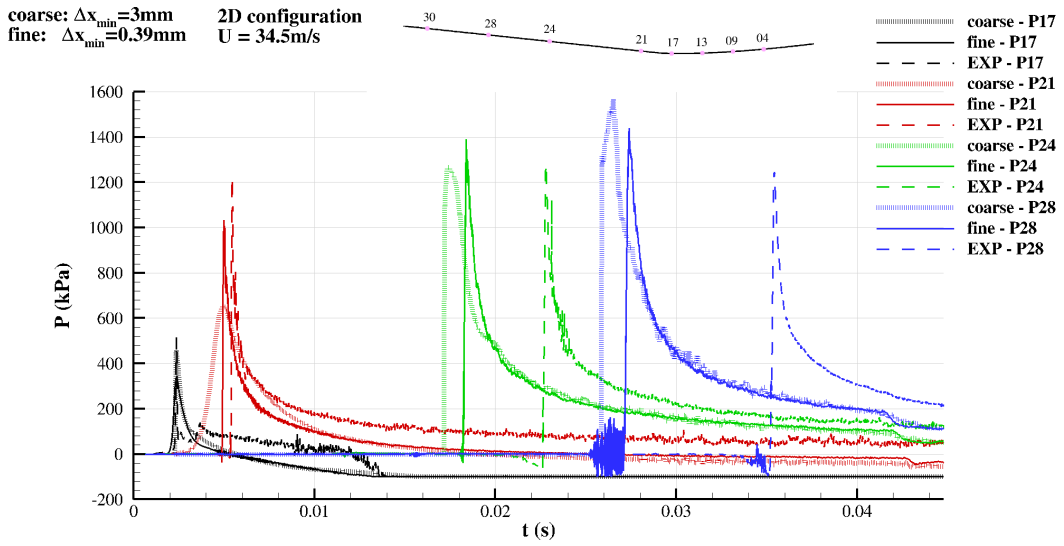

FIGURE 5.12: 2D ditching: experimental vs numerical pressure signals registered by the probes P17-P28 with the coarse and fine resolutions, for the impact speed $U = 34.5$ m/s.

the mixing of air bubbles with the water upon the fuselage impact. Obviously, these are 3-D multiphase phenomena that cannot be captured in a 2D single-phase configuration. Consequently, important numerical inaccuracies should be expected in this region of the flow, especially in terms of the predicted numerical pressure in the rear portion of the fuselage.

Nevertheless, this initial 2-D approach effectively proved that the SPH method can predict the occurrence of cavitation at this impact speed, in accordance with the experiments. Moreover, the implementation of the cavitation technique does not seem to introduce any numerical instabilities within the flow. A snapshot of the flow at $t = 0.0392$ s is provided in Fig. 5.14. Indeed, underneath the rear portion of the fuselage the cavitation zone is highlighted in red solid lines, wherein the particle pressures which reach the prescribed saturation vapor value are blocked at this value. In this zone and elsewhere in the water, the pressure is highly regular without any numerical noise. This particular result is very encouraging for the extension to 3D.

5.2.3 3D study

5.2.3.1 Numerical setup

The sound speed values used for the 2D configuration were kept unchanged for the 3D simulations. However, the passage from 2D to 3D configurations poses some difficulties in terms of CPU cost. A good compromise between particle refinement levels and CPU cost had to be achieved. The simulations were run using a coarser discretization, $\Delta x_{min} = 3.125$ mm, using 6 refinement boxes, inclined at the fuselage pitch angle similarly to the 2D configuration. Fig. 5.15 shows a global view of the numerical domain, including the APR boxes and the fuselage portion. The latter was implemented following

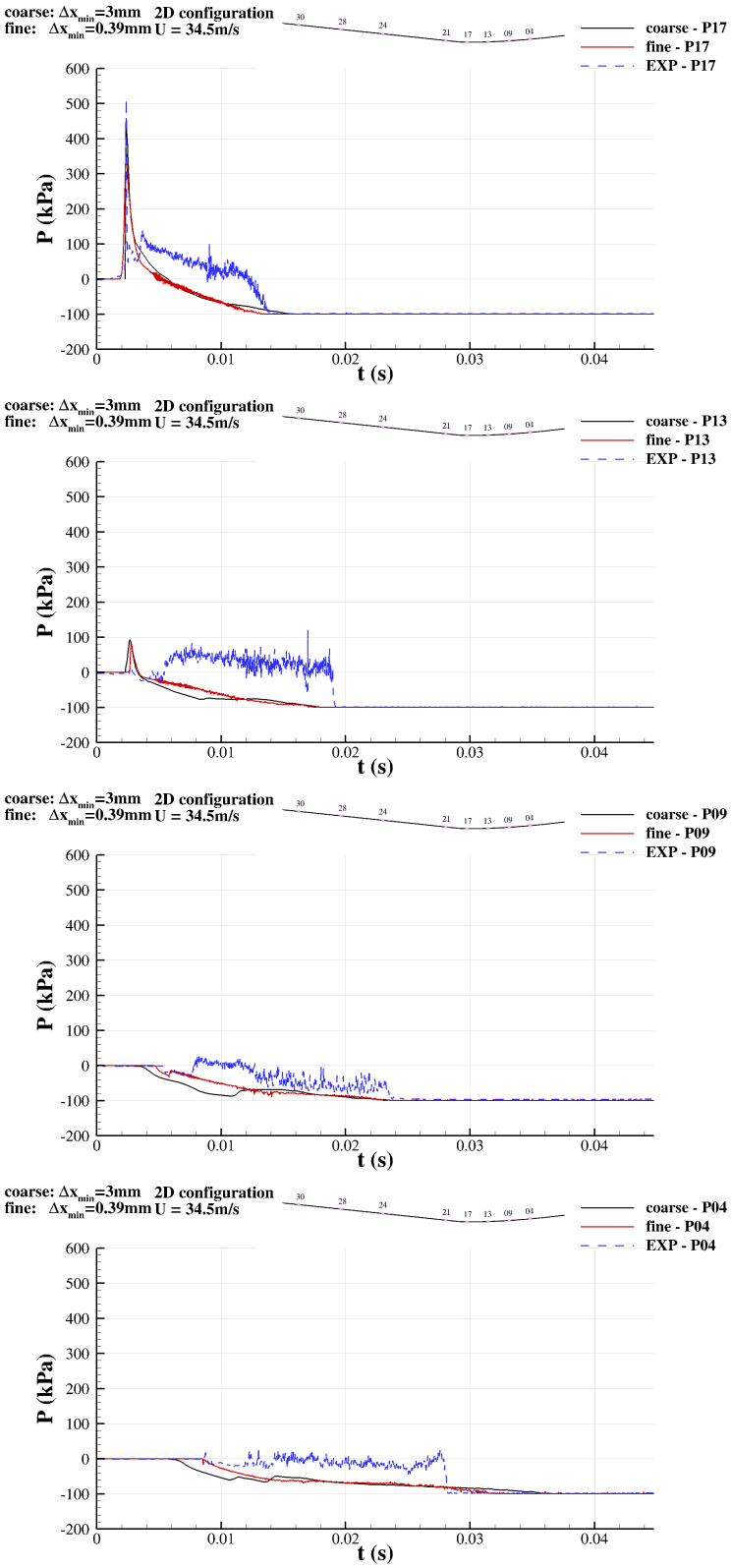

FIGURE 5.13: 2D ditching: experimental vs numerical pressure signals registered by the rear probes P17-P4 with the coarse and fine resolutions, for the impact speed $U = 34.5$ m/s. This time the predicted pressure reaches the water saturation level, which means that cavitation does occur in this zone.

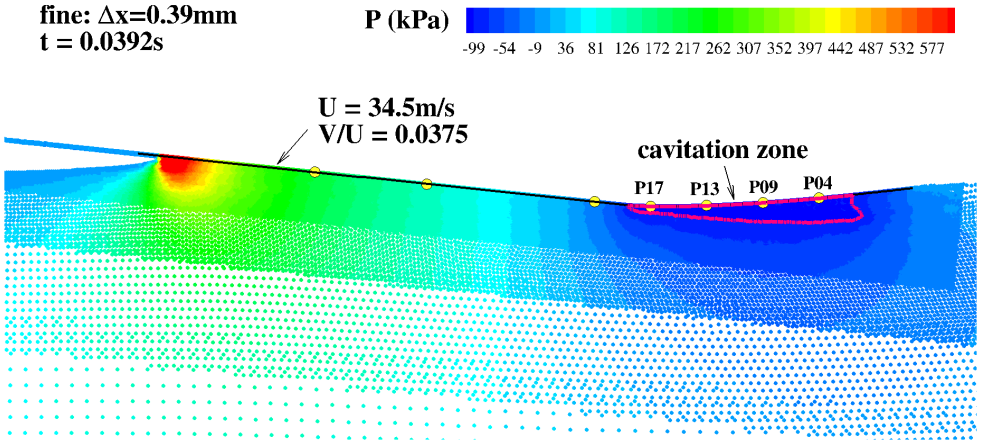

FIGURE 5.14: 2D ditching: snapshot of the flow at $t = 0.0392$ s. The cavitation occurs in the water zone underneath the rear of the profile, where the probes P17-P4 are located. The cavitation zone contour is highlighted with a solid red line.

the analytical function provided by Iafrati et al. [44] and presented in Section 5.1.2.

5.2.3.2 U=21 m/s - Results and comparison

The evolution of the water surface deformations during the fuselage impact is shown in Fig. 5.16 at different time instants. The pressure maps on the fuselage are also presented in Fig. 5.17 at the corresponding time instants.

At the front part of the specimen, a parabolic-shaped jet is developed starting from the region of curvature change. Similarly to the 2D simulations, the jet keeps advancing towards the leading edge of the fuselage part at a constant maximal pressure while it keeps penetrating the water.

Contrary to the 2D configuration however, the 3D jet propagation speed computed with the SPH method is much closer to the jet propagation speed of the experiments. This also was expected since the confinement is higher is 2D, inducing faster outflow around the specimen. This result is clear on Fig. 5.18, where the histories of the numerical and experimental pressure signals captured by the probes P17-P30 are plotted. On the one hand, although a small time shift still exists between the SPH and experimental pressure peaks, the 3D numerical signals are very close to the experimental results. The origin of the slight time shift can be attributed to the fact that particle resolution is still not fine enough, and also to the absence of the air phase within our computations.

On the other hand, the discrepancy of pressure amplitude is still observed for the probes P17 and P21, which is explained by the fact that at these early ditching stages the corresponding impact zones are under-resolved, similarly to the 2-D simulation with the same discretization level $\Delta x_{min} = 3$ mm. Nonetheless, later in time numerical pressure peaks are in very satisfactory agreement with the experiments (P24, P28 and P30).

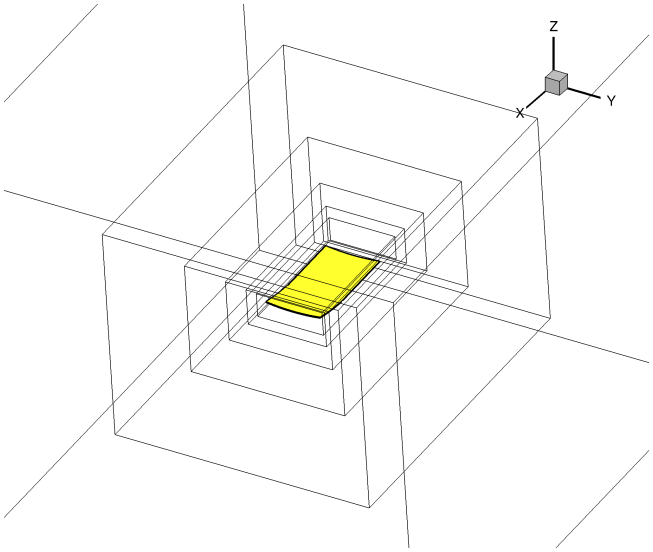

FIGURE 5.15: 3D ditching: numerical domain used for the simulations. The panel is highlighted in yellow. The boxes represent the different APR resolution levels.

As visible in Fig. 5.17, the water impact of the fuselage also generates negative pressures underneath its rear, due to its double curved geometry [44]. At the impact speed U=21 m/s, underneath the curvature change zone the numerical pressure reaches its lowest values without reaching the pressure saturation level, as predicted in the experiments.

Fig. 5.19 shows the time evolution of the pressure signals registered by the rear probes P17-P4. The SPH model predicts lower negative pressure values in this zone especially at the probes P17 and P13, which is again linked to the absence of air in our simulations.

5.2.3.3 U=34.5 m/s - Results and comparison

The SPH results for the impact speed U=34.5 m/s are presented in this section. The time histories of the signals on the probes P17, P21, P24, P28 and P30 are shown in Fig. 5.20. Similarly to the previous impact speed, the numerical and experimental pressure peaks agree in terms of both the amplitudes and propagation velocities.

The pressure signal captured by the probe P17 decreases to the set value of the vapor pressure of water and stagnates at this value throughout the duration of the simulations. This behavior is observed also at the rear probes P13-P4, as shown in Fig. 5.21. This is a clear indication that the water pressure in this zone has reached the cavitation threshold. Note that the experiments predict a pre-cavitation phase where the pressure oscillates, which is not predicted by our single-phase SPH model. Essentially though, the experiments and the numerical results agree on the time the pressure reaches the cavitation after the peak is registered at the probe P17.

The pressure map evolution on the fuselage is provided in Fig. 5.22 at different time instants. As expected, the pressure reaches higher levels when

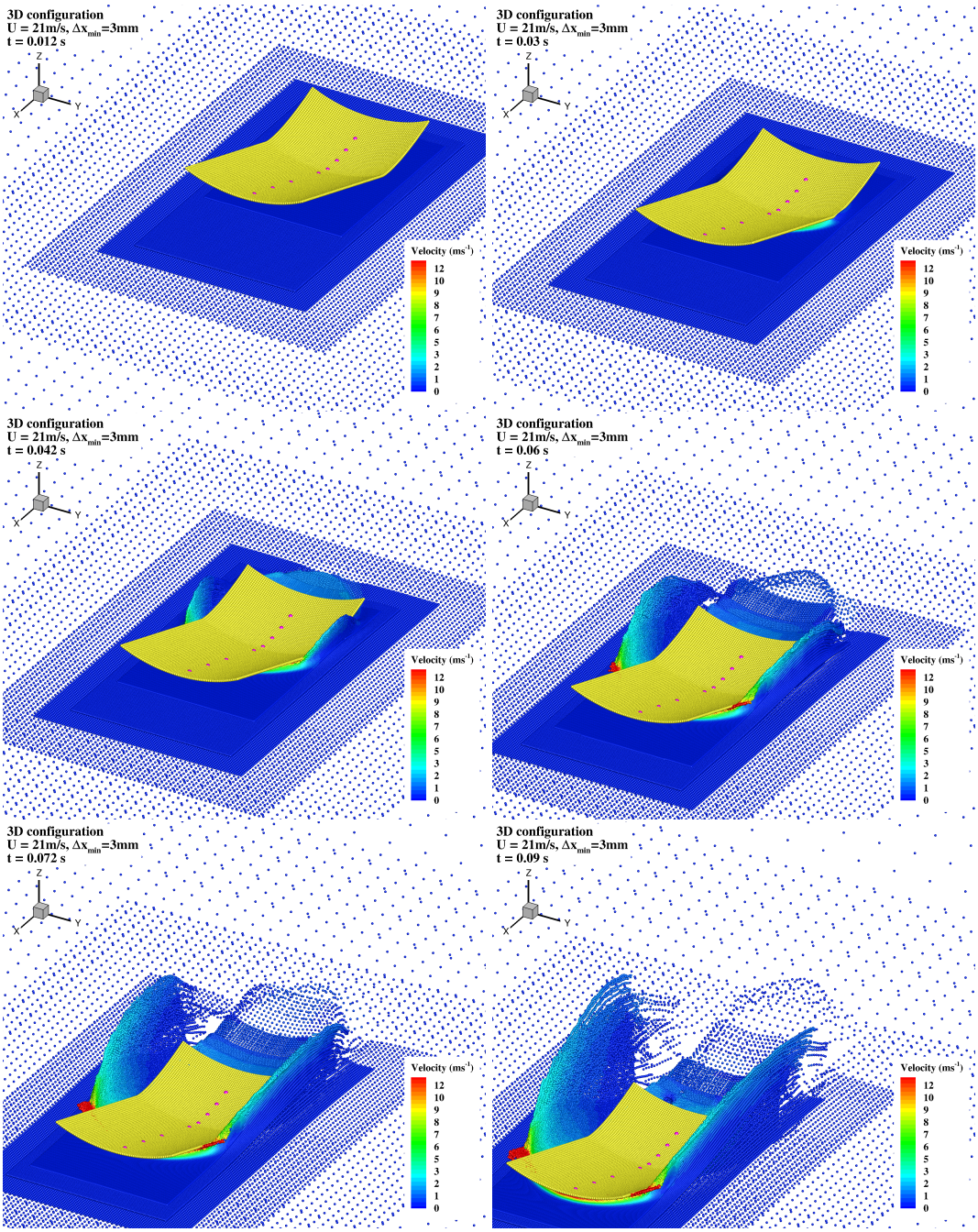

FIGURE 5.16: 3D ditching: evolution of the water free-surface during the fuselage impact at U=21 m/s. The probes of interest are highlighted in purple. They are located on the piercing edge (mid-line) of the fuselage.

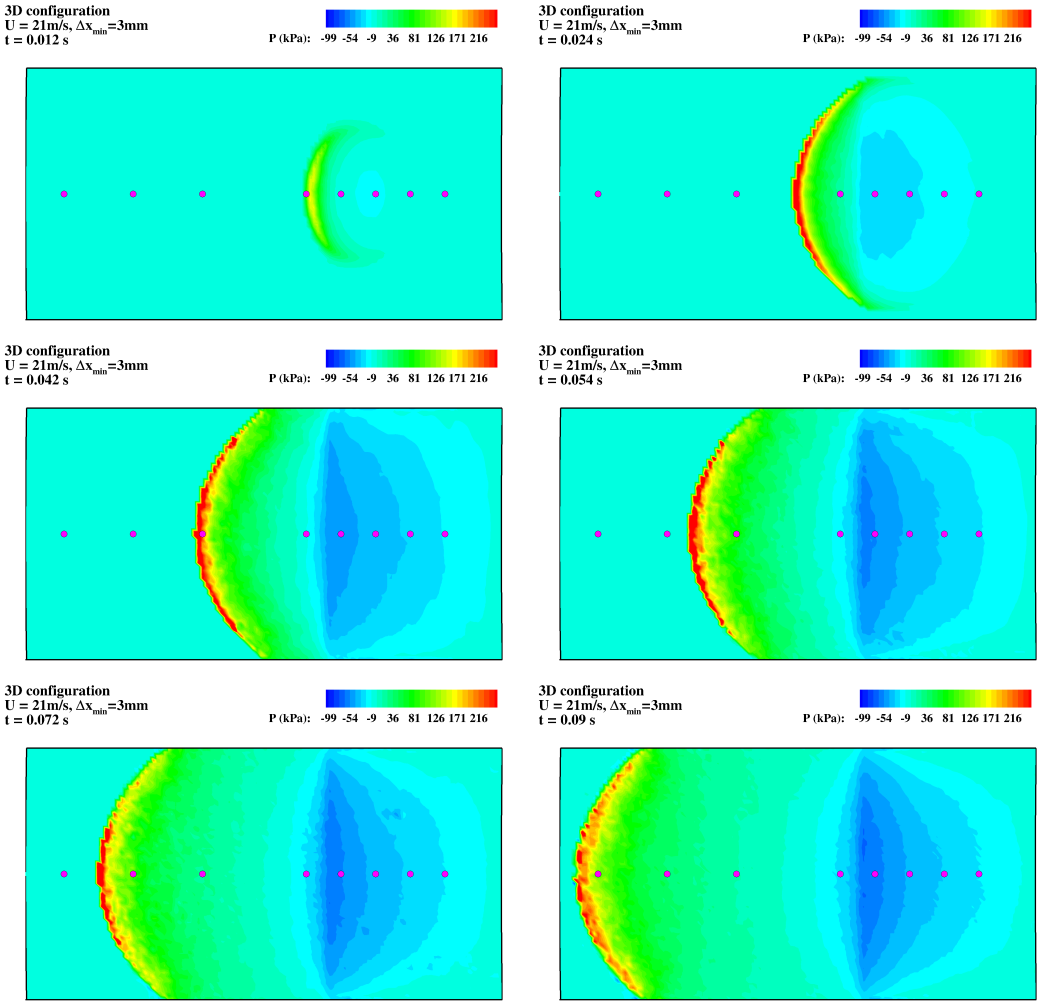

FIGURE 5.17: 3D ditching: evolution of the pressure map on the fuselage impacting at U=21 m/s. As expected, the pressure does not reach the pressure saturation level at this impact speed.

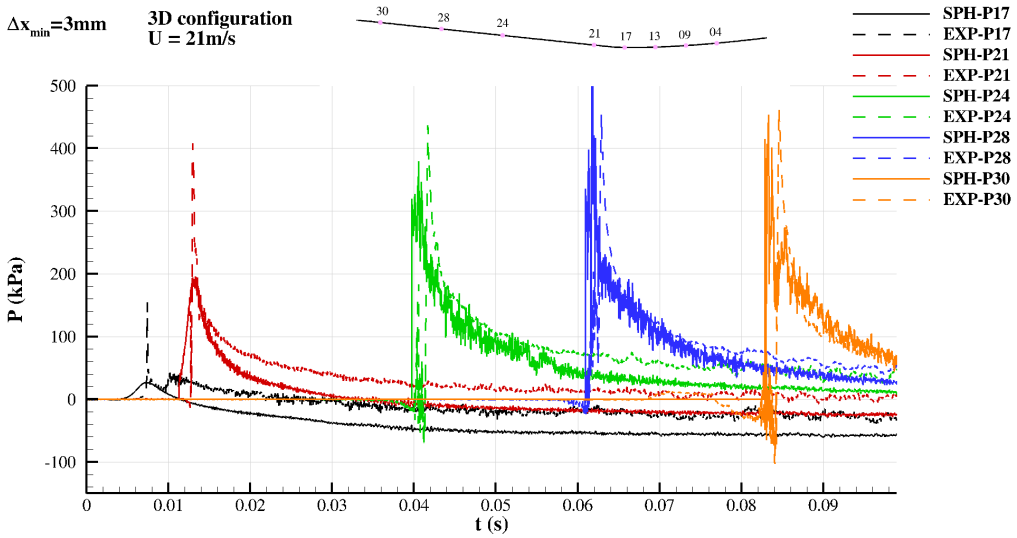

FIGURE 5.18: 3D ditching: experimental vs numerical pressure signals recorded at the probes P17-P30, at the impact speed U=21 m/s.

increasing the impact speed from 21 m/s to 34.5 m/s. More importantly, the cavitation zone is clearly visible at the rear of the profile. Side and front view of the cavitation pocket are provided in Fig. 5.23, where the particles of higher pressure than the pressure saturation level are blanked.

A qualitative comparison of the cavitation pocket shape is provided in Fig. 5.24, which shows a bottom view of the experimental and numerical flows. Although the instant of the experimental snapshot is unclear, a clear resemblance in the shape of the cavitation pocket between our numerical result and the experiments is visible, with only a slight difference in size in the longitudinal and transversal directions. This discrepancy could be attributed again to the particle resolution still not being fine enough at $\Delta x_{min} = 3$ mm, and to the fact that the cavitation is assumed here to be a single-phase phenomenon, without a proper modeling of the water vapor and surrounding air phases. In any case, it is somewhat surprising that the proposed cavitation capturing technique does not introduce any numerical instabilities within the flow, as the computed pressures can be considered to be in very good agreement with the results of the experimental campaign of Iafrati et al.[44].

5.3 Summary of the numerical campaign

In the context of the SARAH project, a numerical investigation of an aircraft fuselage ditching was carried out in this chapter, using a weakly-compressible Riemann-SPH method. The effect of viscosity was not taken into account as it is considered negligible compared to the effects of pressure and inertia which are largely dominating in the high-speed impacts studied here.

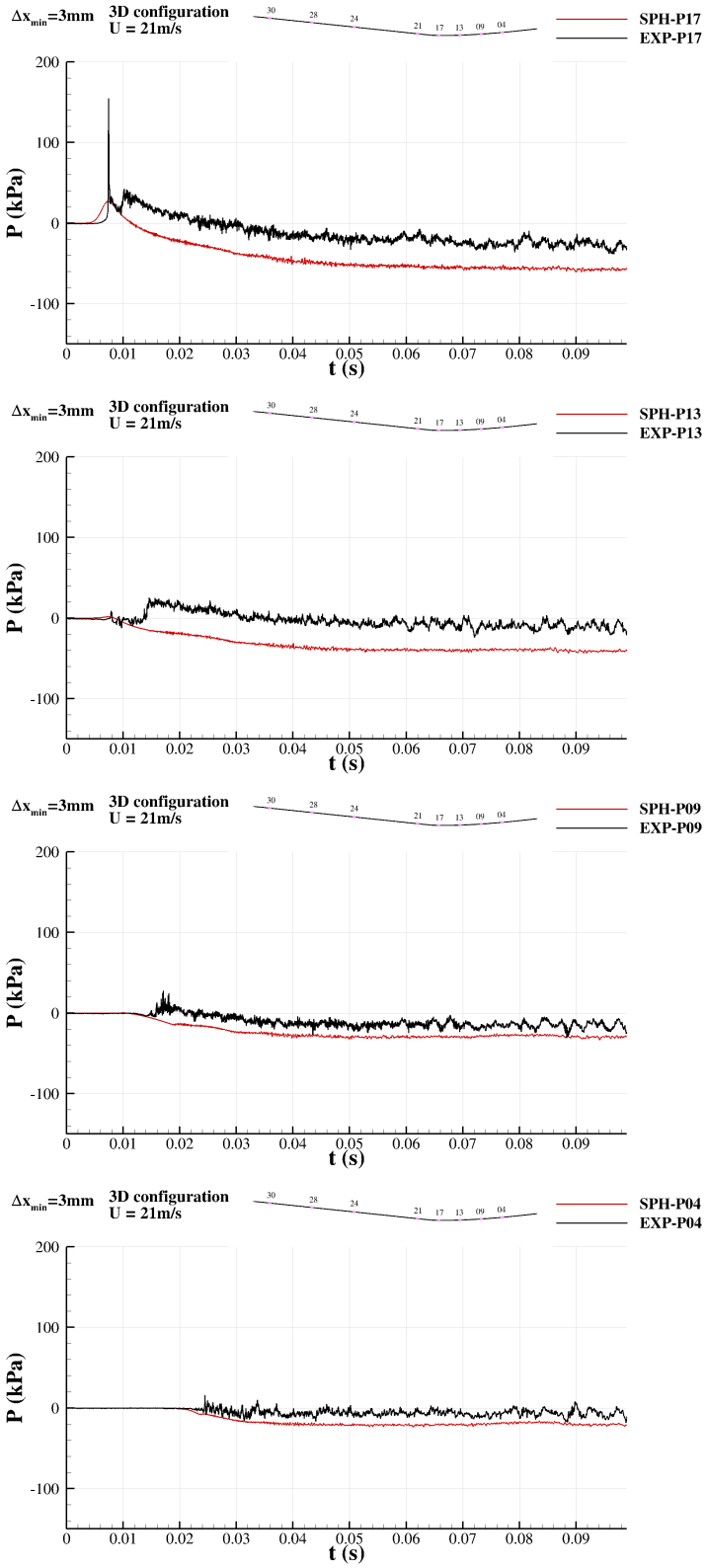

FIGURE 5.19: 3D ditching: experimental vs numerical pressure signals registered by the rear probes P17-P4, at the impact speed U=21 m/s.

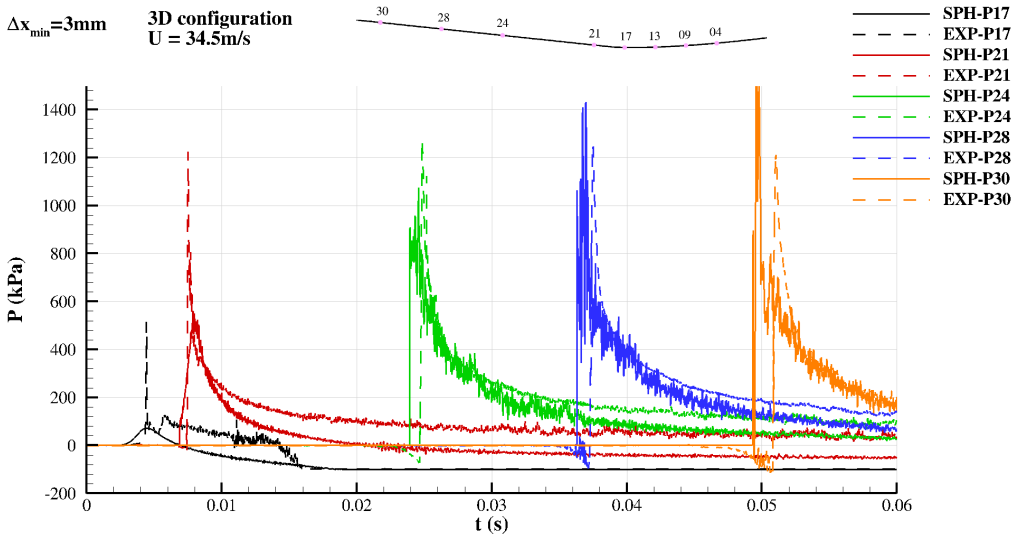

FIGURE 5.20: 3D ditching: experimental vs numerical pressure signals recorded at the probes P17-P30 at the impact speed U=34.5 m/s.

The results are compared to the experimental work of Iafrati et al. [44], which highlighted the occurrence of cavitation in the rear part of the tested specimens. To this aim, a simple but effective cavitation capturing technique was proposed here, which successfully predicted the occurrence of cavitation in the rear part of the specimen in agreement with the experiments, without ever introducing numerical instabilities.

Satisfactory agreement was found between the numerical and experimental campaigns, quantitatively in terms of pressure peak amplitudes and occurrence of cavitation depending on the horizontal impact speed, and qualitatively in terms of the clear resemblance of the SPH cavitation pocket shape with the real one.

However, some differences between the numerical and experimental pressure signals were observed at the rear probes. Indeed, the limitations of a single-phase model were highlighted in this zone, since the absence of air/water vapor phases unsurprisingly alter the predicted loading on the rear part of the fuselage. Consequently, this numerical campaign should be improved upon by considering a multiphase model that includes the existence of an air phase, and a water liquid-vapor phase transition model for a more accurate prediction of cavitation.

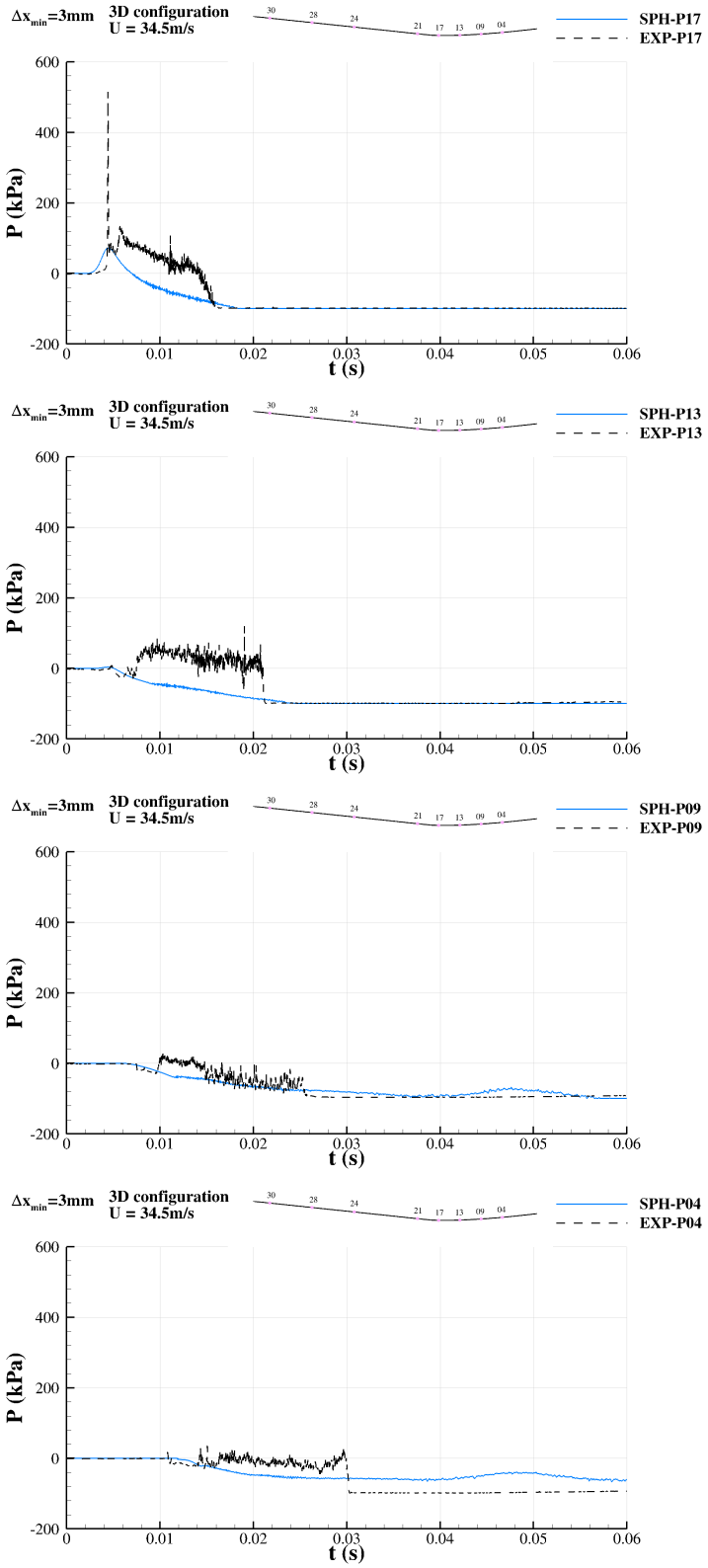

FIGURE 5.21: 3D ditching: experimental vs numerical pressure signals registered by the rear probes P17-P4, at the impact speed U=34.5 m/s.

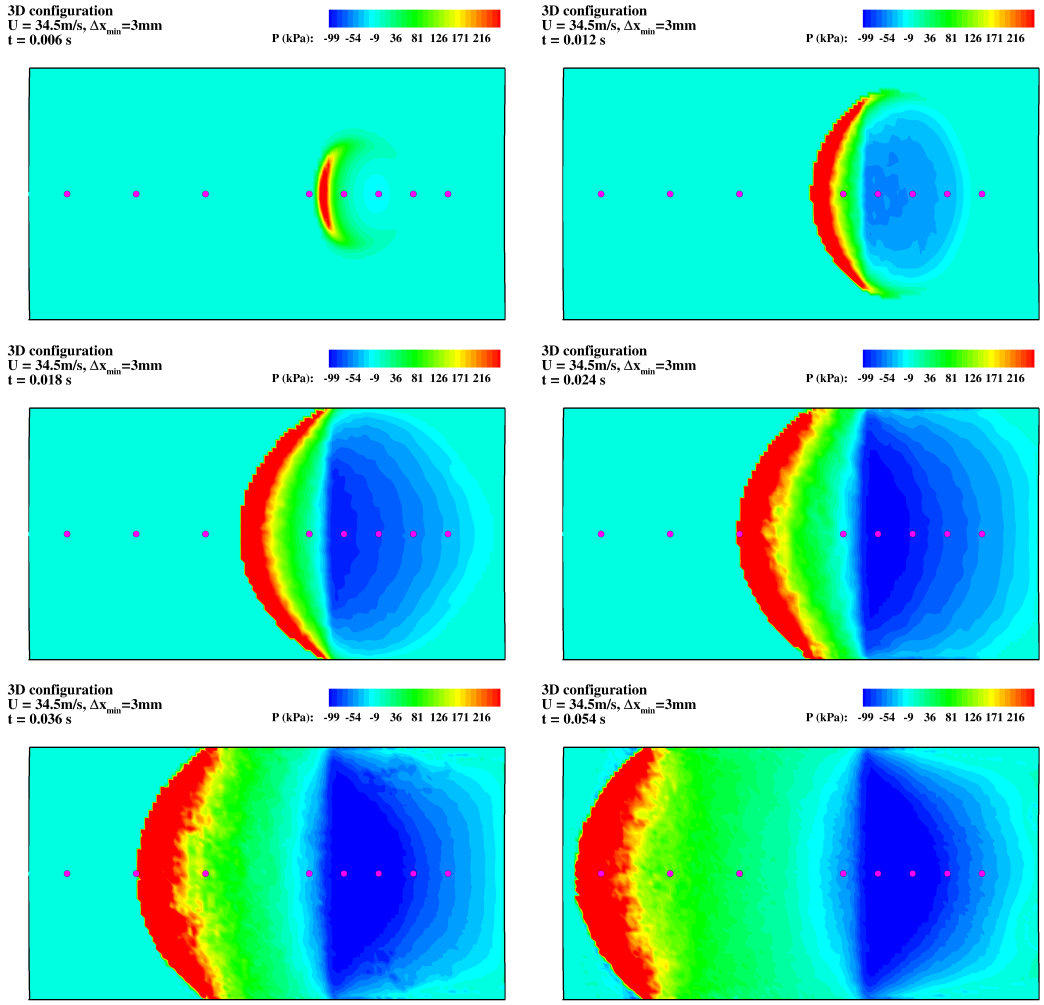

FIGURE 5.22: 3D ditching: evolution of the pressure map on the fuselage impacting at $U = 34.5$ m/s. The pressure does reach the water saturation level in the rear of the fuselage, indicating the occurrence of cavitation. The probes of interest are highlighted in purple.

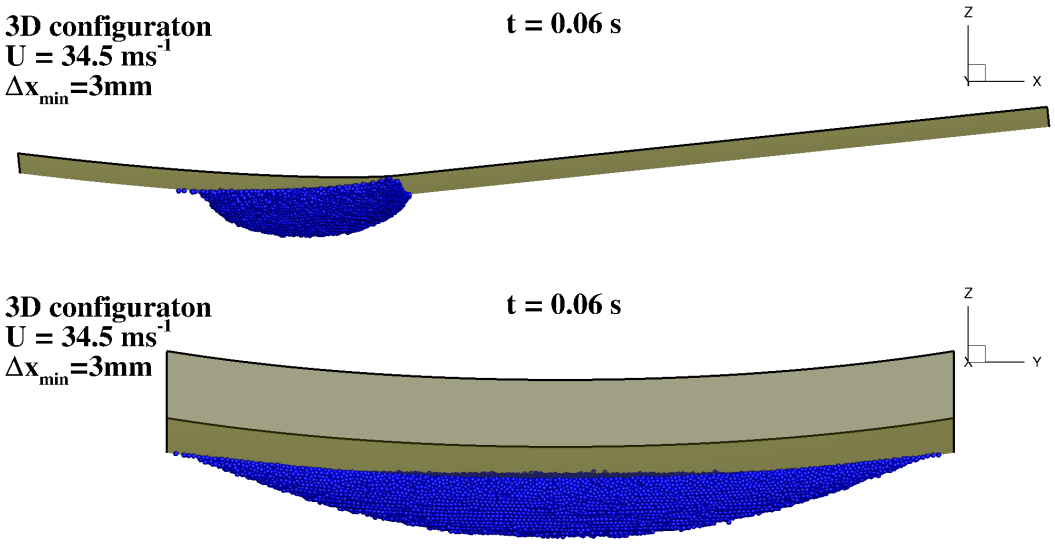

FIGURE 5.23: 3D ditching: side (top) and front (bottom) views of the cavitation pocket, at $t = 0.06$ s.

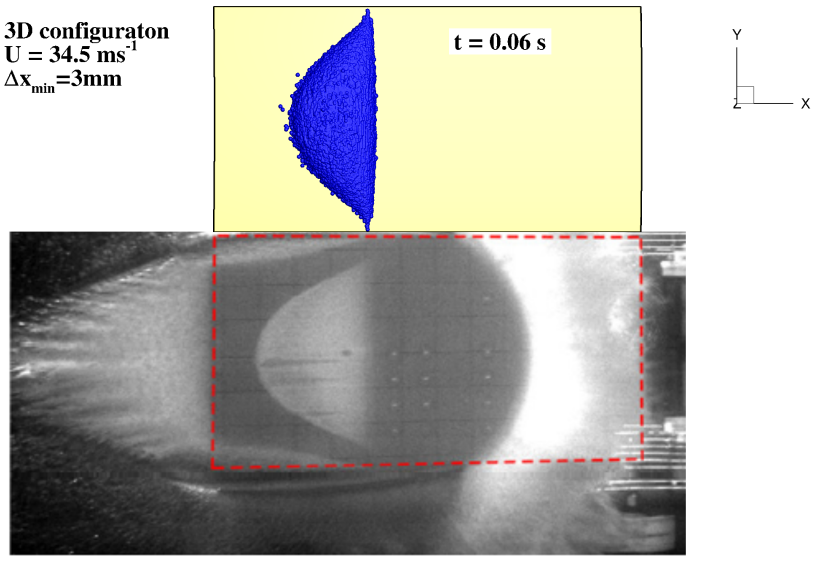

FIGURE 5.24: 3D ditching: qualitative comparison of the cavitation pocket shape and size between the numerical (top) and experimental results (bottom).

Conclusion

This research started with a bibliographical study that highlighted the fundamentals of the SPH method and its application to the Euler equations. The state-of-the-art stabilization techniques were presented, followed by an exposition of the different boundary conditions that the target model should guarantee within the multiphase context. Then, the numerical tools used throughout this thesis were exhibited, such as adaptive particle refinement (APR), and particle shifting methods.

Chapter 2 began with an overview of the state-of-the-art multiphase SPH models, highlighting the pros and cons of each model. Consequently, the Grenier et al. [35] model was identified as the best model to build upon, in view of its ability to keep sharp the interface between fluids via a Shepard computation of the density, and its use of a Volumetric Strain Rate equation which allows the simulation of free-surface flows. A first derivation of the governing equations of the weakly-compressible Multiphase δ-SPH scheme was proposed, followed by an extension of the δ-SPH diffusive terms to multiphase flow in order to eliminate the spurious oscillations of pressure. Then, the numerical stability of the proposed model was studied. It was found that the choice of the sound speed for the different phases was driven by physical and numerical constraints that affect the stability of the scheme. Consequently, a map of the maximal stable CFL coefficients with respect to the phases' sound speed and density ratios was elaborated.

In light of this stability analysis, the third chapter dealt with the validation of the proposed Multiphase δ-SPH scheme. Three well-known test-cases were performed - hydrostatic, dam-break and oscillating fluid patches, in single and two-phase configurations. The results highlighted the capabilities of the model in terms of solving two-phase flows with high density ratios, with or without a free-surface while yielding satisfactory pressure fields. A fourth challenging test-case was introduced, involving the impact of a corrugated MarkIII panel on a water free-surface, coupled with the presence of an entrapped air cavity. The corrugations are small rigid structures under the flat panel, whose shape is given by an analytical function. Our results were compared to the findings of a semi-analytical by Khabakhpasheva et al. [49] based on the Wagner conditions. The pressure field was found to be quasi-uniform in the air bubble as expected. However, the air cavity volume evolution was found to be greatly impacted by the Wagner conditions, since it adds further constraints on the movement of the inner contact point. Nevertheless, aside from the Wagner condition's restrictions, the agreement between our SPH results and the semi-analytical solution can be considered satisfactory.

A variant of Riemann-based SPH schemes [54] also offers the possibility of handling interfacial flows in the presence of a free-surface. A stability study was performed on this Riemann-SPH scheme, then its regions of stability were compared to the proposed Multiphase δ-SPH ones. A discussion over the computational cost of each model ensued, showing that proposed model was much more sensible to the increase in density and/or sound speed ratios. With the maximal stable CFL coefficients determined for the Riemann-SPH scheme, the dam-break and water impact of the corrugated panel test cases used for the validation of the proposed model in Chapter 3 were rerun using Riemann-SPH. The comparison focused on the quality of pressure fields and mechanical energy decay. It was shown that both models yielded similar results provided some adjustments on each scheme are made. On the one hand, a small increase in the parameter α of the proposed model goes a long way in eliminating spurious oscillations of pressure, which as expected, comes at the cost of slightly more diffusion. On the other hand, the Riemann-SPH scheme is vastly improved also in the multiphase context with the use of a particle shifting technique.

In relation with the European SARAH project, in Chapter 5 a numerical investigation of fuselage ditching, at realistic impact speeds, was carried out using the Riemann-SPH scheme discussed in Chapter 4. The ditching configurations were based on the experimental campaign led by Iafrati et al. [44], also in the context of the SARAH project. Their experimental results highlighted the occurrence of the cavitation phenomenon in the water, depending on the horizontal impact speed. Thus, one of the objectives of this investigation was to see whether it is possible to capture this cavitation phenomenon numerically using SPH. To this aim, a simple yet effective cavitation capturing technique was developed and validated first on 2D simulations of the ditching problem. It was shown to introduce no numerical instabilities, the quality of the pressure field remaining unaltered. Consequently, the full 3D simulations were performed so as to compare the numerical and experimental loading on the fuselage. Satisfactory agreements were observed, in terms of the registered pressure signals peaks and propagation along the specimen, and in terms of the cavitation's occurrence and pocket shape.

All in all, the main objectives of this thesis were to improve the SPH method in the multiphase context, and to apply it to the simulation of the emergency water landing of aircrafts. These targets were effectively achieved. On the one hand, a new multiphase SPH model was proposed, that is able to handle high density ratios between the fluids and the presence of a free-surface, while yielding noise-free pressure fields. On the other hand, the SPH method was successfully used for the numerical simulation of fuselage water impact at realistic speed conditions, within the scope of the SARAH project.

Nevertheless, there is still room for improvement regarding the topics treated in this thesis. Firstly, the absence of particle shifting within the proposed Multiphase δ-SPH can be noted, which is solely due to time constraints. Thus, in the short term, a particle shifting technique should be added, quite straightforwardly, to the proposed Multiphase δ-SPH model,

which would enhance its results on the one hand, and enrich its comparison with the Riemann-SPH scheme on the other hand.

Secondly, the heuristic stability regions obtained in Chapter 2 for the proposed scheme can be further explored theoretically. For instance, the von Neumann stability analysis performed by Violeau and Leroy [101] on the single-phase weakly-compressible SPH equations, could be extended to our multiphase SPH model equations.

Finally, although the proposed Multiphase δ-SPH model was a very good candidate for the ditching simulations of Chapter 5, the numerical campaign was carried out using the multiphase Riemann-SPH scheme. This choice was purely a pragmatic one, since all the numerical tools available in our lab that are crucial to these complex simulations are, to this day, only developed for Riemann-based SPH schemes. Indeed, such numerical tools involve the Adaptive Particle Refinement and Boundary Integral Method, which are not straightforwardly adaptable to the Multiphase δ-SPH scheme. However, it is easy to see the advantages that would be brought on by the proposed model for the simulations of Chapter 5. As a first attempt, we considered ditching to be a single-phase problem, which means that, if used, the proposed model would allow higher CFL coefficients in comparison to Riemann-SPH, as shown in Chapter 4 with the much simpler dam-break test case, saving considerable amounts of computational time. Moreover, this single-phase approach is justified a posteriori, since very close agreement was observed between the 3D numerical and experimental results. However, in the long term these simulations should be improved upon in the future through the use of a multiphase model, such as the one developed in this thesis, which would take into account the surrounding air phase, in conjunction with a water liquid-vapor phase transition model in order to better predict the physics of cavitation.

Bibliography

[1] M. Antuono, A. Colagrossi, and S. Marrone. "Numerical diffusive terms in weakly-compressible SPH schemes". In: *Computer Physics Communications* 183.12 (2012), pp. 2570–2580.

[2] M. Antuono, S. Marrone, A. Colagrossi, and B. Bouscasse. "Energy balance in the δ-SPH scheme". In: *Computer Methods in Applied Mechanics and Engineering* 289 (2015), pp. 209–226.

[3] M. Antuono, A. Colagrossi, S. Marrone, and D. Molteni. "Free-surface flows solved by means of SPH schemes with numerical diffusive terms". In: *Computer Physics Communications* 181.3 (2010), pp. 532–549.

[4] R. A. Bagnold. "Interim report on wave-pressure research". In: *Journal of the Institution of Civil Engineers* 12.7 (1939), pp. 202–226.

[5] D. A. Barcarolo, D. Le Touzé, G. Oger, and F. de Vuyst. "Adaptive particle refinement and derefinement applied to the smoothed particle hydrodynamics method". In: *Journal of Computational Physics* 273 (2014), pp. 640–657.

[6] M. J. Berger and P. Colella. "Local adaptive mesh refinement for shock hydrodynamics". In: *Journal of Computational Physics* 82.1 (1989), pp. 64–84.

[7] J. Bonet and T.-S. L. Lok. "Variational and momentum preservation aspects of Smooth Particle Hydrodynamic formulations". In: *Computer Methods in Applied Mechanics and Engineering* 180.1 (1999), pp. 97–115.

[8] B. Buckner. "Green Water on Ship-type Offshore Structures". PhD thesis. Delft University of Technology, 2002.

[9] S. Børve, M. Omang, and J. Trulsen. "Regularized smoothed particle hydrodynamics with improved multi-resolution handling". In: *Journal of Computational Physics* 208.1 (2005), pp. 345–367.

[10] G. Capdeville. "Modélisation numérique d'écoulements compressibles, partie I et II". In: *Cours de l'Ecole Centrale de Nantes* (2006).

[11] L. Chiron. "Coupling and improvements of the SPH method to treat flows involving temporal and spatial multi-scales". PhD thesis. Ecole Centrale de Nantes, 2017.

[12] L. Chiron, G. Oger, M. de Leffe, and D. Le Touzé. "Analysis and improvements of Adaptive Particle Refinement (APR) through CPU time, accuracy and robustness considerations". In: *Journal of Computational Physics* 354 (2018), pp. 552–575.

[13] L. Chiron, M. de Leffe, G. Oger, and D. Le Touzé. "Fast and accurate SPH modelling of 3D complex wall boundaries in viscous and non viscous flows". In: *Computer Physics Communications* 234 (2019), pp. 93–111.

[14] A. J. Chorin. "Numerical solution of incompressible flow problems". In: *Studies in Numerical Analysis* 2 (1968), pp. 64–71.

[15] H. Climent, L. Benitez, F. Rosich, F. Rueda, and N. Pentecote. "Aircraft ditching numerical simulation". In: *25th Int. Congress of the Aeronautical Sciences, Hamburg, Germany*. 2006.

[16] A. Colagrossi, M. Antuono, and D. Le Touzé. "Theoretical considerations on the free-surface role in the smoothed-particle-hydrodynamics model". In: *Physical Review E* 79 (2009).

[17] A. Colagrossi, G. Colicchio, and D. Le Touzé. "Enforcing boundary conditions in SPH applications involving bodies with right angles". In: *Proceedings of the 2nd International SPHERIC Workshop*. Madrid, Spain, May 2007.

[18] A. Colagrossi and M. Landrini. "Numerical simulation of interfacial flows by smoothed particle hydrodynamics". In: *Journal of computational physics* 191.2 (2003), pp. 448–475.

[19] A. Colagrossi, D. Durante, J. Avalos, and A. Souto-Iglesias. "Discussion of Stokes' hypothesis through the smoothed particle hydrodynamics model". In: *Physical Review E* 96 (2017).

[20] A. Colagrossi, B. Bouscasse, M. Antuono, and S. Marrone. "Particle packing algorithm for SPH schemes". In: *Computer Physics Communications* 183.8 (2012), pp. 1641–1653.

[21] R. H. Cole. *Underwater explosions*. Princeton University Press, 1948.

[22] S. J. Cummins and M. Rudman. "An SPH Projection Method". In: *Journal of Computational Physics* 152.2 (1999), pp. 584–607.

[23] M. De Leffe. "Modélisation d'écoulements visqueux par méthode SPH en vue d'application à l'hydrodynamique navale". PhD thesis. Ecole Centrale de Nantes, 2011.

[24] W. Dehnen and H. Aly. "Improving convergence in smoothed particle hydrodynamics simulations without pairing instability". In: *Monthly Notices of the Royal Astronomical Society* 425.2 (2012), pp. 1068–1082.

[25] G. A. Dilts. "Moving-least-squares-particle hydrodynamics - I. Consistency and stability". In: *International Journal for Numerical Methods in Engineering* 44.8 (1999), pp. 1115–1155.

[26] C. Eckart. "Variation Principles of Hydrodynamics". In: *Physics of Fluids* 3.3 (1960), pp. 421–427.

[27] P. Español and M. Revenga. "Smoothed dissipative particle dynamics". In: *Physical Review E* 67 (2003).

[28] J. Feldman. "Dynamic refinement and boundary contact forces in smoothed particle hydrodynamics with applications in fluid flow problems". PhD thesis. Swansea University, 2006.

[29] M. Ferrand, D. R. Laurence, B. D. Rogers, D. Violeau, and C. Kassiotis. "Unified semi-analytical wall boundary conditions for inviscid, laminar or turbulent flows in the meshless SPH method". In: *International Journal for Numerical Methods in Fluids* 71.4 (), pp. 446–472.

[30] A. Ferrari, M. Dumbser, E. F. Toro, and A. Armanini. "A new 3D parallel SPH scheme for free surface flows". In: *Computers and Fluids* 38.6 (2009), pp. 1203–1217.

[31] J.-M. Ghidaglia, A. Kumbaro, and G. Le Coq. "Une méthode volumes finis à flux caractéristiques pour la résolution numérique des systèmes hyperboliques de lois de conservation". In: *Comptes rendus de l'Académie des sciences. Série 1, Mathématique* 322.10 (1996), pp. 981–988.

[32] R. A. Gingold and J. J. Monaghan. "Smoothed particle hydrodynamics - Theory and application to non-spherical stars". In: *Monthly Notices of the Royal Astronomical Society* 181.3 (1977), pp. 375–389.

[33] N. Grenier. "Numerical modelisation by SPH method of water-oil separation in gravity separators". PhD thesis. Ecole Centrale de Nantes, 2009.

[34] N. Grenier, M. Antuono, A. Colagrossi, D. Le Touzé, and B. Alessandrini. "An Hamiltonian interface SPH formulation for multi-fluid and free surface flows". In: *Journal of Computational Physics* 228.22 (2009), pp. 8380–8393.

[35] N. Grenier, D. Le Touzé, A. Colagrossi, M. Antuono, and G. Colicchio. "Viscous bubbly flows simulation with an interface SPH model". In: *Ocean Engineering* 69 (2013), pp. 88–102.

[36] P. Groenenboom and M. Siemann. "Fluid-structure interaction by the mixed SPH-FE method with application to aircraft ditching". In: *The International Journal of Multiphysics* 9.3 (2016).

[37] P.-M. Guilcher. "Contribution au développement d'une méthode SPH pour la simulation numérique des interactions houle-structure". PhD thesis. Ecole Centrale de Nantes, 2008.

[38] P.-M. Guilcher, G. Oger, E. Jacquin, L. Brosset, N. Grenier, and D. Le Touzé. "Simulation of liquid impacts with a two-phase parallel SPH model". In: *International Journal of Offshore and Polar Engineering* 24 (2014), pp. 11–20.

[39] B. Guo, P. Liu, Q. Qu, and J. Wang. "Effect of pitch angle on initial stage of a transport airplane ditching". In: *Chinese Journal of Aeronautics* 26 (2013), pp. 17–26.

[40] L. Hernquist and N. Katz. "TREESPH: A Unification of SPH with the Hierarchical Tree Method". In: *Astrophysical Journal, Supplement Series* 70 (1989).

[41] X. Y. Hu and N. A. Adams. "A constant-density approach for incompressible multi-phase SPH". In: *Journal of Computational Physics* 228.6 (2009), pp. 2082–2091.

[42] X. Y. Hu and N. A. Adams. "A multi-phase SPH method for macroscopic and mesoscopic flows". In: *Journal of Computational Physics* 213.2 (2006), pp. 844–861.

[43] X. Y. Hu and N. A. Adams. "An incompressible multi-phase SPH method". In: *Journal of Computational Physics* 227.1 (2007), pp. 264–278.

[44] A. Iafrati and S. Grizzi. "Cavitation and ventilation modalities during ditching". In: *Physics of Fluids* 31.5 (2019).

[45] "Incompressible smoothed particle hydrodynamics for free-surface flows: A generalised diffusion-based algorithm for stability and validations for impulsive flows and propagating waves". In: *Journal of Computational Physics* 231.4 (2012), pp. 1499–1523.

[46] M. J. Ivings, D. M. Causon, and E. F. Toro. "On Riemann solvers for compressible liquids". In: *International Journal for Numerical Methods in Fluids* 28.3 (1998), pp. 395–418.

[47] K. E. Jackson and Y. T. Fuchs. "Comparison of ALE and SPH Simulations of Vertical Drop Tests of a Composite Fuselage Section into Water". In: *10th International LS-DYNA Users Conference*. Washington, DC, USA, 2008.

[48] T. von Kármán. "The impact on seaplane floats during landing". In: *National Advisory Committee on Aeronautics* (1929).

[49] T. I. Khabakhpasheva, A. A. Korobkin, and S. Malenica. "Fluid impact onto a corrugated panel with trapped gas cavity". In: *Applied Ocean Research* 39 (2013), pp. 97–112.

[50] A. Korobkin and A. Iafrati. "Numerical study of jet flow generated by impact on weakly compressible liquid". In: *Physics of Fluids* 18 (2006).

[51] A. C. H. Kruisbrink, F. R. Pearce, T. Yue, and H. P. Morvan. "An SPH multi-fluid model based on quasi buoyancy for interface stabilization up to high density ratios and realistic wave speed ratios". In: *International Journal for Numerical Methods in Fluids* 87.10 (2018), pp. 487–507.

[52] S. Kulasegaram, J. Bonet, R. W. Lewis, and M. Profit. "A variational formulation based contact algorithm for rigid boundaries in two-dimensional SPH applications". In: *Computational Mechanics* 33 (2004), pp. 316–325.

[53] P. D. Lax and R. D. Richtmyer. "Survey of the stability of linear finite difference equations". In: *Communications on Pure and Applied Mathematics* 9.2 (1956), pp. 267–293.

[54] J. Leduc, F. Leboeuf, M. Lance, E. Parkinson, and J. C. Marongiu. "Improvement of multiphase model using preconditioned Riemann solvers". In: *Proceedings of the 5th International SPHERIC Workshop*. Manchester, UK, June 2010.

[55] B. van Leer. "Towards the ultimate conservative difference scheme - V. A second-order sequel to Godunov's method". In: *Journal of Computational Physics* 32 (1979), pp. 101–136.

[56] A. Leroy, D. Violeau, M. Ferrand, and C. Kassiotis. "Unified semi-analytical wall boundary conditions applied to 2-D incompressible SPH". In: *Journal of Computational Physics* 261 (2014), pp. 106–129.

[57] S. J. Lind, P. K. Stansby, and B. D. Rogers. "Incompressible–compressible flows with a transient discontinuous interface using smoothed particle hydrodynamics (SPH)". In: *Journal of Computational Physics* 309 (2016), pp. 129–147.

[58] L. Lobovský, E. Botia-Vera, F. Castellana, J. Mas-Soler, and A. Souto-Iglesias. "Experimental investigation of dynamic pressure loads during dam break". In: *Journal of Fluids and Structures* 48 (2014), pp. 407–434.

[59] L. B. Lucy. "A numerical approach to testing the fission hypothesis". In: *The Astronomical Journal* 82 (1977), pp. 375–389.

[60] S. Marrone, A. Colagrossi, A. Di Mascio, and D. Le Touzé. "Analysis of free-surface flows through energy considerations: Single-phase versus two-phase modeling". In: *Physical Review E* 93 (2016).

[61] S. Marrone, A. Colagrossi, J. S. Park, and E. F. Campana. "Challenges on the numerical prediction of slamming loads on LNG tank insulation panels". In: *Ocean Engineering* 141 (2017), pp. 512–530.

[62] S. Marrone, M. Antuono, A. Colagrossi, G. Colicchio, D. Le Touzé, and G. Graziani. "δ-SPH model for simulating violent impact flows". In: *Computer Methods in Applied Mechanics and Engineering* 200 (2011), pp. 1526–1542.

[63] S. Marrone, A. Colagrossi, D. Le Touzé, and G. Graziani. "Fast free-surface detection and level-set function definition in SPH solvers". In: *Journal of Computational Physics* 229.10 (2010), pp. 3652–3663.

[64] S. Marrone, A. Colagrossi, L. Chiron, M. De Leffe, and D. Le Touzé. "High-speed water impacts of flat plates in different ditching configuration through a Riemann-ALE SPH model". In: *Journal of Hydrodynamics* 30.1 (2018), pp. 38–48.

[65] S. Marrone, A. Colagrossi, A. Di Mascio, and D. Le Touzé. "Prediction of energy losses in water impacts using incompressible and weakly compressible models". In: *Journal of Fluids and Structures* 54 (2015), pp. 802–822.

[66] J. C. Martin and W. J. Moyce. "Part IV. An Experimental Study of the Collapse of Liquid Columns on a Rigid Horizontal Plane". In: *Philosophical Transactions of The Royal Society A: Mathematical, Physical and Engineering Sciences* 244 (1952), pp. 312–324.

[67] S. Mas-Gallic and P. A. Raviart. "A particle method for first-order symmetric systems". In: *Numerische Mathematik* 51 (1987), pp. 323–352.

[68] D. D. Meringolo, S. Marrone, A. Colagrossi, and Y. Liu. "A dynamic δ-SPH model: How to get rid of diffusive parameter tuning". In: *Computers & Fluids* 179 (2019), pp. 334–355.

[69] D. Molteni and A. Colagrossi. "A simple procedure to improve the pressure evaluation in hydrodynamic context using the SPH". In: *Computer Physics Communications* 180.6 (2009), pp. 861–872.

[70] J. J. Monaghan. "On the problem of penetration in particle methods". In: *Journal of Computational Physics* 82.1 (1989), pp. 1–15.

[71] J. J. Monaghan. "Simulating Free Surface Flows with SPH". In: *Journal of Computational Physics* 110.2 (1994), pp. 399–406.

[72] J. J. Monaghan. "Smoothed Particle Hydrodynamics". In: *Annual Review of Astronomy and Astrophysics* 30.1 (1992), pp. 543–574.

[73] J. J. Monaghan. "Smoothed particle hydrodynamics". In: *Reports on Progress in Physics* 68.8 (2005), pp. 1703–1759.

[74] J. J. Monaghan. "SPH without a Tensile Instability". In: *Journal of Computational Physics* 159.2 (2000), pp. 290–311.

[75] J. J. Monaghan and A. Rafiee. "A simple SPH algorithm for multi-fluid flow with high density ratios". In: *International Journal for Numerical Methods in Fluids* 71.5 (2013), pp. 537–561.

[76] J. P. Morris, P. J. Fox, and Y. Zhu. "Modelling low Reynolds number incompressible flows using SPH". In: *Journal of Computational Physics* 136 (1997), pp. 214–226.

[77] A. Murrone and H. Guillard. "A five equation reduced model for compressible two phase flow problems". In: *Journal of Computational Physics* 202 (2005), pp. 664–698.

[78] R. P. Nelson and J. C. B. Papaloizou. "Variable smoothing lengths and energy conservation in smoothed particle hydrodynamics". In: *Monthly Notices of the Royal Astronomical Society* 270 (1994), pp. 1–20.

[79] J. von Neumann and R. D. Richtmyer. "A Method for the Numerical Calculation of Hydrodynamic Shocks". In: *Journal of Applied Physics* 21.3 (1950), pp. 232–237.

[80] S. Nugent and H. Posch. "Liquid drops and surface tension with smoothed particle applied mechanics". In: *Physical review E* 62 (2000), pp. 4968–4975.

[81] G. Oger. "Aspects théoriques de la méthode SPH et applications à l'hydrodynamique à surface libre". PhD thesis. Ecole Centrale de Nantes, 2006.

[82] G. Oger, M. Doring, B. Alessandrini, and P. Ferrant. "An improved SPH method: Towards higher order convergence". In: *Journal of Computational Physics* 225.2 (2007), pp. 1472–1492.

[83] G. Oger, S. Marrone, D. Le Touzé, and M. de Leffe. "SPH Accuracy Improvement Through the Combination of a quasi-Lagrangian Shifting Transport Velocity and Consistent ALE Formalisms". In: *Journal of Computational Physics* 313 (2016), pp. 76–98.

[84] G. Oger, M. Doring, B. Alessandrini, and P. Ferrant. "Two-Dimensional SPH Simulations of Wedge Water Entries". In: *Journal of Computational Physics* 213 (2006), pp. 803–822.

[85] R. Ortiz, G. Portemont, J. L. Charles, and J. F. Sobry. "Assessment of Explicit FE Capabilities for Full Scale Coupled Fluid/Structure Aircraft Ditching Simulations". In: *Proceedings of the 23rd International Congress of the Aeronautical Sciences*. Toronto, Canada, Sept. 2002.

[86] S. Osher. "Riemann Solvers, the Entropy Condition, and Difference". In: *SIAM Journal on Numerical Analysis* 21.2 (1984), pp. 217–235.

[87] A. N. Parshikov and S. A. Medin. "Smoothed Particle Hydrodynamics Using Interparticle Contact Algorithms". In: *Journal of Computational Physics* 180.1 (2002), pp. 358–382.

[88] N. Pentecôte. "Validation of PAM-CRASH code for the simulation of the impact on water". In: *DLR–IB 435.2003* 3 (2003).

[89] N. Pentecôte and A. Vigliotti. "Crashworthiness of helicopters on water: Test and simulation of a full-scale WG30 impacting on water". In: *International Journal of Crashworthiness* 8.6 (2003), pp. 559–572.

[90] Q. Qu, M. Hu, H. Guo, P. Liu, and R. K. Agarwal. "Study of Ditching Characteristics of Transport Aircraft by Global Moving Mesh Method". In: *Journal of Aircraft* 52 (2015), pp. 1550–1558.

[91] N. J. Quinlan, M. Basa, and M. Lastiwka. "Truncation error in mesh-free particle methods". In: *International Journal for Numerical Methods in Engineering* 66.13 (2006), pp. 2064–2085.

[92] P. W. Randles and L. D. Libersky. "Smoothed Particle Hydrodynamics: Some recent improvements and applications". In: *Computer Methods in Applied Mechanics and Engineering* 139.1 (1996), pp. 375–408.

[93] Y. Reyes López, D. Roose, and C. Recarey Morfa. "Dynamic particle refinement in SPH: application to free surface flow and non-cohesive soil simulations". In: *Computational Mechanics* 51 (2013), pp. 731–741.

[94] M. Siemann. "Numerical and experimental investigation of the structural behavior during aircraft emergency landing on water". PhD thesis. Institute of Structures and Design, 2016.

[95] P. K. Stansby, A. Chegini, and T. C. D. Barnes. "The initial stages of dam-break flow". In: *Journal of Fluid Mechanics* 374 (1998), pp. 407–424.

[96] P. N. Sun, A. Colagrossi, D. Le Touzé, and A.-M. Zhang. "Extension of the δ-Plus-SPH model for simulating Vortex-Induced-Vibration problems". In: *Journal of Fluids and Structures* 90 (2019), pp. 19–42.

[97] H. Takeda, S. M. Miyama, and M. Sekiya. "Numerical Simulation of Viscous Flow by Smoothed Particle Hydrodynamics". In: *Progress of Theoretical Physics* 92.5 (1994), pp. 939–960.

[98] R. Vacondio, B. D. Rogers, P. K. Stansby, P. Mignosa, and J. Feldman. "Variable resolution for SPH: A dynamic particle coalescing and splitting scheme". In: *Computer Methods in Applied Mechanics and Engineering* 256 (2013), pp. 132–148.

[99] R. Vignjevic and M. Meo. "Simulation of helicopter under-floor structure impact on water". In: *International Journal of Crashworthiness* 6.3 (2001), pp. 425–443.

[100] J.-P. Vila. "On particle weighted methods and smooth particle hydrodynamics". In: *Mathematical models and methods in applied sciences* 9 (1999), pp. 161–209.

[101] D. Violeau and A. Leroy. "On the maximum time step in weakly compressible SPH". In: *Journal of Computational Physics* 256 (2014), pp. 388–415.

[102] D. Violeau, A. Leroy, and A. Mayrhofer. "Exact computation of SPH wall renormalising integrals in 3-D". In: *Proceedings of the 9th SPHERIC International Workshop*. Paris, France, June 2014.

[103] H. Wagner. "Phenomena associated with impacts and sliding on liquid surfaces". In: *Zeitschrift für Angewandte Mathematik und Mechanik* 12.4 (1932), pp. 193–215.

[104] H. Wei, Y. H. Wang, and C. H. Chen. "Numerical Simulation of Aircraft Ditching Based on ALE Method". In: *Mechanical Components and Control Engineering* 668 (2014), pp. 490–493.

[105] H. Wendland. "Piecewise polynomial, positive definite and compactly supported radial functions of minimal degree". In: *Advances in Computational Mathematics* 4.1 (1995), pp. 389–396.

[106] A. Wick, G. Zink, R. Ruszkowski, and T. Shih. "Computational simulation of an unmanned air vehicle impacting water". In: *45th American Institute of Aeronautics and Astronautics Aerospace Sciences Meeting and Exhibit*. Reno, Nevada, USA, Jan. 2007.

[107] T. Xiao, N. Qin, Z. Lu, X. Sun, M. Tong, and Z. Wang. "Development of a smoothed particle hydrodynamics method and its application to aircraft ditching simulations". In: *Aerospace Science and Technology* 66 (2017), pp. 28–43.

[108] R. Xu, P. Stansby, and D. Laurence. "Accuracy and stability in incompressible SPH (ISPH) based on the projection method and a new approach". In: *Journal of Computational Physics* 228.18 (2009), pp. 6703–6725.

[109] R. Zhao and O. Faltinsen. "Water entry of two-dimensional bodies". In: *Journal of Fluid Mechanics* 246 (1993), pp. 593–612.

Titre: Amélioration de la méthode SPH pour écoulements multiphasiques et application à l'amerrissage d'urgence d'avions

Mots clés: Smoothed Particle Hydrodynamics, multiphasique, impact d'eau, amerrissage, δ-SPH

Résumé: Cette thèse porte sur l'amélioration de la méthode SPH pour les écoulements multiphasiques, et son application à l'amerrissage d'urgence d'avions. Ce problème, appelé aussi «ditching», est caractérisé par des écoulements violents donnant suite à de larges déformations de la surface libre. En outre, le problème du ditching englobe des évolutions couplées des différentes phases présentes pendant l'impact, à savoir l'air, l'eau liquide et, dans des cas extrêmes, la vapeur d'eau. La méthode SPH est un excellent candidat pour simuler de tels problèmes. En effet, d'une part, l'absence de maillage dans cette méthode permet plus facilement de calculer les grandes déformations de la surface libre, en s'affranchissant complètement du problème de distorsion du maillage, contrairement aux autres méthodes numériques classiques telles que les Éléments Finis. D'autre part, la méthode SPH se prête naturellement à la simulation d'écoulements multiphasiques de par son formalisme lagrangien. L'absence de termes convectifs au sein des équations SPH prévient l'existence de diffusion numérique à l'interface entre les fluides, supprimant le besoin classique de schémas de capture d'interface.

Lors de cette thèse, dans un premier temps, un nouveau modèle SPH faiblement compressible explicite a été développé, capable de simuler des écoulements multiphasiques à hauts ratios de densité, éventuellement en présence d'une surface libre, tout en produisant des champs de pression libres d'oscillations numériques. Une étude de la stabilité numérique de ce modèle a été menée, résultant en une définition heuristique des pas temps maximaux stables en fonction du ratio de vitesses du son des fluides mis en jeu. Ensuite, le modèle a été validé puis comparé à un schéma Riemann-SPH, en termes de domaine de stabilité, de champs de pression et de diffusion numérique. Finalement, dans le cadre du projet européen SARAH, la méthode SPH a été appliquée au problème d'amerrissage d'avions dans des conditions de vitesses d'impact réelles. Des expériences menées par des partenaires du projet ont démontré l'existence du phénomène de cavitation à partir de certaines vitesses d'impact. En conséquence, une technique de capture de cavitation numérique a été introduite dans cette thèse. Enfin, à l'issue de simulations SPH 2D et 3D, un accord satisfaisant a été observé entre l'expérience et nos résultats numériques.

Title: Improvement of the SPH method for multiphase flows and application to the emergency water landing of aircrafts

Keywords: Smoothed Particle Hydrodynamics, multi-phase flows, water impact, ditching, δ-SPH

Abstract: This thesis focuses on the improvement of the SPH method for multiphase flows, and its application to emergency landing of aircrafts. This problem, also known as "ditching", is characterized by violent flows resulting in large deformations of the free-surface. In addition, the ditching problem encompasses coupled evolutions of the different phases present during the impact, namely air, liquid water and, in extreme cases, water vapor. The SPH method is an excellent candidate for simulating such problems. Indeed, on the one hand, the absence of mesh within this method makes it easier to compute large deformations of the free-surface, completely eliminating the problem of mesh distortion, unlike other classical numerical methods such as Finite Elements. On the other hand, the SPH method naturally lends itself to the simulation of multiphase flows due to its Lagrangian formalism. The absence of convective terms within the SPH equations prevents the existence of numerical diffusion at the interface between fluids, eliminating the traditional need for interface capture schemes.

During this thesis, first a new explicit weakly-compressible SPH model was developed, capable of simulating multiphase flows at high density ratios, possibly in the presence of a free-surface, while producing pressure fields without spurious oscillations. A study of the numerical stability of this model was conducted, resulting in a heuristic definition of the maximum stable time steps as a function of the sound speed ratio of the fluids involved. Then, the model was validated and compared to a Riemann-SPH scheme, in terms of stability domain, pressure fields and numerical diffusion. Finally, as part of the European SARAH project, the SPH method was applied to the problem of aircraft ditching under real impact velocity conditions. Experiments conducted by other partners have demonstrated the existence of cavitation at certain impact speeds. As a result, a numerical cavitation capturing technique was introduced in this thesis. Finally, 2D and 3D SPH simulations yielded a satisfactory agreement between the experiments and our numerical results.